Republic Algerian Democratic and Popular
Ministry of Higher Education and Scientific Research
Tlemcen University

THESIS

Presented at:

FACULTY OF SCIENCE - DEPARTMENT OF COMPUTER SCIENCE

For the graduation of:

DOCTORATE

Specialty: *Computer science*

By :

Imane NEDJAR

On the subject of

Medical images indexation and annotation

Defended Publicly on November 15th at Tlemcen University before a jury composed of:

Mr Azeddine CHIKH	Professor	Tlemcen University	Chairman
Mr Mohammed Amine CHIKH	Professor	Tlemcen University	Thesis supervisor
Mr Saïd MAHMOUDI	Professor	Mons University	Thesis co-supervisor
Mr Mohamed El Amine ABDERRAHIM	MCA	Tlemcen University	Reviewer
Mr Ghalem BELALEM	Professor	Oran 1 University	Reviewer
Mr Baghdad ATHMANI	Professor	Oran 1 University	Reviewer

Acknowledgment

The realization of this thesis will not take place without the physical and psychic support of some people who have contributed from far or near in this completion. Thanking them for their efforts is the least thing that they deserve.

I address my first gratitude and appreciation to Professor Mohamed Amine CHIKH, for his guide during all the time of research by his important advices, his eagerness and encouragement.

Many thanks to Professor Saïd MAHMOUDI, his efforts was the principal pillar in the aspirations achievement of this thesis by previewing all the big and the small things.

I thank my co-workers in Applied Sciences University of Tlemcen and I commend the Algerian Ministry of Higher Education and Scientific Research to what has been committing to improve the level of Algerian university teachers by supporting them to complete their projects.

I would like to express my gratitude to the president Mr Azeddine CHIKH professor at Tlemcen university and the jury members Mr Mohamed El Amine ABDERRAHIM professor at Tlemcen university, Mr Ghalem BELALEM professor at Oran 1 university and Baghdad ATHMANI professor at Oran 1 university; that accepted to evaluate and examine this thesis, in order to get it rich by their remarks and scientific opinions.

The most beautiful gratitude to Professor Pierre MANNEBACK, who opened to us the door of the computer science department, faculty of engineering, at Mons university and by making the good atmosphere to work.

Special greetings to all the team members CREDOM of Biomedical Engineering Laboratory at Tlemcen university and all members and the interns in the computer science department in the faculty of engineering at Mons university, that I have met them in the period of internship. More especially, I give my deepest thanks to Mr Adriano GUTTADAURIA for his technical aids.

My biggest thanks go to my parents, brothers and sisters who are the permanent supporter in my life. I want to especially thank my brother Boumedyen for all things that he give me.

This thesis is dedicated to all who I have mentioned here, also to my friends, family and my loved ones.

Abstract

Computer aided detection and diagnosis CADe/CADx systems, are an essential tools used by physicians to assist them in their daily clinical diagnosis. In cancers diseases, these systems have an important role to perform the early detection and diagnosis, this allows to provide early treatment before it will be too late.

In this thesis, we present several methods to be uses in a computer aided diagnosis system in order to generate structured reports of liver lesions including cancer using Computed Tomography (CT) images. In addition, we propose different methods for computer aided detection of breast cancer, by treating breast density classification using mammography and breast lesion classification using histopathology images.

At this context we present three distingue contributions, the first one is related to the annotation of liver CT images by using a medical ontology, in which we propose three methods.

The second contribution is about breast density classification according to the standard Breast Imaging Reporting and Data System (BI-RADS). In addition to that, we propose an improved version of Synthetic Minority Over-Sampling Technique Algorithm (SMOTE) used to equilibrate the dataset.

The last contribution is about breast lesions classification in the histopathology images. Precisely, we propose a method to distinct benignant and malignant lesions, as well to classify the normal cases, benign cases, in situ and invasive cancer cases.

Keywords: *Medical images*; *Computer-aided diagnosis*; *Image retrieval*; *Liver annotation*; *BEMD*; *Gabor wavelet*; *Mammography*; *Breast tissue classification*; *SMOTE*; *Image classification*; *Histology images*; *Deep learning*.

Contents

List of Figures

List of Tables

Introduction

Medical imaging represents one of the cornerstones used in the detection and diagnostic of diseases. One of the most frightful diseases is cancer, in which many lives are lost every year. According to the statistic given by the World Health Organization in 2018, over 9.6 million people are died with cancer [12]; only the early detection, diagnostics and treatments can improve the survival of patients rates. Medical imaging is used to face cancer by detecting it in the earliest stage.

The rapid progress evolution and improvement of imaging techniques knew since the development of the sonar technology in 1960, despite that the discovery of X-ray imaging was in 1896 [13]. At the moment, there are many available imaging techniques used in the medical field such as Computed Tomography (CT) imaging, Mammography, Magnetic Resonance (MR) imaging, Ultrasound (US) imaging, etc.

Medical images are usually asked by physicians to be used in the cancer diagnosis, their availability and reimbursement facilitate the process. Therefore, this daily production increases the number of medical images [14].

Computer-aided detection and diagnosis CADe/CADx systems are one of the better solutions operating the amount of the produced medical images, by assisting the clinicians in their diagnostics. CAD systems are based on computer models that provide many functionalities in the diagnostic. For example, they can be used to detect, segment the cancers. Also, they can give the type of cancers and annotate its properties.

In this thesis, we were particularly interested in developing computer models of CAD systems for liver and breast cancer annotation and classification.

Motivation

Breast and liver cancers are the most common cancer. In 2018, breast cancer represented the second common cancer, which constituted 11.6% of cancer incidence with 2.09 million cases and the mortality rate among cancer cases was 6.6%, equivalent to 627000 deaths. In other side, liver cancer was the sixth common cancer with 4.7% of cancer incidence; however, it represented the fourth cause of cancer mortality with a rate of 8.2% equivalent to 782000 deaths [12] [15].

These figures were a sufficient source of motivation in order to develop the methods of

computer-aided detection and diagnosis CADe/CADx systems for liver and breast cancers. The CAD systems based on artificial intelligence methods showed their positive impact on improving the diagnosis led by physicians [16]. In fact, the CAD system allows physicians to overcome some problems that affect their performance during the diagnostic, such as misinterpretation due to perceptual fatigue or the weak experience, also to automate the redundant tasks in order to avoid time-consuming.

Objectives

The main goal of this thesis is to develop new methods of computer-aided diagnostic system, by presenting new solutions on images annotation and classification based on indexation approaches. More precisely, we focused on studying liver and breast lesions, including cancers.

For the liver's lesions, we presented several methods for automatic liver annotation using liver CT images in order to generate a structured report, that helps physicians in the process of reporting and image retrieval. The modality CT was chosen, because it is suitable for detecting and diagnosing liver lesions and liver metastases, thanks to its capacity at imaging soft tissue structures [17].

In the breast study, we have focused on two solutions, the first one is related to breast parenchyma tissue classification, and the second one is based on breast lesion classification. We have investigated the development of breast tissue density classification, because breast density is associated with breast cancer risk, where is considered as a marker for prior cancer risk [18]. To achieve this study, we have used the mammography.
On the other side, we have used the histopathology images for breast lesion classification. In fact, the histopathology images analysis obtained from the biopsy process is the most accurate method used to determine for sure if there is cancer or not.

In summary, developing methods to support the pathologists in their diagnostics was the essential aim for us.

Challenges

We found many challenges to realize the objectives of this thesis; we quote them according to the problematic treated.

Liver annotation

- Creation of a standardized report
- Reducing the semantic gap between the low level and height level image features

Breast density and lesions classification

- The use of a standardized classification
- Overcome the imbalance problem of dataset
- Validate the different methods using different datasets
- Avoid the use of handcrafted features

In addition to the above challenges, the development of efficient methods that compete the related works was the most difficult challenge to realize.

Contributions

In this thesis, we will present three distingue contributions.

The first one, consists of developing liver annotation methods by using ontology to generate a standardized report. In addition to this, and in order to avoid the semantic gap between the low level and the height level image features, we used the methods of classification and content-based medical image retrieval for images indexation.

The second and the third contributions are related to breast study, where in the second contribution we developed a method for breast density categorization by applying the standard Breast Imaging Reporting and Data System (BI-RADS) classification. We also proposed an improved version of the SMOTE algorithm to equilibrate the dataset.

In the third contribution, we developed an effective method for the histopathological classification of breast lesions. This kind of images is very complicated, making the extraction of handcraft features a difficult task. For this reason we have proposed to use the deep learning approaches. In addition, the presented method is evaluated on two different datasets.

In order to provide an objective and efficient comparison, we have evaluated all the proposed methods in international challenges.

Thesis Overview

The present thesis is organized as follows:

Chapter 1 gives an overview of medical background, by providing the medical information, including the anatomy and physiology of the liver and breast with their pathologies and diagnosis.

Chapter 2 presents the literature related works on liver annotation, breast density classification and histopathology images classification.

Chapter 3 presents the methods developed for liver CT annotation, with experimentations, including our participation in liver challenge, and comparative study with related works.

Chapter 4 presents the method developed for breast density classification, in addition to the experimentation carried out on different datasets. The chapter concludes by presenting the results obtained in the mammography challenge.

Chapter 5 starts by introducing the fundamentals concept of Convolutional Neuronal Network (CNN) and the different architectures, then the proposed method is presented. Finally, a discussion of the results obtained in the histopathology image challenge is given.

We conclude this thesis with a general conclusion and some potential future works.

Chapter 1

Overview of Liver and Breast

1.1 Introduction

We focus in this chapter on the medical background related to the liver and breast. Where we reviewing the anatomy and physiology of these two organs and we will explain they principals components. Thereafter we will introduce in detail their lesions and finally we will conclude each part by the imaging techniques used to diagnosis the lesions.

1.2 Anatomy and physiology of the liver

The liver is a vital organ comprises around 2% of an human's body weight [19] and is the second largest organ after the skin, partially protected by the ribs, it is located on the right side of the body beneath the diaphragm, on top of the stomach, overlying the gallbladder, right kidney and intestines [20].
It help metabolism support as well immunity and digestion, furthermore detoxification and vitamin storage. These function make him an essential organ in the human's life, fortunately one particularity of the liver is its capacity to regenerate its dead tissues [20].

1.2.1 Liver components

A. ***Liver vessels***

The liver is one of the most densely vascular organs in the human body. It contains more than 10% of the body's total blood volume, and it is crossed by 1.4 liters of blood on average every minute (for an adult).
The liver contains four vessel structures: portal vein, hepatic vein, hepatic arteries and bile ducts.

- *Portal vein*: The portal vein is unique among all bloods vessels of the body. It main function is to bring the blood rich in nutrients from the gastrointestinal tract and spleen to the liver in order to process nutrients and filter out toxic substances;

thereafter the blood goes back into general circulation [21].
This blood accounts for approximately 2/3 to 3/4 of blood flow into the liver.

- *Hepatic veins*: are blood vessels which transport the liver's deoxygenated blood and blood which has been filtered by the liver to the inferior vena cava.
  There are three main hepatic veins which divide off the inferior vena can just below the surface of the diaphragm: the right hepatic vein, middle hepatic vein and left hepatic vein.
- *Hepatic arteries*: arterial blood accounts for only a 1/4 of the blood flow into the liver, however, it supplies about 2/3 to 3/4 of the oxygen to the liver since the blood is more oxygen rich than portal vein blood. The common hepatic artery originates from three main source : the celiac trunk, the left gastric artery and superior mesenteric artery. Where the middle hepatic artery is arises from the celiac trunk, the right hepatic artery is arises from the superior mesenteric artery, the left hepatic artery is which arises from the left gastric artery [22].
- *Bile Ducts*: the liver produce the bile that is used for fats digestion. The bile ducts carry the bile through the liver to the gallbladder to be stored or released directly into the small intestine.

The liver divides into four unequal lobes; the right hepatic lobe is the largest, the left hepatic lobe is the narrowest part of the organ. Between these two major lobes, there is the square lobe and the caudate lobe. The square lobe and the caudate lobe are separated by a furrow called the hilum of the liver. It is at the hilum that the portal vein and the hepatic artery enter the liver, and that major bile ducts pass.
Each lobe of the liver is divided into segments; there are 8 segments in all. These anatomical divisions are important for surgical procedures: when a part of the liver is damaged and must be extracted, resection often follows these anatomical contours.

B. ***Lobules***

The liver is composed of 100,000 functional units named lobule. Each lobule has an hexagonal shape where at each its corner there are portal vein, hepatic artery and bile duct called portal triad [20].
Blood supplying from portal vein and hepatic artery drains into the branch of the hepatic vein that lies in the lobule's center via sinusoidal vascular channel [23]. Each sinusoid containing 2 main cell types: Kupffer cells and Hepatocytes.
Kupffer cells: are a type of macrophage, their functions include the phagocytosis of large particles, secretion of immune-regulatory mediators also they capture and break down old, worn out red blood cells [24].
Hepatocytes: have cubical shape, are the foundation of the lobule and they line the sinusoids; their functions include metabolism, storage, digestion, and bile production

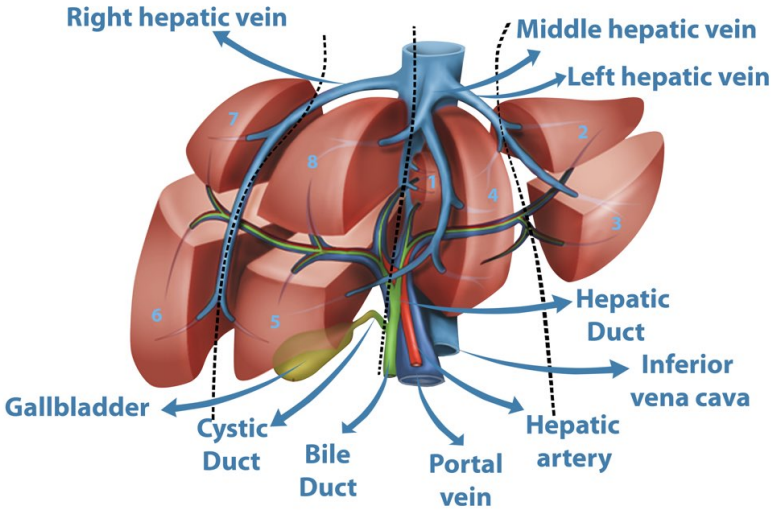

Figure 1.1: Liver vessels and segments [1]

[20]. In the lobule there is a space between the sinusoidal and the hepatocytes cells named the space of Disse, this space allows the hepatocytes to meet the blood and to absorbed the plasma components. Furthermore, it contains the stellate cells that constitute 5% of the total hepatic cell and it function is to store the fat such as vitamin A [25].

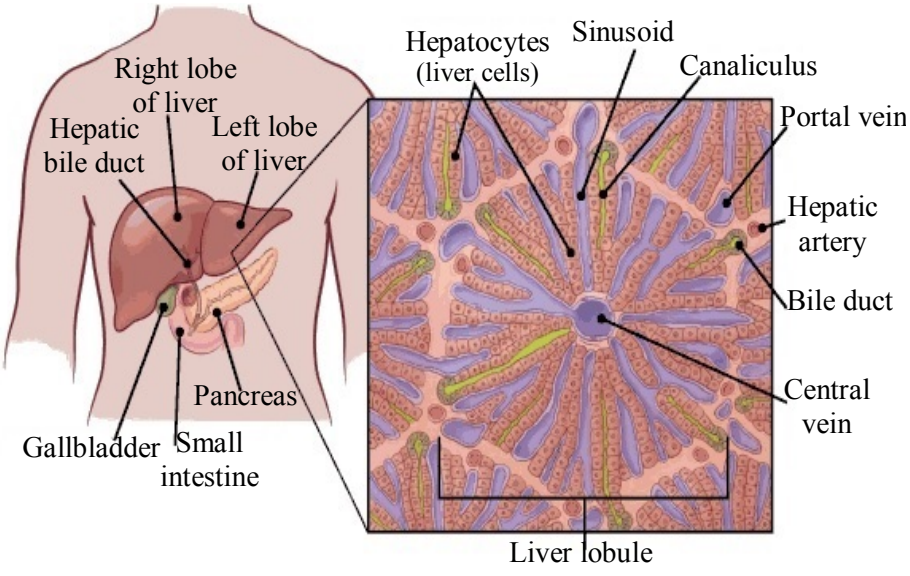

Figure 1.2: Liver lobule [2]

1.2.2 Physiology of the Liver

The liver can be thought of as a chemical factory that processes, transforms and eliminates different substances. In fact, the blood of the portal vein reaches the liver with very many substances resulting from the digestion system. These molecules are absorbed by the cells of the liver which are endowed with specific enzymes and allow their chemical transformation. These changes made by the liver are vital for the body. The liver's functions can be categorized into the following :

A. ***Digestion***

An essential component for digestion is the bile, it is a yellow liquid produced by the Hepatocytes and it released in the bile ducts to be stored in the gallbladder.

The hormone cholecystokinin is liberated from duodenum to stimulate the gallbladder to release bile, this occurs when duodenum contain large fat clumps. The bile turns these large clumps into smaller pieces that have more surface area and are therefore easier for the body to digest [20].

B. ***Metabolism***

The liver is an essential metabolic organ which governs body energy metabolism [26]. Where it contribute to metabolize carbohydrate, lipids, and proteins into biologically substances.

In carbohydrates metabolism, the liver maintaining glucose concentrations in a normal range in the blood [27]. The excess glucose of the blood supplied by the portal vein after a food, is reduced by the liver by storing it in the form of glycogen. When the level of glucose is too low in the blood, the liver degraded the glycogen to the glucose and releases it in the blood [28].

The liver plays a key role in lipid metabolism [29], the lipids reaching the liver are transformed into triglycerides and stored in liver cells. In response to the body's energy needs, these triglycerides are broken down into fatty acids and used. In addition, it transform the excess carbohydrates and proteins into fatty acids and triglycerides, which are then stored in adipose tissue [30].

The liver cells synthesize the amino acids of the dietary proteins obtained from the digestive system. The amino acids will be used as energy source after removing the toxic amine groups and convert them into ammonia and eventually urea [20].

C. ***Detoxification***

Certain substances which arrive at the liver are toxic for the organism: the role of the liver is to degrade these substances into non-toxic products.

The ammonia, which is naturally produced by the colon during the decomposition of the digestive content, has a high neurological toxicity. It is degraded by the liver cells, then eliminated in the urine.

The liver also plays an essential role in the breakdown cycle of hemoglobin. The red blood cells have a lifespan of around 120 days. At the end of this period, they are destroyed in the spleen, where the breakdown of hemoglobin produces free bilirubin. The bilirubin is toxic and can be harmful; it has a characteristic yellow color. It reaches the liver via the bloodstream and is transformed there into conjugated bilirubin, non-toxic.

The alcohol (ethanol) ingested also mainly reaches the liver. Absorbed by the liver cells, it is transformed into acetaldehyde and then into acetate. These substances are returned to the blood and eliminated via the kidneys. But ethanol and acetaldehyde have a toxic effect on liver cells: they have chemical properties that seriously disrupt their functioning, and lead to fatty liver disease.

Medicines taken by mouth reach the liver in the same way: it absorbs and eliminates part of the active substances in the medicine. The dosages of the drugs take into account this intervention of the liver [31].

D. ***Storage***

The liver provides storage of many essential nutrients, vitamins, and minerals obtained from blood passing through the hepatic portal system. Glucose is transported into hepatocytes under the influence of the hormone insulin and stored as the polysaccharide glycogen. Hepatocytes also absorb and store fatty acids from digested triglycerides. The storage of these nutrients allows the liver to maintain the homeostasis of blood glucose. Our liver also stores vitamins and minerals - such as vitamins A, D, E, K, and B12, and the minerals iron and copper - in order to provide a constant supply of these essential substances to the tissues of the body [32].

E. ***Immunity***

The liver is considered as one of innate immune organ [33], due that it processed a set of immune cells. Indeed, the liver contains a large number of Kupffer cells represent 80–90% of the total population of macrophages in the body [34]. The liver contain also an important innate immune cells named natural killer (NK) cells that provide the first line of defense against pathogens and tumors [35].

Moreover, there are NKT cells a liver lymphocyte cells regulator for liver disease by modulating liver inflammation, injury, fibrosis and regeneration [34].

In addition, there are the liver sinusoidal endothelial cells, that play an important role in the innate immunity, where they remove soluble macromolecular and colloidal waste from the circulation, also they detect microbial infection through pattern recognition receptor. In they turn the hepatocytes produce about 80–90% of the circulating innate immunity proteins in the body [34].

1.3 Liver pathologies

The liver represents a key target organ for toxicity [19], that make him prone to a variety of pathologies [25].
The liver pathologies causes given by the National Library of Medicine (NLM) [36] are as following :

- Pathologies caused by viruses, such as hepatitis portal vein is unique
- Pathologies caused by drugs, poisons and alcohol such as fatty liver disease and cirrhosis
- Inherited diseases, such as Wilson disease

From the pathologies there is also liver tumor, the next section we will define each pathology separately.

A. ***Viral Hepatitis***
   Hepatitis is any acute or chronic inflammation of the liver. It is said to be acute when the body comes into contact with the virus, and chronic when it persists beyond 6 months after the start of the infection.
   There are two cause to have Hepatitis : the viral causes with the main hepatitis alphabetical viruses, known as A, B, C, D and 3 other virus Epstein Barr virus, Cyto Megalo virus and herpes.
   The second cause are non-viral such as alcoholism, autoimmune disease and obesity. This disease can progress spontaneously to recovery or progress to cirrhosis or liver cancer [31].

B. ***Fatty liver***
   Non-Alcoholic Fatty Liver Disease (NAFLD) results from the accumulation of fat in liver cells. This occurs, when a person consumes more fat and sugars making triglycerides developed in the hepatocytes exceeds 5% of the liver weight.
   Angulo [37] classify the causes of NAFLD into primary causes, nutritional, drugs, metabolic, toxins and infections.
   The primary causes are : obesity, glucose intolerance, type 2 diabetes, hypertriglyceridemia, low HDL cholesterol, hypertension.
   From the nutritionals causes there are protein calorie malnutrition, rapid weight loss.
   As drugs causes, he cited estrogens, tamoxifen, amiodarone.
   Lipodystrophy and hypopituitarism as metabolic causes.
   The causes can be toxins such as bacillus cereus toxin and infections causes like hepatitis C and human immunodeficiency virus.

C. ***Cirrhosis***

Cirrhosis is the consequence of any chronic liver disease such as viral hepatitis, alcoholic hepatitis, etc. In a patient with liver disease, scar tissue replaces damaged liver cells: it is hepatic fibrosis. The scar tissue surrounds clusters of regenerating liver cells; these clusters constitute regeneration nodules [31].

Cirrhosis therefore changes the function and structure of the liver, which has several consequences: the primary functions of the liver such as filtration of blood and secretion of bile are no longer fulfilled. Portal hypertension develops (increased pressure inside the venous system which leads blood from the digestive system to the liver). Ultimately, cirrhosis can progress to liver cancer within 15 to 20 years of its onset [38].

D. ***Wilson disease***

Wilson's disease is a rare genetic condition occurs when the liver don't release the copper into the bile as it must be. This leads to liver damage and result to releases the copper into the bloodstream. Thereafter many organ are affected like the kidneys, brain, and eyes. in an advanced stage of Wilson Disease, it can cause severe brain damage, liver failure, and death [39].

E. ***Liver tumor***

By definition the tumor is an abnormal growth of cells that can be benign (noncancerous) or malignant (cancerous). Benign tumors usually do not pose a serious health risk, in contrary to malignant tumors that can be fatal [40].

The following section we will introduce the benign liver lesions followed by malignant liver lesions.

1.3.1 Benign liver lesions

One particularity of benign tumor it didn't spread to other organs like malignant tumor.

A. ***Hemangiomas***

Is the most common benign liver lesion, made up of clusters of blood-filled cavities, lined by endothelial cells and fed by the hepatic artery. The small masses (1 mm - 3 cm) and the medium masses (3 cm - 10 cm) don't cause symptoms and do not need treatment, however larger masses (10 cm - 20+cm) can cause pain and usually they will develop complications that require prompt surgical intervention or other kind of therapy [41].

B. ***Focal Nodular Hyperplasia***

Is the second most common benign liver lesion, it develops within hepatic parenchymal tissue, the tumor is characterized by the presence of scar, which is

generally located at the center of the lesion [42]. Focal nodular hyperplasia is more common in young to middle-aged adults, specially females compared to male with a ratio of 8/1 [43]. FNH is typically asymptomatic lesions, usually requiring no treatment.

C. ***Hepatic cysts***

Liver cysts are abnormal fluid-filled sacs that form in the liver occur in up to 5% of the population [44]. Generally don't require treatment unless symptoms develop, and they rarely affect liver function [45].

D. ***Hepatocellular adenoma***

Is an uncommon benign liver tumors, are often round, well-defined pseudoencapsulated masses. The masses can be small (<5cm) or large (>5cm) resection preferred for large masses that pose a greater risk of hemorrhage or malignant progression [46]. The Hepatocellular adenoma, usually occurs in young women which is correlated with increased estrogen levels especially found in the oral contraceptives and also in the obese persons [47].

1.3.2 Malignant liver lesions

In the benign tumor, excessive cell production remains limited and localized. Generally, the benign tumor easily gives way to local treatment. In the case of malignant tumors, excessive cell production becomes anarchic and uncontrolled.

Cancerous liver tumors that start in the liver are called primary liver cancer. The cancerous tumors in the liver that starts in another organ and spread to the liver through blood or lymphatic vessels are called metastatic liver cancer.

A. ***Hepatocellular carcinoma (HCC)***

Develops from liver cells, is the most primary common malignant liver lesion that occurred more often in males than females with the ratio of 4/1 [48]. HCC have two different growth patterns : single tumor that grows larger and spread to other parts of the liver only in the late disease, the second type start as many small cancer nodules throughout the liver [2].

Viral hepatitis and excessive alcohol intake are risk factors, well on the cirrhosis remains the most important risk factor for the development of HCC.

The HCC is the 3rd cause of death from cancer [49] because the diagnosis is too often made in advanced disease degree where the liver is impairment, at this stage, there is virtually no effective treatment that would improve survival [48].

B. ***Intrahepatic cholangiocarcinoma (bile duct cancer)***
Represent 10% to 20% of liver cancer, cholangiocarcinoma can be start in the cells that line the small bile ducts or in the bile ducts outside the liver [16]. Men and women are affected with the same frequency, most often after age 60. The causes of chronic bile inflammation are important risk factors for intrahepatic cholangiocarcinoma [50].

C. ***Angiosarcoma***
Is a rare primary malignancy disease that represent 2% of liver cancer. Starts in the cells lining the blood vessels of the liver more precisely endothelial cells and usually presents as an abdominal mass [51]. Angiosarcoma affects both men and women, the average age is less than 50 years [52]. Generally its evolution is very rapid, by the time that they diagnosis, the cancer usually too widespread thus conduct to die almost patients within 2 years after diagnosis [51] .

D. ***Hepatoblastoma***
Hepatoblastoma is developed in children younger than 4 years old. Usually, the symptom can be abdominal distension or abdominal mass [53]. Fortunately, if this tumor didn't spread outside the liver it will be treated successfully surgery and chemotherapy [2].

1.4 Diagnosis of liver cancer

The liver cancer can be due to many factors such as: gender, race, chronic viral hepatitis, cirrhosis, tobacco use, obesity, type 2 diabetes [54].

1.4.1 Symptoms of liver cancer

The liver cancer symptoms can be as follow :

- Loss of appetite and weight
- Yellowing of the skin and eyes (jaundice)
- An enlarged liver and spleen, felt as fullness under the ribs on the right and the left side respectively
- Vomiting and feeling very full after a small meal

1.4.2 Imaging tests

A. ***Ultrasound***
Ultrasound uses sound waves to produce images of the liver, it is the first test used to look at the liver. This test can show tumors growing in the liver [55] (see Figure 1.3).

B. ***Computed tomography (CT)***

Is a imaging technique which consists in measuring the absorption of X-rays by the tissues then, by computer processing, digitizing and finally reconstructing 2D or 3D images of anatomical structures. It can give specific information of tumor like the size and the shape as well as the information of blood vessels [55] (see Figure 1.4).

C. ***Magnetic resonance imaging (MRI)***

Magnetic Resonance Imaging (MRI), is an examination performed by a device that produces electromagnetic waves with a very powerful magnet. With MRI, the doctors can differentiate between benign and malignant tumor (see Figure 1.5).

D. ***Angiography***

Angiography is a radiological examination that allows to study invisible blood vessels on conventional radiographs. Its purpose is to detect vascularization disorders by injecting the dye into an artery to outline blood vessels while X-ray images are taken. It can also be prescribed before an intervention to pinpoint the path of blood vessels [55] (see Figure 1.6).

Figure 1.3: Ultrasound machine

Figure 1.4: Computed Tomography machine

Figure 1.5: Magnetic Resonance Imaging machine

Figure 1.6: Angiography machine

1.4.3 Other tests

A. ***Biopsy***

The biopsy is a sample of flesh in the organ extracted for analysis, it can be done by hollow needle or an incision, depending on the size and the position of suspicious area, the number of lumps and other medical problems.

Fine-needle aspiration (FNA): is a type of biopsy in which a very fine needle and syringe are used to collect cells, tissue or fluid from an abnormal region or mass. The sample is then examined under a microscope.

Core-needle biopsy: a larger needle is used during core needle biopsy to draw a column of tissue out of a suspicious area. This biopsy is recommended if cancer is suspected.

Surgical biopsy: is an operation in which the tissue of the lump are surgically removed for microscopic examination. This exam is also called open biopsy. A surgical biopsy may be excisional (removes the entire mass or abnormal region) or incisional (removes a fragment from an abnormal mass or region).

1.5 Anatomy and physiology of the breast

The breast organ, medically known as the mammary gland, is located on the anterior chest wall. The female breast is highly complex and more developed than the male breast.
The prime function of the female breast is lactation: a term that encompasses synthesis, secretion and ejection of milk. Prior to puberty there are no discernible differences, functional or structural, between the male and female breast. With the onset of puberty, a big changes ensue in the morphology and function of the female breast. These changes are the result of the unique response of the breast to various normal hormonal influences [56].

1.5.1 Breast components

As shown in Figure 1.7, the breast consists of :

- ***Lobe (milk gland)***: the female breast contain 15–20 sections called lobes. Each of these lobes is composed of many smaller lobules, where milk is produced.
- ***Nipple***: is the small raised area in the center of the breast from which milk is drawn.
- ***Milk Ducts***: are about 6-8 tubes that transfer milk from the lobules to the nipple.
- ***Areola*** : is the dark area of skin surrounding the nipple, it contains sweat glands that serves to lubricate the nipple during breastfeeding.
- ***Breasts tissue***: The breast does not contain muscles. Women's breasts contain fatty tissue, fibrous, and glandular tissue [57]
  - Glandular tissue includes the lobes and the ducts.
  - Fibrous, or connective, tissue include ligaments, supportive tissues, it provide support to the breast and give it its shape.
  - Fatty tissue, fills in the spaces between glandular and fibrous tissue, the amount of fat determines the size of the breast.

1.5.2 Breast development

Human breast tissue begins to develop in the 6th week of fetal life. Breast tissue initially develops along the line between the fetal axilla and inguinal region and form two ridges called the mammary crests or milk lines. By the 9th week of fetal life, the breast tissue regresses (goes back) to the chest area, leaving two breast buds on the upper half of the chest [58] [3].
Figure 1.8 depicts the development of the mammary gland in the fetal life.

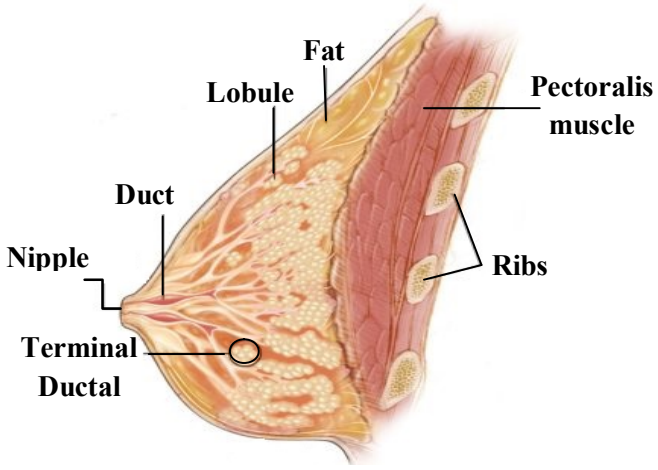

Figure 1.7: Female breast anatomy

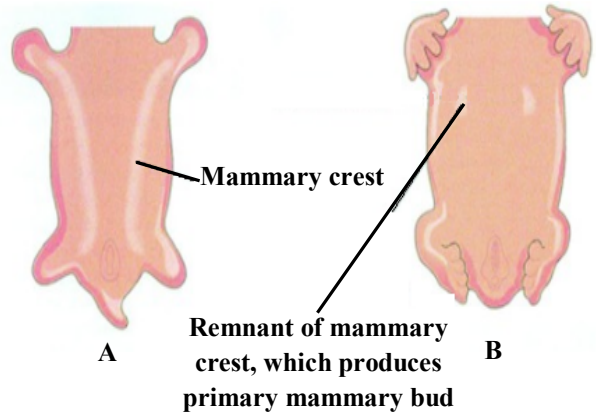

Figure 1.8: Development of the mammary gland. (A) Ventral view of an embryo gestation showing mammary crests. (B) The view showing the remains of the mammary crest [3]

Female breast goes through more changes than any other organ in the body [59], from birth, puberty, pregnancy and breastfeeding, right through to menopause.

- ***From birth until puberty***
  The breast consists of lactiferous ducts.

- ***Puberty***
  In early puberty, the ducts start to proliferate, and their terminations form solid masses of cells that represent the future breast lobules [56]. The areola becomes a prominent bud, and breasts begin to fill out.
  In late puberty, glandular tissue and fatty tissue increase in the breast, and the areola becomes flat.

- ***Pregnancy***
  During pregnancy, the nipples and breasts may feel sensitive and tender, breasts

increase in size very quickly, the nipples and areola change in size and colour as they prepare for milk production [60]. In the late of pregnancy, the nipples start leaking a liquid substance that contains antibodies named colostrum, this can happen also as early as 14 weeks of pregnancy.

- ***Breast feeding***
  After birth, The levels of estrogen and progesterone hormones decrease. The breasts will usually begin to produce milk three to five days after a woman has given birth. During these few days before milk is produced, the body produces colostrum. The researches shows that breastfeeding may reduce the risk of developing breast cancer [61].

- ***Breast changes after menopause***
  After menopause, breast change in size and shape, this is because the breast tissue become more fatty. In fact, the breasts glandular tissue has been kept solid so that the glands could produce milk, shrinks after menopause and is replaced with fatty tissue [56]. Because the breasts become less dense after menopause it is often easier for radiologists to detect breast cancer on an older woman's mammograms.

1.6 Breast pathologies

The pathologies of breast are divided into two categories : Benign lesions and Malignant lesions.
The benign breast lesions are more found in the women than the malignant lesions, and in most cases the treatment don't need surgery, however some benign lesions can be associated with an increase risk of breast cancer. The women are facing the risk of having benign lesions in the second to fifth decades of life, nevertheless, the risk of having malignant lesions continues to increase after menopause. In the next section we introduce the common benign lesions found in the breast.

1.6.1 Benign breast lesions

Benign lesions can develop from mammary tissues. They are not life threatening unlike malignant lesions, except in some cases if they are misplaced or too large.
These lesions are numerous and varied in their aspects. Guray and Sahin [62] classified them into: developmental abnormalities, inflammatory lesions, fibrocystic changes, stromal lesions, and neoplasms.
On other hand, Masciadri and Ferranti [63] gave the classification of benign breast lesions according to histological origin, that represent: terminal and lobular ducts, ductal system and lesions of different origin. In [64] the authors used the categorization based upon the

degree of cellular proliferation and atypia, where three categories of benign breast lesions were defined : non proliferative, proliferative without atypia, and atypical hyperplasia.
In the following section we will introduce the more commonly benign lesions based on the classification given by Guray and Sahin [62], because it is more general.

A. ***Developmental Abnormalities***

Mammary heterotopia: is the presence of supernumerary breast tissue at a nonphysiological site, this tissue is known as ectopic tissue, is seen mostly along the milk line (see Figure 1.8), specially on the chest wall, axilla and vulva. The supernumerary of nipples is called ”Polythelia” and supernumerary of areola or glandular tissue is called ”Polymastia”.

Mammary hypoplasia: is the underdevelopment of glandular tissue during adolescence, Mammary hypoplasia is recognized as Insufficient Glandular Tissue (IGT), the consequence of this lesion is that, the women with IGT have a low milk production or in some cases a total absence of milk. Hypoplastic breasts signs include the lack of change during pregnancy, asymmetrical shape of breasts and the areolas appear swollen.

B. ***Inflammatory lesions***

According to D’Alfonso *et al.* [65], the inflammatory lesions of breast mimic malignancy lesion on clinical and radiographic, which makes their diagnostic more difficult. The inflammatory and reactive changes in the breast are classified into : Mastitis (Lactation Mastitis, Granulomatous Mastitis), Mammary Duct Ectasia and Fat Necrosis.

Lactation Mastitis: is an inflammation of the mammary, which occurs in the vast majority of cases in women who are breastfeeding. It happen when bacteria found on the breast surface penetrate the nipple through small cracks, caused cellulitis (bacterial skin infection) of the interlobular connective tissue.

Granulomatous Mastitis: occurring as reactions resulting from infectious etiology such as tuberculosis and sarcoidosis [62]. The silicone product used for breast augmentation can cause granulomatous reaction in the breast.

Mammary Duct Ectasia: is an inflammation of ducts, identify by the dilatation of the central ducts. These ducts occupied by acidophilic material corresponding to retention of secretion products with intraluminal plugs of histiocytes [66]. Among the symptoms of this condition nipple discharge and inversion, a palpable subareolar mass sometimes associated with pain.

Fat Necrosis: Refers to non-enzymatic necrosis, often caused by a variety of chest injuries. Fat necrosis may mimic breast cancer if it appears as spiculated dense mass [62].

C. ***Fibrocystic Changes***

Fibrocystic changes in the breast, also known as fibrocystic disease, chronic cystic disease and mazoplasia [62], are the most common benign lesion of the breasts that occur in 50 to 80% of premenopausal women.

In fibrocystic disease there are two kind of lesions: solid lesions and liquid or semisolid lesions (macro and micro cysts), which encompasses adenosis, cysts, epithelial hyperplasia with or without atypia, apocrine metaplasia, radial scar, and papilloma [62].

Cyst: A breast cyst is a bag filled with fluid, and have round or ovoid structures that develops in the breast. It is the most common type of breast mass in women aged 35 to 50 years. A breast cyst is usually benign and rarely cancerous. The Cyst can appear in one breast or in both. The symptoms of a breast cyst may be: a mass in a breast, often soft and mobile, it grows, sensitive and painful before or during menstruation.

Adenosis: It is a hyperplasia [1] achieving an increase in size and number of glandular components, mostly involving the lobular units.

The most knowing lesion in Adenosis are : sclerosing adenosis and microglandular adenosis.

Sclerosing adenosis: is a palpable mass which can mimic invasive breast cancer. It is defined as a benign lobulocentric lesion of disordered acinar, myoepithelial, and connective tissue elements [67].

Microglandular adenosis: is characterized by a proliferation of round, small glands distributed irregularly within dense fibrous and/or adipose tissue [62] .

Apocrine Metaplasia: is defined as a benign epithelial alteration of breast tissue and it manifest as non-proliferative breast lesion.

The new cells have a visual resemblance to apocrine glandular cells, for this reason this condition was named Apocrine Metaplasia, these cells can be a palpable mass. Apocrine Metaplasia is frequently seen in women older than 30 years and increases with age [68].

Epithelial Hyperplasia: is a benign proliferative that line the ducts or the milk glands (lobules) inside the breast. In Hyperplasia disease there are two kind of lesions: Ductal Lesions and Lobular Lesions [69].

Ductal Lesions: is proliferative epithelial cells that line the small ducts inside the breast.

Lobular Lesions: is proliferative epithelial cells lining the milk glands (lobules).

Columnar Cell Lesions: represent the substitution of regular layer of cuboid epithelial by columnar cells covering the Terminal Duct Lobular Units (TDLUs), lined by one to several layers of tightly packed, columnar shaped epithelial cells [70] [71].

Phyllodes tumours of the breast: Phyllodes tumors of the breast or cystosarcoma

[1] The enlargement of tissue caused by an increase in the reproduction rate of its cells

phyllodes, are rare fibroepithelial lesions [72]. Affecting women over 40 years old, Phyllodes tumours are presented as a painless mass that can grow quickly. Most phyllodes tumors are benign, but about 1 out of 4 of these tumors are malignant, represent less than 1% of all breast cancers.

Radial Scar: It is characterized by a fibroelastotic center, from which emanate numerous ducts, and lobules in a stellar architectural organization. Radial scar's stellate appearance may mimic carcinoma mammographically and histologically [73].

Intraductal Papilloma: is a benign papilloma characterized by a proliferation intraductal of luminal and basal epithelial cells. Intraductal papilloma can be found in both large ducts of the subareolar region and the TDLU more peripherally [74]. It clinically manifested by serous and bloody discharge.

D. ***Neoplasms***

Fibroadenoma: represent one of the most common benign tumor breast, in which it assimilate approximately one-third of all benign breast lesion of the female. Fibroadenoma made up of both glandular tissue and stromal (connective) tissue, and it appear as small firm and rubbery mass that moves easily and whose contours are well defined. Usually it occur in women in second and third decade of life [75] [76].

Lipoma: is benign tumors, it manifest as a lump under the skin that occurs due to an overgrowth of fat cells, it usually solitary tumor and isn't tender.

Adenoma: is a pure epithelial proliferative neoplasm, but is considered benign, the most common lesion of adenoma are tubular adenoma and lactating adenoma.

Tubular adenoma present as firm mass, is a proliferation of packed tubular structures within a small amount of fibrous stroma, it occurs in young women.

Lactating adenoma present as painless breast mass, palpable that undergo rapid growth, it occurs in the postpartum period [62].

Hamartoma: know also as fibroadenolipoma or adenolipoma, it is smooth, painless lump composed by the overgrowth of mature breast cells of fatty, fibrous and gland tissues [62][77].

1.6.2 Malignant breast lesions

There are several kinds of breast cancer, where two categories of breast cancer were defined *Non-invasive breast cancers* and *Invasive breast cancers*.

A. ***Non-invasive breast cancers***

Also know by carcinoma in situ, the breast cancer starts in the milk ducts or lobules and it do not grow to other part of breast tissue. In this category there are Ductal carcinoma in situ and Lobular carcinoma in situ.

Ductal carcinoma in situ (DCIS): DCIS is a non-invasive cancer that stays inside the milk duct, it can spread along the ducts and gradually affect a substantial area of

the breast. This type accounts for 85% of carcinoma in situ and 20 to 30% of breast cancers [78].

Lobular carcinoma in situ (LCIS): LCIS is an overgrowth of cells that stay inside the lobule. Lobular carcinoma in situ accounts for 1 to 2% of breast cancers and it can be developed to invasive breast cancer in either breast [78].

B. ***Invasive breast cancers***

Also know by infiltrating, in opposite to non-invasive breast cancers, the cancer cells invaded into the neighboring breast tissue as fatty and connective tissues or can be spreading to other organs. In this category there are different types of breast cancer, we will present each of them successively.

Invasive ductal carcinoma (IDC): IDC represents 8 in 10 of invasive breast cancers [79]. It starts in the milk ducts, the cancer cells breaks through the wall of duct and intrude the nearby breast tissue. In some cases, it may be able to spread (metastasize) to other parts of the body. The spread of cancer cells occurs first through the lymphatic system and the first metastases are localized in the lymph nodes adjacent to the affected organ. This is known as lymph node metastasis or regional metastatic adenopathy. The dissemination of cancer cells by blood is usually delayed and may lead to the formation of metastases in organs distant from the site of origin such as the liver, lungs or bones. This is known as visceral metastases or secondary cancers.

Papillary Breast Cancer: is a very rare type of invasive ductal breast cancer, when it is infiltrating it represent less than 1 to 2% of all invasive breast cancers. It tends to occur in older women. When the cells are looked under microscope they appear as finger-like projections, from this it called Papillary Breast Cancer [80].

Mucinous (Colloid) Breast Cancer: Colloid is a rare type of invasive ductal breast cancer that accounts for less than 2% of all breast cancers. The tumor is made up of cancer cells that secrete mucus and may contain also typical invasive ductal cells. It develops more often in women aged 60 to 70 years [81].

Invasive lobular carcinoma (ILC): ILC represents 1 in 10 of invasive breast cancers [79]. It manifest like IDC except that the cancer cells starts in lobules (the milk producing glands).

Inflammatory breast cancer (IBC): Inflammatory breast cancer presents 1% of all breast cancers, but it is fast growing and often fatal [78]. The cancer cells block the lymphatic vessels in the skin of the breast, this cause symptoms of inflammation hence its name: Inflammatory breast cancer. Among the symptoms there are: breast swelling, warming, thickening and red color of the skin [79].

Paget Disease of the Breast: Paget's disease of the breast is a rare type of breast cancer. It affects the skin of the nipple and the areola, it appears as a rash, crusted, scaly and red. Paget's disease of the breast affects more women over 50 years old and

women having infiltrating ductal carcinoma or ductal carcinoma in situ [82].

Angiosarcoma of the Breast: present 0.05% of all breast cancers, starts in the cells which line the blood vessels or lymph vessels of the breast. There are two types of angiosarcoma: A primary angiosarcoma it manifests in women age 30-50 years who have never had any treatments for breast cancer. In contrast, the secondary angiosarcoma, it manifests in woman age 67-71 years, who has already had treatments for a primary breast cancer [83].

1.7 Diagnosis of breast cancer

Finding breast cancer early and getting treatment are the most important strategies to prevent deaths from breast cancer. The symptoms can help to detected and diagnosis the breast cancer, in the next paragraph we give the common symptoms of breast cancer.

1.7.1 Symptoms of breast cancer

The symptoms of breast cancer are all abnormal manifestations caused by this disease, the most frequent symptoms are :

- A lump in a breast or underarm is the sign of the most commonly observed breast cancer.
- Changes in breast skin and the mamelon: irritation, redness and dimpling of breast skin.
- Any change in the size or shape of the breast and the nipple.
- Nipple discharge without being compressed or tinged with blood.
- Pain in any area of the breast.

Late symptoms occur when the cancerous mass grows or spreads to other parts of the body, including other organs:

- Bone pain
- Weight loss
- Nausea
- Loss of appetite
- Jaundice

- Breathlessness
- Cough
- Headache
- Double vision
- Muscular weakness

These symptoms do not necessarily mean that it is breast cancer, because they can happen with other conditions and many women with breast cancer have no symptoms.
Fortunately different tests can be used to look for breast cancer such as mammography, breast ultrasound, magnetic resonance imaging (MRI) and biopsy. All these techniques will be introduced in the following section.

1.7.2 Imaging tests

A. ***Mammography***

Mammography is a low dose X-ray of the breast. The image obtained by mammography is called a mammogram. It can help to detect cancerous and noncancerous tumors in the breast. A mammogram can be performed either as part of a breast cancer screening named screening mammography or in the presence of symptoms named diagnostic mammogram.

Screening mammogram: is a screening test that is used for women who have no symptoms of breast cancer. In this mammogram, both breasts are examined. This test can help to detect abnormal lumps or areas of breast tissue that may be too small to be detected by palpation.

Diagnostic mammogram: is performed when a patient has symptoms suggestive of breast cancer such as nipple discharge, redness of the skin and lumps in the breast,etc. This mammogram includes a basic mammogram and additional pictures centered on the suspect areas.

B. ***Breast ultrasound***

Breast ultrasound is performed following a mammogram when it showed an abnormality. In this case, the ultrasound allows the radiologist to analyze more finely this anomaly.

Breast ultrasound is recommended, when the density of the breasts does not allow to obtain a good quality of mammogram, this is the case in some young women and also is used in the case of pregnant women for the reason that the mammography are contraindicated because the X-rays.

Figure 1.9: Mammography machine

C. ***Magnetic resonance imaging (MRI)***
For women with breast cancer, MRI is used to determine the size of the cancer and it growth, and also to evaluate the response of chemotherapy performed before the operation. In screening women at high risk for breast cancer, MRI is recommended with mammography, because MRI can miss some cancers [84].

1.7.3 Other tests

A. ***Biopsy***
When other tests show that there is a possibility to have breast cancer, the breast biopsy is the only way to know for sure if it's cancer.

1.8 Conclusion

In this chapter, we saw the anatomy and physiology of liver and breast organs, a great importance was given to the pathologies including benign and malignant lesions. In the liver pathologies diagnosis, the CT image technique gave an important information to the clinical evaluation of liver disease. In other side, in the breast pathologies diagnosis, the mammography is the most technique used to identify malignant lesion and the biopsy represent the only way to know for sure if it's cancer. For these reasons we were interested by studying and analyzing these kind of modalities, CT for liver, mammogram and histological images for breast. More details about this studies are given in the next chapters.

Chapter 2

State of the art

2.1 Introduction

Advancements in medical technology has given rise to produce a huge number of medical images from different medical imaging techniques such as mammography, digital microscopic images, etc. Consequently, this laying a great challenge to manage, store and retrieve these images. Computer-aided detection and diagnosis CADe/CADx systems are developed to assist the physicians in the diagnosis process. This is achieved by automating some tasks and by giving their diagnostic opinion, using a set of image analysis methods and machine learning techniques [85] .

In this chapter, we will present the methods proposed to be used in CADe/CADx systems for liver computed tomography (CT) images annotation, breast density classification using mammogram and breast histopathological image classification. In the next section, we will present the related works proposed to annotate liver CT images including the methods proposed for ImageCLEF challenge. In section 2.3 we will review the related works on breast density classification using digital mammography.
In section 2.4 we will present the works related to the classification of the histopathological images. Where, we will focus on the methods that classify the tumor kind as malignant and benignant at the first time. Secondly we will review the methods proposed in International Conference on Image Analysis and Recognition (ICIAR) Grand Challenge on **B**re**A**st **C**ancer **H**istology image (BACH), that aim to automatically classify breast histology images in four classes: normal, benign, in situ carcinoma and invasive carcinoma.

2.2 Liver CT annotation

The liver lesion annotation is one of the recent research branches in the medical field, since it contributes to improve the diagnostic by providing accurate details about lesions. Despite that, the liver image annotation is a hard task where a few CAD system have been developed [86]. Generally, the liver CAD systems can contain several modules such as liver, vessels and lesions segmentation module that allows to define the regions of interests (ROIs), liver

tissue and tumors classification modules and annotation module.

According to [87] the segmentation methods are repartitioned into two approaches: the grey level and the contour-based approaches.

From the grey level approaches we found the region growing method, clustering method and threshold method. In the liver segmentation, the region growing method is the most used [88] [89]. In other side, the lesion segmentation are gotten using the clustering method such as k-means [90] and fuzzy c-means [91]. In addition to the threshold method [92] [93]. The vessels segmentation are given using region growing method [94] [95] and clustering method like fuzzy c-means [96].

The contour based approaches contain the deformable models and graph cut models. In the literature review, the deformable models are used to segment the liver [97] [98], the lesion [99] and vessels [100]. In other side, the graph cut models are used for liver [101] [102], lesion [103] and vessels segmentation [104].

In addition to these approaches, deep convolutional neural networks approaches are also used for liver segmentation [105] and liver tumor segmentation [106].

The segmentation methods can be manual, semi-automatic and fully automated. In the manual segmentation, the radiologist marked the region of liver and lesion by using a software made for this task such as Physician Annotation Device (iPAD) [107], the authors in [9] [108] used iPAD for liver lesion segmentation. In the semi-automatic segmentation the radiologists partially intervene by initializing the seeds pixels of the region of interest for automatic segmentation [109] or by guiding the segmentation using an interactive process [103]. The fully automatic segmentation is more challenging because the image with low contrast is much difficult to segment, in addition no radiologists intervene, yet if it will be carried out successfully it be helpful for them because it saves time.

In CAD systems there are liver tissue and tumor classification modules. To achieve the two tasks of classification, the most modules used the low level features extracted from the region of interest and feed them into machine learning methods for classification. In general, the low level features can be texture features, shape features and colors features, more precisely intensity features since the medical image are usually in grayscale. In addition to this features, the bag of visual features is also used to describe the liver lesion.

In the literatures, we found the methods developed for liver tissue classification such as the method proposed by Mir in 1995 [110] which is based on texture features to classify liver CT tissues into normal and abnormal tissue with malignancy. In [111] the authors classify the liver into fatty and cirrhosis. A further interesting goal to classify the liver CT tissues was given by [112], where they studied the altered liver tissue in CT image for patients with colorectal cancer.

In other hand, several methods for liver lesion classification have been developed. We can categorize them according to the type features used. For example, Safdari et al. [113] and in the researches given by Diamant et al. [114] [115] used the bag of visual word histogram

to classify the lesions into cyst, haemangiomas and metastases.
The First Order Statistics (FOS), Co-occurrence Matrices (COM), Gray Level Difference Matrices (GLDM), Laws Texture Energy (LTE) are used both by Stoitsis et al. [116] and Mougiakakou et al. [117] to categorize the liver lesion into normal, cyst, hemangioma and Hepatocellular carcinoma (HCC).
Ganeshan et al. [112], Ye et al. [118] and Chi et al. [119] used only COM, FOS to classify the lesion into the adequate categories, indeed Chi et al. [119] used 7 classes of lesions namely: HCC, metastases, hemangioma, cysts, liver abscess and focal nodular hyperplasia.
The Gray-Level Co-Occurrence Matrix (GLCM) features was the largely used to classify different types of lesions [120][121] [122].

Despite the lesion classification is important, but in the reality the medical images contain more information. In fact, for several years radiologists annotate manually these images by creating a structured reports. Indeed, many factors contributed to make this task difficult such as the subjectivity in the annotation because it depend on radiologists experience and the errors due to the perceptual misinterpretation [123].
Fortunately, to overcome this problems many solutions have been proposed, such as the development of ontologies like Onlira [124] and RadLex [125] that contain a structured vocabularies of the radiology field. With these ontologies, the radiologic reports will be more standardized, they contribute also to reduce the misinterpretation with less semantic gap between the low and high level features. The liver functional annotation system is based on lesions and vessels structure and their anatomical relationship with the liver that can be described by ontological terms or graphic representation.

We have chosen to work on liver annotation more precisely on the CT images, as it is already mentioned in the literature [126], that in this modality the liver lesions and metastases are mostly identified and diagnosed.

2.2.1 Related works

In this section, we will present literature methods that annotate the liver properties, vessels and lesions. We have noticed that the vast majority of the works have been concentrated on the annotation of lesions, this comes back to their importance in the diagnosis, a summary of the works carried out is presented in Table 2.1.

Year	Author(s)	No. of Images	Name of Dataset	Methods	Accuracy (%)
2010	Napel et al. [108]	30	Private dataset	AdaBoost	NDCG=95
2011	Korenblum et al. [127]	74	Private dataset	Distance of imaging observation characteristics	ROC=0.92
2012	Gimenezet et al. [128]	79	Private dataset	LASSO	81.6
2013	Agarwal et al. [9]	278	Private dataset	Auto-encoders	p-value= 0.74
2014	Depeursinge et al. [123]	74	Private dataset	SVM	ROC = 0.85
2014	Spanier and Joskowicz [129]	50	ImageCLEF 2014	LDA,LR, KNN,SVM	91
2014	Ermis and Cemgil [130]	50	ImageCLEF 2014	GCTF	88
2015	Kurtz et al. [131]	72	Private dataset	Distance	AUC 0.79
2016	Chen et al. [86]	50	MICCAI 2007	Vessel-tree	volumetric overlap error= 4.16
2016	Kumar et al. [132]	50	ImageCLEF 2014	SVM, weighted nearestneighbor	91
2018	Spanier et al. [126]	50	ImageCLEF 2014	SVM	NDCG= 84
2018	Alahmer [87]	174	Private dataset	SVM	95.56
2020	Loveymi et al. [133]	50	ImageCLEF 2015	Random subspace (RS) + kNN	93.1
2020	Pan et al. [134]	64	Private dataset	Vessel skeletonization	-

Table 2.1: Brief overview of different studies carried out on liver CT annotation

Napel et al. [108] proposed a content-based medical image system that retrieve similar radiology CT images to a query image, in order to annotate its liver lesions. The radiologists circumscribe the ROIs lesions from 30 portal venous phase CT images, and annotated them into 12 lesions categories by using 161 semantic features terms selected from the ontology RadLex. The lesions categories are : overall lesion shape, lesion margin and contours, lesion rim or capsule, lesion focality, overall, uniformity within lesion, overall within lesion, spatial pattern, temporal features, lesion substance, lesion effect on liver, miscellaneous lesion findings. In fact, the radiologists constructed a semantic features descriptors of size 161 contain a binary value (present or absent of semantic features). In addition, the authors extracted 46 texture features (14 histogram features and 32 Gabor features) and two boundary features in total 209 features were used. Finally, adaptive boosting algorithm with similarity measure were used for retrieval.

Korenblum et al. [127] built Biomedical Image Metadata Manager (BIMM) system to search, retrieve and annotate liver's lesions. Image metadata contain all information about image modality, acquisition parameters, annotations created by radiologists and the regions of interest (ROIs). BIMM is a Web-based application composed of controller module and database. The radiologists used iPAD to select ROIs and generate AIM files (Annotation and Image Markup standard) that contain the anatomy, imaging observations (e.g., mass), imaging observation characteristics (smooth margins) and diagnoses type.
The diagnosis type include: cyst, metastasis, hemangioma, hepatocellular carcinoma, focal nodular hyperplasia, abscess, laceration, fat deposition.
BIMM receive the AIM file through web service, and the controller module charge to store into a database. In the test phase, the user can query BIMM for image metadata using text or image as input via web browser. The text query return the query results matching anywhere in the AIM image metadata. In other side, image query search for image containing similar lesion based on image observation characteristics, then the images returned are ranked according to similarity matching.

Gimenezet et al. [128] presented a framework for liver lesions annotation using a set of hand craft features classified by L1-regularized logistic regression. The ROIs were extracted from 79 CT images of liver lesions in the portal venous phase and annotated by a radiologist. The types of lesions used in this study are: hepatocellular carcinoma, metastasis, hemangioma, focal nodular hyperplasia, abscess, laceration, fat deposition and cyst.
The following semantic features from RadLex ontology are used to create a binary semantic annotation vector (positive or negative observations) of size 30 for each ROI: smooth margin, ovoid, normal perilesional tissue, homogeneous, heterogeneous, enhancing, solitary lesion, non enhancing, homogeneous enhancement, hypodense, circumscribed margin, round , multiple lesions 1-5, lobular, homogeneous fade, multiple lesions 6-10, peripheral discontinuous nodular enhancement, multiple lesions >10, homogeneous retention, centripetal fill-in, soft tissue density, poorly-defined margin, abuts capsule of

liver, water density, hypervascular, irregularly shaped, irregular margin, heterogeneous enhancement, lobulated margin, internal nodules. The authors extracted 431 features of texture, shape, contrast and edge. From texture they used histogram and its features such as peak, entropy, and variance. Also they extracted the low frequency coefficients of 3-level Haar wavelet transform, the features of Daubechies wavelet transform and Gabor features. The shape features include compactness, roughness, local area integral invariant, radial distance signature. The contrast features used are proportion of pixels with intensity larger than threshold and difference of means, for the edge they used edge sharpness and histogram on Edge.

Agarwal et al. [9] implemented an auto-encoders with one hidden layer for liver's lesion annotation. The authors used 4491 patches extracted from 504 ROIs lesions of 278 images. The lesions were annotated with the same 30 binary semantic features used by Gimenezet et al. [128]. The auto-encoders received as input the patches and train to generate the semantic features vectors (e.g. the lesion is heterogeneous or not).

Depeursinge et al. [123] built a framework that model the visual liver lesions using visual semantic terms (VST). The authors used a private dataset composed of 74 ROIs extracted by a radiologist and divided into a set of 12×12 patches. These patches were extracted from the margin and the internal texture of the lesion, in order, to define the 18 VSTs describing the peripheral and internal lesion. The 18 VSTs are introduced in RadLex ontology and distributed into 7 lesion categories. Lesion margin: circumscribed margin, irregular margin, lobulated margin, poorly-defined margin, smooth margin. Lesion substance: internal nodules. Perilesional tissue characterization: normal perilesional tissue. Lesion attenuation: hypodense, soft tissue density, water density. Overal lesion enhancement: enhancing ,hypervascular, nonenhancing. Spatial pattern of enchacement: hererogeneous, homogeneous, peripheral discont. Lesion uniformity: heterogeneous, homogeneous.
To predict the likelihood of VSTs in ROIs, the authors used the features of steerable Riesz wavelets, which are learned using Support-vector machine (SVM).

Spanier and Joskowicz [129] tested four classifiers to predict the liver's annotations of the ImageCLEF liver CT annotation challenge 2014. Wherein, from the four classifier namely the linear discriminant analysis (LDA), logistic regression (LR), K-Nearest Neighbors (KNN), and SVM. The LDA and KNN were selected as their exhibits annotation precision. We note that the ImageCLEF liver CT annotation challenge 2014 provide a dataset of 50 CT images (50 training and 10 testing) with 73 liver and liver lesion annotations available for experiments, in addition to a set of local and global features extracted from the images. The authors selected 39 features that are: Liver volume, liver mean, liver variance, vessel ratio, vessel volume, min lesion volume, max lesion volume, lesion ratio, all lesions mean, all lesions variance, all lesions skewness, all lesions kurtosis, all lesions energy, all lesions smoothness, all lesions abcssia, all lesions entropy, all lesions threshold, number of lesions, lesion mean, lesion variance, lesions kewness, lesion kurtosis, lesion energy, lesion

smoothness, lesion abcssia, lesion entropy, lesion threshold, lesion2vessel min distance, lesion2vessel touch ratio, vessel total ratio, vessel lesion ratio, volume, surface area, max extent, aspect ratio, sphericity, compactness, convexity, solidity. The authors added 9 features: the average and the standard deviation of the gray level intensity values of the healthy part of the liver, the average and the standard deviation of gray level intensity values of the lesion, the mean and the standard deviation of the lesion's contour gray levels, the average gray level difference between the healthy part of the liver with the lesion and lesion's contour, the average gray level difference between the lesion and its contour.

Ermis and Cemgil [130] used Generalized Coupled Tensor Factorization (GCTF) that represent a generalization of the Probabilistic Latent Tensor factorization models to annotate the liver CT images. The annotations problems was formulated as matrices factorization by extracting common latent factors. For this purpose, the ImageCLEF2014 liver CT dataset was represented in the form of matrices and the GCTF framework was used to develop coupled factorization of these matrices to fill the liver, vessels and lesions annotation. The authors used the Kullback–Leibler (KL) divergence and the Euclidean distance as cost function.

Kurtz et al. [131] proposed a system for liver CT annotation and retrieval based on the similarities of both image features and ontological inter-term in addition to the user feedback.

The system was composed on five steps, in the first step, the radiologist extracted 72 ROIs lesions and annotated them using 18 RadLex terms distributed into 8 categories: lesion margin and contour, lesion substance, perilesional tissue, lesion attenuation, overall lesion enhancement, spatial pattern of enhancement, lesion uniformity, lesion effect on liver. Thereafter, each ROI was divided into a set of 12×12 patches and the energies of multi-scale Riesz wavelets were extracted to represent the terms' visual signatures.

The second step was dedicate to the computation of the global term similarities by combining image-based term similarity and semantic term similarity (ontology). In fact, in the image-based similarity the Euclidian distance was used to compute the distance between the visual signatures of the given terms. In other hand, semantic term similarity was computed using hierarchical and depth distance between the terms in the ontology. The global term similarities was used to fill a symmetric term similarity matrix that model the similarity between all the terms. These two steps are included in the offline phases.

In the step three of the online phase, the visual signatures of each term of the training data are used to automatically annotate the content of the ROI lesion of the query image by defining the semantic feature vector.

The step four consist to retrieve similar image to the image query using the hierarchical semantic-based distance (HSBD) [135] and the similarity matrix .

Finally, according to the user feedback on the retrieved image, the authors applied a penalty algorithm to advantage the relevant image and disadvantage the irrelevant images.

Chen et al. [86] presented a vessels tree method for functional segments annotation of liver CT image. The method was based on determining the topology of portal veins, where through its branches they can obtain the liver segments and conduct to annotate the liver's regions. In the first stage, the authors segment the liver and the tumor regions using graph cut algorithm. Thereafter they applied the Hessian filter to segment the vessel regions. The vessel skeleton was extracted from the vessel regions using 3D thinning algorithm, thereafter it was formulated by graph then to a vessel trees. The authors categorized the vessel trees into two sub-trees. The First one, contain the main vessels of liver portal vein with a large radius branches, while the second sub-tree contain small radius branches. As the second sub-tree present the distribution of vessels system, the authors used K-means to cluster the vessel tree, K was equal to 8 according to the number of functional segments. After that, the authors used the Euclidian distance between each voxel in the liver with a branch to identify the region of the voxel. Finally the clinical features are extracted include the global and individual features. As the global features they extracted the size of liver, vessels, and lesions, as well as the ratio of each segment to liver. The individual features include the anatomical locations, such as the spatial relationship among vasculature, lesions, liver, and the segments in which the lesion resides. These clinical features are used to generate a structured report for liver annotation, in addition the authors provide functional segments visualization.

Kumar et al. [132] proposed a method for automatic annotation of liver CT images. The authors used 3D-CT images of the liver from the ImageCLEF 2014 Liver annotation challenge, this dataset contain 50 images for training and 10 images for test, it included 73 concept to be annotated and a set of texture and shape features extracted from the liver, the hepatic vasculatures, and lesions. The texture features are Haralick, Gabor, Tamura and Haa. The shape features contain volume, surface area, sphericity, solidity, convexity, Hu shape invariants. The features with missing values or that had no variation across all images were excluded by the authors and the number of features used was 446. In addition, they extracted a bag of visual features descriptors from the training images by applying k-means on the features derived from the scale invariant feature transform (SIFT), then 1000-bin histogram was defined. The retrieval strategy was decomposed into two stages for each concept to be annotated. The first stage, they extracted the collection of annotations from the similar training images to the image test and in the second stage they selected the best answer from the obtained collection. The authors tested the classifier SVM and weighted nearest-neighbor (WNN) for retrieval. In the case of SVM, the first stage was composed of the 1-vs-all SVMs and the second stage was composed of the 1-vs-1 SVMs. In other side, the first stage of WNN approach consist to retrieve the nearest-neighbors images by using Euclidean distance and in the second stage a weighted voting scheme was used to select the best annotation for each concept. The best result was obtained using SIFT descriptors with WNN method.

Spanier et al. [126] developed an automatic method for content base liver CT images retrieval, that restore the most similar liver lesion annotations to a test image. The method was composed of segmentation module, features extraction and similarity measure. In the segmentation module 3D region growing using super pixel was applied. Thereafter, the normalized gray level histogram of 60 bins was used as features vector of the segmented liver. The authors used the images of ImageCLEF2014 Liver annotation dataset and only three groups of lesion semantic annotation:
Lesion contrast: homogeneous or heterogeneous
Lesion composition: solid
Peripheral localization: smooth and encapsulated or infiltration
The remarkable contribution of their work is the use of SVM to compute the weight of each bin to identify each annotation. In the test phase, a weighted comparison measure was performed between the image query descriptor and the dataset descriptors.

Alahmer [87] proposed a full system for liver lesion annotation and classification. The system include the segmentation module that segment the liver using histogram-based adaptive threshold and morphological operations, thereafter the region growing process is used to extract the lesions and vessels. The authors proposed multiple ROIs selection approach using intensity difference, then for each ROI a set of lesion characteristics were extracted. The lesion characteristics consist of the high-level features that are composed of features extracted from the image contents and the features inferred from the low-level features through the machine learning SVM.
In total 85 semantic terms are used to annotate 21 high-level features of 174 CT scan liver lesion. The high-level features are: lesion density, lesion density type, lesion rim, lesion rim thickness, contrast uptaken, enhancement pattern, lesion composition, lesion leveling type, lesion shape, lesion focality, lesion margin, lesion margin definition, lesion enhancement, lesion brightness, lesion surrounding, calcified (inside lesion), calcified wall, scar, lobe, segment, close to vein.

Loveymi et al. [133] investigated a set of handcrafted features to annotate liver CT images by producing an organized structured report. The handcraft features include shape descriptors like area, moments, circularity, solidity, weighted centroids, major and minor axis lengths and eccentricity. As texture descriptors they extracted 48 features from 3D GLCMs using four direction 0°, 45°, 90° and 135° and distance equal to 1. In addition, 24 means and 24 standard deviation features obtained from the 3D Gabor wavelet transform were used. Furthermore, a coding histogram obtained from the quantization of Speeded Up Robust Features was used (SURF). Besides to that, the authors proposed a new descriptor named Deep Local Binary Pattern (DLBP). The DLBP are based on Local Binary Patterns (LBP), where a set of LBP histograms were computed from multi-slide liver image, thereafter computed the covariance matrix of the LBP histograms, and from it they extracted the Rotation Invariant LBP histogram (RILBP). In order, to select the appropriate features for

each annotation the RSKNN that represent Random subspace (RS) with kNN was used, as well, the SVM in the classification step. Using the dataset from ImageCLEF 2015 liver CT annotation task, the obtained result showed that RSKNN outperform the SVM.

Pan et al. [134] proposed a liver annotation system based on improved vessel-skeletonization method. First, the authors segment the liver and it vessels, then the skeleton vessels are extracted from vessels regions, thereafter the liver's segments are defined using the connectivity of skeleton vessels. To process the segmentation of liver from the CT images, the level set method was used, where the seeds points can be were up manually by the user or automatically. For vessel segmentation they used regional growth algorithm with a manual seeds initialization. The main contribution of the authors was the introduction of the modified iterative thinning-based vessel skeletonization, where the voxel on the surface of the vessels are deleted in the iterative thinning objects. The hepatic portal vessel skeleton was transformed into a tree-shape data structure, where each tree node is marked according to it the portal vein branch. Finally the authors used a proposed nearest neighbor segment approximation distance to identify the liver's segments. Based on these segments, the liver annotations extracted are: the number of voxel in a segment, the volume ratio of segment to liver, the average volume information of the lobes.

In the next section we will present the works related to breast density classification.

2.3 Breast Density classification in digital mammogram

The mammography is one of the common examination techniques to detect breast cancer. The radiologists look for different features from a mammogram such as breast density, masses and calcifications to detect breast abnormalities.
Several methods for CADe/CADx systems have been developed during the last decade to accurate radiologists in their diagnostic. This methods are developed to detect breast lesion abnormalities, or to classify breast density that can conduct to the detection of abnormalities [136].

In state of the art, the methods based on lesion detection are partitioned on two axes: the first one, masses segmentation and classification, the second is calcification detection and classification.
To segment masses, the presented methods in [137] [138] [139] used machine learning approaches, indeed the deep learning methods were used to segment masses [140] [141] [142] and to classify the shape of masses as irregular, lobular, oval and round [142]. Some works [143] [144] [145] focused on detection and identification of masses types that can be classified as benign or malignant.
The calcification is a breast lesion that could be micro-calcification or macro-calcification. The micro-calcifications are represented by a small calcium deposit, if they have a regular shape they will be considered as benign lesion other way as malignant lesion. The macro-calcifications are represented by a large calcium deposit that are considered noncancerous lesions. The works related to the calcification include a proposed automatic computer detection of clustered calcifications in [146] and calcification descriptor for content-based mammogram retrieval given in [147] . In other side, the research are more involved in micro-calcifications detection and classification than the macro-calcification. From the solutions given for the micro-calcifications detection there are [148] [149] [150] and for micro-calcifications classification there are [151] [152].

We come back to the state of the art methods. Indeed, there are some researchers that have been focused on developing CAD systems for breast tissue density classification. Specially because the increase in breast tissue density is associated with breast cancer risk. In fact, according to Sprague et al. [18], more than 30 states in the united states have agreed to use breast density as a marker for prior cancer risk, where they made breast density notification legislation [153]. In addition, differentiate between different breast tissue density classes is considerably difficult specifically for atypical cases, that makes CAD systems helpful for the radiologists. These points were motivated us to work on the breast density classification, in addition this work was not done by the research groups in our laboratory.

The following section we will present the studies carried out on breast tissue density classification.

2.3.1 Related works

The relation between breast density and the risk to develop breast cancer overcome to 1976, where Wolfe [154] was the first that validate this correlation based on the study carried on 7214 patients.

Wolfe [154] defined four groups of risk for developing breast cancer (N1,P1,P2,DY).

N1: tissue composed primarily of fat and no ducts visible (represent lowest risk).

P1: tissue chiefly fat with prominent ducts in anterior portion up to one-fourth of volume of breast (represent low risk).

P2: prominent duct pattern occupying more than one-fourth of volume of breast (represent high risk).

DY: is a dysplasia, minor component of prominent duct pattern (represent highest risk).

Another classification was given by Tabár and Dean [155] based on a combination of four mammographic features:

Nodular (N): represent the terminal ductal lobular units.

Linear (L): represent either ducts or fibrous or blood vessels.

Homogeneous (H): represent fibrous tissues.

Radiolucent (R): represent adipose fatty tissues.

Tabár and Dean defined five risk levels based on the distributions of the four features [N%,L%, H%, R%]: TI [25%, 15%, 35%, 25%] is the lowest risk, TII [2%, 14%, 2%, 82%], TIII is similar to TII except that the ducts are often associated with fibrosis, TIV [49%, 19%, 15%, 17%], TV [2%, 2%, 89%, 7%] is the highest risk.

The American College of Radiology (ACR) [156] proposed the classification Breast imaging-reporting and data system (BI-RADS) to standardize mammography reporting. The classification BI-RADS is the most used, covers the significant relationship between density and cancer in the breast. The four breast compositions were defined as follows:

- BI-RADS I: almost entirely fatty breast (0 - 25%)
- BI-RADS II: some fibroglandular tissue (26% - 50%)
- BI-RADS III: heterogeneously dense breast (51% - 75%)
- BI-RADS IV: extremely dense breast (76% - 100%)

The proposed method classify the breast tissue into four BI-RADS classes. In addition, as well was reported in [157] the classification of breast tissue into the two classes fatty and dense in the atypical cases is a hard task even for experienced radiologists, for this reason our method is also used to classify these types of tissues.

A brief description of the methods proposed to classify breast tissues are showed in Table 2.2, each of them is detailed next.

Year	Author(s)	Number of classes	No. of Images	Name of Database	Methods	Accuracy (%)
1998	Karssemeijer [158]	04	615	Nijmegen	KNN	67.0
2002	Bovis and Singh [159]	04	377	DDSM	Multiple classifiers ANN	71.4
2003	Petroudi et al. [160]	02	132	Oxford	Nearest neighbor	92.5
		04				75.7
2005	Oliver et al. [161]	04	300	DDSM	KNN+ ID3	47.0
2006	Bosch et al. [162]	04	500	DDSM	KNN,SVM	84.75
2007	Castella et al. [163]	02	352	Collected	LDA	88
		04				83
2008	Oliver et al. [164]	02	322	MIAS	Bayesian	91
		04	831	DDSM		77
2011	Liu [165]	04	88	T.Hospital	SVM	86.4
2011	Z.Chen [166]	02	322	MIAS	KNN	88.0
2012	Muštra et al. [167]	02	322	MIAS	Naïve Bayesian	91.6
			144	KBD-FER	KNN	97.2
2013	Masmoudi et al. [168]	04	400	EL Farabi	ANN	79.0
2016	Kriti et al. [169]	02	322	MIAS	SVM	94.4
					PNN	92.5
2016	Virmani and kriti [170]	02	322	MIAS	KNN	96.2
2017	Ahn et al. [171]	02	397	Private dataset	CNN	Correlation coefficient=0.96
2018	Xu et al. [172]	02	409	INbreast	CNN	96.8
		04				92.6
2018	Mohamed et al. [173]	02	22000	Private dataset	CNN	AUC= 0.98
2018	Wu et al. [174]	02	201179	Private dataset	CNN	86.5
		04			CNN	76.7

Table 2.2: Brief overview of different studies carried out on different mammographic images databases for two-classes and four-classes breast tissue density classification

Karssemeijer in [158] proposed the use of local region features to classify beast density. The authors construct a method based on hypothesis that a correlation between tissue thickness and distance to the skin exit. For that a set of sub-regions that have the same distance to skin are extracted and the sub-region features were computed from grey level histograms. kNN classifier was used to classify 615 digitized mammograms acquired from University Hospital Nijmegen.

Bovis and Singh [159] have investigated the use a set of textural features with Multiple Artificial Neural Network (ANN) for breast tissue classification. The authors employed four approaches to determine the texture proprieties: the first one, is GLCM using the directions 0°, 45°, 90°, 135° and pixel distances 2, 4, 6 they extract 15 features (angular second moment, contrast, correlation, inverse different moment, sum average, sum variance, sum entropy, entropy, difference average, difference variance, difference entropy, information measure of correlation I, information measure of correlation II, inertia, variance). Secondly, they extracted 10 spectral energy from the power spectrum of the Fourier transform. Thirdly, they computed the total texture energy from the combination of Laws' texture masks with each mammographic image. Finally, by applying the Discrete Wavelet Transform (DWT) four features (standard deviation, mean, skewness and kurtosis) are extracted from 3 different sub-bands at 3 different scales of the transformed image. In addition to these features, they extracted the entropy, standard deviation, mean, skewness and kurtosis from the grey scales breast images. The authors used Principal Component Analysis (PCA) to reduce the dimensionality of features vectors. In the classification step, the set of ANNs outputs expressed in a probabilistic framework, are combined using six combination rules: majority vote, sum rule, max rule, min rule, product rule and median rule. The best result was given by using the product rule.

Petroudi et al. [160] classify the mammographic breast density according to the statistical distribution of tissue patterns. In fact, the authors applied the Maximum Response 8 (MR8) filter bank on 11 mammogram image per BI-RADS class (total 44 images). Then, all filtered responses are aggregated and K-means is used to compute 10 cluster centers per class, thus 40 cluster centers represent the textons dictionary. The authors create a texton histogram for each image based on textons dictionary. At the test time, the test image histogram is compared to all the training images histograms and the class of the nearest neighbor is assigned to the image test.

Oliver et al. [161] proposed a method for breast parenchymal density classification into the four BIRADS scores. At the beginning, the breast region was smoothed with a median filter of size 5×5. Then the authors apply Fuzzy C-Means algorithm to group pixels into separate categories with the aim to obtain representative instances of two classes: normal and dense tissue. Then a set of morphological and texture features for each class were extracted. The morphological features used are the centre of masses and the medium intensity of both clusters. As texture features, they calculated features derived from GLCMs.

With four directions: 0°, 45°, 90°, 135°; and a distance equal to 1, the features extracted are contrast, energy, entropy, correlation, sum average, sum entropy, difference average, difference entropy, and homogeneity features. The authors used 300 Medio-Lateral Oblique right mammograms taken from DDSM. The database is formed of 50 mammograms with BI-RADS I and IV, and 100 with BI-RADS II and III. Two classifiers were testes: the k-NN, Decision Tree classifier (ID3). However, only by using fuzzy combination of the above two classifiers the accuracy was improved.

In 2008, Oliver et al. [164] proposed an improve of their results in [161] by using more features and using a Bayesian combination of a number of classifiers. At set of morphological features for both clusters were calculated including the relative area and the first four histogram moments (mean intensity, the standard deviation, the skewness, and kurtosis). They also added more GLCMs, in which they used four different directions: 0°, 45°, 90°, and 135°, and three distances equal to 1, 5, and 9 pixels. For each GLCM, the following features were used: contrast, energy, entropy, correlation, sum average, sum entropy, difference average, difference entropy, and homogeneity features.
The classification was performed by using the kNN, the decision tree classifier C4.5 instead of ID3, and Bayes classifier based on the combination of the first two classifiers. The best results was obtained using Bayesian combination.

Bosch et al. [162] used textons descriptors with probabilistic Latent Semantic Analysis (pLSA) to classify breast parenchymal tissue. In fact, they extracted a texton around each pixel, then they created a bag-of-words using k-means. Next, pLSA is applied to automatically find the tissue distribution for each mammogram. Finally the authors tested SVM and KNN to classify the tissues distribution and the best result was obtained using the SVM classifier.

Castella et al. [163] proposed a semiautomatic method for breast tissue density classification. Firstly, the radiologists extracted four ROIs per mammogram of size 256×256 pixel, chosen from the central breast region. Then, the authors extracted a set of different statistical quantities from each ROI. These features involve from the gray level histogram like the standard deviation, skewness and kurtosis. They also extracted 20 GLCMs from each ROI using four directions of 0°, 45°, 90°, 135° and five distances of 1, 3, 5, 7, 9 and they computed the following features: energy, entropy, contrast, and homogeneity. From the Primitive Matrix (PM) they derived the Short Primitive Emphasis (spe), the Long Primitive Emphasis (lpe), as well as Gray Level Uniformity (glu) and Primitive Length Uniformity (plu). They also used the fractal dimension and the coarseness, contrast, complexity, and strength provided from the Neighborhood Gray Tone Difference Matrix (NGTDM). The authors used three Bayesian classifiers based on the measure of Mahalanobis distance, a naïve Bayesian, and LDA. The dataset used for the experiments consisted of 352 digital mammograms collected at the Clinique des Grangettes, Geneva, Switzerland. The best results was given by the classifier LDA.

Liu et al. [165] proposed a sub-region based method for breast density prediction using 88 full field digital mammograms (FFDM) provided by Tianjin tumor hospital. Firstly, from each image the authors extracted a set of sub-regions of size 128×128 without overlapping and for each region they computed the histogram moments descriptors. Thereafter, they used the SVM classifier to classifier these regions, the SVM was trained on 400 sub-regions which contained 200 high density sub-regions and 200 low density sub-regions from the whole set of all images. Finally the mammogram density is assigned to the image by computing the ratio number of high density sub-regions to the whole set sub-region of the image.

Chen et al. [166] investigated the potential application of five local feature for breast density classification. These features are LBP, Local Grey level Appearances (LGA), Basic Image Features (BIF), Texton I and Texton II.
In Texton I, they used the MR8 filter bank to map each pixel within the breast area into 8 dimensional filter response space. In fact, the filter responses over all the training images from each class were aggregated and clustered using K-Means, then these centres (textons) are gathered together into the texton dictionary. Subsequently, the textures are modeled by the frequency histogram of textons.
In Texton II, they extracted 3 × 3 image patches around each pixel within the breast area and rearranged these image patches into 9 dimensional feature space, then they sorted the 160 textons extracted from the training set according to the magnitude value in ascending order, and then labeled each breast tissue pixel by the nearest texton. The authors used the KNN for the classification and MIAS database for evaluation. The best classification result was obtained by Texton II, followed by LGA, providing the second-best result, while LBP performs worst among these five approaches.

Muštra et al. [167] used a set of first and second order grayscale features to predict breast density. In fact, from each image the authors extracted a ROI of size 512×384, then the following features were computed: the number of pixels with higher intensity than the mean intensity of the muscle region, the higher intensity than Otsu's threshold, standard deviation, entropy, skewness, kurtosis. They extracted also multi-resolution histograms with 8,16,32 and 64 bins and four features: the mean, standard deviation, skewness, kurtosis from 256 bin histograms. From the mammogram they extracted the Haralick and Soh from GLCMs using four direction and distance equal to 1,3,5. The authors tested the best first forward and backward search of the wrappers selection methods by applying the KNN and Naive Bayesian classifiers. For the evaluation the authors used MIAS and the private dataset named KBD-FER digital mammography database obtained from the University Hospital Dubrava, Zagreb, Croatia. The best results obtained using MIAS dataset was given by the best first backward selection method with Naive Bayesian classifier. In other side, the best results obtained using KBD-FER dataset was given by best first forward selection method and KNN classifier.

Masmoudi et al. [168] proposed local binary pattern variance descriptor (LBPV) to classify tissue density. LBPV allows to exploit the local and global textural information by using an adaptive weight to adjust the LBP descriptor histogram. The obtained descriptors are classified using ANN. For the evaluation the authors used the Tunisian dataset named EL FARABI from the radiology center EL FARABI Sfax Tunisia.

Kriti et al. [169] proposed a method based on the potential of Laws' masks of various lengths for texture description of mammographic images. After the manual extraction of ROIs of size 200×200 pixels, the authors computed five statistical parameters: mean, standard deviation, skewness, kurtosis, and entropy from Laws' texture energy images. The Laws' texture energy images are extracted from 2D Laws' masks constructed from one dimensional vectors for three different length of 5,7,9 pixels. The vectors describing the following features: Level(L), Edge(E), Spot(S), Wave(W) and Ripple(R). The authors used PCA to reduce the descriptors dimensionality, SVM and Probabilistic neural network (PNN) for the classification. The highest accuracy was obtained using the four principal components derived from Laws' masks of length 5 with SVM.

Virmani and kriti [170] proposed the use of wavelet energy descriptors for breast tissue density classification. First, the ROIs of size 200×200 pixels are manually extracted, then the following wavelets filters are applied on these ROIs: Haar (db1), Daubechies (db4 and db6), Coiflets (coif1 and coif2), Symlets (sym3 and sym5) and Biorthogonal (bior3.1, bior3.3 and bior4.4). Thereafter the energy descriptors are extracted from each sub-image results from the different decompositions. Finally, for the classification the authors tested SVM, KNN and PNN. The best results was obtained using the energy descriptors computed from the sub-image resulting from 2nd level decomposition of Haar wavelet filter classified with KNN.

Ahn et al. [171] developed a CNN for breast density estimation. The CNN was trained to learn the local and global image features. In fact, to extract the local features the authors applied the histogram stretching on down-sampling images. Then they generated four images, the first one represent a denoising image and the two other images represent hessian based eigenvalue 1 and 2 respectively and the last one is the original image with histogram-stretched. Thereafter a set of paths of size (41×41) were extracted from the above images and their histogram of 100 bins were computed. For the global features, the authors extracted a histogram of 100 bins from the whole histogram stretched image. Thus, they obtained a matrix features of 100×5 that was feed into the CNN. The proposed CNN was composed of 2 times convolutional layer +pooling+dropout and convolutional layer+pooling followed by 2 fully connected layers. The obtained correlation coefficient with the radiologist was equal to 0.96.

Xu et al. [172] proposed a CNN based on residual blocs to classify breast parenchymal into four and two BI-RADS categories. The CNN was composed of 67 convolution layers and 3 fully connected layers, all the convolutional layers have a kernel size of 3×3 and they

were decomposed on three groups. The first group have the number of filters equal to 64, in the second the number of filters was 128 and the last group have a number of filter equal to 256. The authors used 7 residual blocks in each group. The CNN was trained from scratch using INbreast dataset, after the application of the augmentation methods (rotation and flip) on images resized to 224×224.

Mohamed et al. [173] presented a CNN model based on AlexNet architecture to classify breast tissue into scattered density and heterogeneously dense. The CNN was composed of five convolutional layers, three max-pooling layers and three fully connected layers. The authors investigate two training approaches, in the first one the CNN was trained from scratch, in the second they applied the fine-tuning by using the weights of the pre-trained AlexNet learned on ImageNet. In the first training the CNN was trained on a private dataset of 22000 images and in the second training the authors used only 500 mammogram images. The results showed that the first training method outperform the second with a small difference.

Wu et al. [174] proposed a multi-column CNN to predict breast density. Each column has as input a crop image of size 2600×2000 from one of the four views used in screening mammography. The columns contain a set of convolutional and pooling layers (convolution+max pooling, convolution+convolution+max pooling, 2×(convolution+max), convolution, global average pooling).
The outputs of those columns (256×4) were concatenated and fed to the fully connected layer then to the softmax layer for density classification.

2.4 Breast histopathological image classification

The histology is a branch of biology dealing with the study of tissues[1], and the histopathology is a subsection of histology that aim to study tissue disease. The mammography help the radiologists to identify areas of abnormality, but in some cases, they can't differentiate cancerous from noncancerous cells [175] .
The histopathology still the primary test to accurate the cancer diagnosis, where a thin slice of suspected area tissue (section) is removed from body by surgical biopsy, then the staining is applied to enhance the visualization of the section, after that, the section is covered in a glass cover slip to be analyses by pathologists using microscope. The used of digital imaging techniques allows to digitalize the section into whole-slide digital pathology images (WSIs). Since these images are very large, the pathologists used smaller regions named patches extracted from WSIs to be analyzed with various magnifications. The pathologists accurate the cancer diagnosis and determine it level based on the cells shapes regularities and tissue distributions.

Breast cancer histopathological image analysis is a laborious and hard task, where the pathologist uses manual techniques to get quantitative information from images such as mitotic counts. This techniques are time-consuming that can lead to statistical human errors related to the decrease of attention due to fatigue [176]. In addition, to make the histopathological report the pathologists need to have a good experience in the field by studying a large numbers of tumors tissues.
To overcome this issue, several pathologist are integrated to produce the histopathological report. However, in some case might exist a disagreement between pathologists [177]. According to Allison et al. [178] this disagreement can be due to the difference in diagnostic study methodology and the different opinion features on diagnostic. These problems adversely affect the quality of the breast cancer diagnostic.

The CAD systems are developed to help the pathologists during the diagnosis, that allows to produce an efficient diagnostic by avoid misdiagnosis with reducing, both, the workload of pathologist and the cost. The developed methods in CAD system for Breast cancer histopathological image analysis are divided on two axes: The first axe is based on the extraction of the quantitative information from images by using segmentation techniques. The second one is based on texture representation.
The researches on both axes have been using hand-crafted features with machine learning and deep learning methods. In fact, the nuclei segmentation [179] [180] [181] [182] [183] and detection [184] [185] are the methods proposed to extract nuclei information, some others works focused on mitosis detection [186] [187] [188] and counting [186]. These methods provide a quantitative information that represent one of the salient factor used by pathologists to give a diagnostic.

[1] https://www.dictionary.com/browse/histology

In other hand, texture representation methods include tissue organization and tumor detection, these methods were developed by using both hand-crafted features with machine learning [189] [190] and deep learning method [191]. In addition, histopathological tissue is used to classify tumor type (benign and malignant) [192] [10] and cancer grade [193].

In this study we had chosen the histopathological tissue to classify the tumor type, the main reason is the availability of the datasets. The next section we will present the works related to the histopathological tissue studies to classify the tumor type, in the second part, we will highlight on the top performing methods in the ICIAR 2018 Grand Challenge on **B**re**A**st **C**ancer **H**istology image (BACH).

2.4.1 Related works

In the histological image classification we distingue two approaches of classification. The first one, used the whole slide images (WSIs) [194] and the second is based on region of interest.

As the used datasets in our study Breakhis and BACH datasets contain the region of interest from the WSIs, in this section we focus on introducing the works that used these datasets. Table 2.3 presents a summary methods that have used BreaKhis dataset, each methods is detailed next.

Spanhol et al. [5] tested a set of textural descriptors such as Local Binary Patterns (LBP) [213], Completed LBP (CLBP) [214], Local Phase Quantization (LPQ) [215], Gray-Level Co-occurrence Matrix (GLCM) [216], Parameter-Free Threshold Adjacency Statistics (PFTAS) [217] and ORB keypoint descriptor [218]. For the classification they tested the 1-nearest neighbor (1-NN), Quadratic Linear Analysis (QDA), SVMs and Random Forests (RF). The result obtained showed that PFTAS classified with SVM and QDA gave a good discriminative features for breast histopathological image classification .

Spanhol et al. [195] proposed CNN based on AlexNet architecture to classify breast cancer histopathological images. The CNN was composed of 5 layers containing respectively convolution + max pooling operation, convolution + average pooling, convolution + average pooling and finally 2 fully connected layer. First, the images were resized from 700×460 to 350×230 , then two methods were applied to extract the patches from the images: sliding window with 50 % of overlapping and random extraction with none overlap, by using patch image of size 32×32 and 64×64, in total 4 strategies were tested (1: sliding window + 32×32, 2: sliding window + 64×64, 3: random + 32×32, 4: random + 64×64). The conducted results on Breakhis dataset showed that the strategy #4 gave a good accuracy for low magnifications 40×, 100×. The authors also tested the combination of four CNNs using different strategies then they applied the max rule. The accuracy was improved only at the patient level.

Years	Author(s)	Methods	Protocol (train,test)	Total Accuracy (%)
2016	Spanhol et al. [5]	PFTAS+QDA	70%,30%	83.02
2016	Spanhol et al. [195]	Proposed CNN	70%,30%	84.46
2016	Spanhol et al. [195]	Combining multiclassifier	70%,30%	85.19
2016	Bayramoglu et al. [196]	CNN using multimagnification	70%,30%	83.24
2017	Spanhol et al. [192]	Deep features	70%,30%	83.93
2017	Sun and Binder [197]	GoogleLeNet	Not specified	86.81
2017	Song et al. [198]	Fisher Vector + VGG-VD model	70%,30%	86.67
2017	Han et al. [199]	CSDCNN	70%,30%	96.16
2017	Samah et al. [175]	Pyramid-structure Wavelet	70%,30%	85.62
2017	Nejad et al. [200]	Proosed CNN	70%,30%	77.5
2017	Sharma et al. [201]	PFTAS+ RF	Not spiecified	81.27
2017	Zhi et al. [202]	Proposed CNN	80%,20%	88.97
2018	Cascianelli et al. [203]	VGG+Reduction strategies	75%,25%	81.27
2018	Nejad et al. [204]	VGG+SVM	98%,2%	80
2018	Benhammou et al. [205]	Inception-V3	70%,30%	83.9
2018	Song et al. [206]	Fisher Vector + VGG19+ Component Selective Encoding (CSE)	70%,30%	88.03
2018	Sanchez-Morillo et al. [207]	KAZE Features	70%,30%	79.27
2018	Kumar and Rao [208]	Proosed CNN	70%,30%	82.93
2018	Alirezazadeh et al. [209]	Adapation+PFTAS+ QDA	70%,30%	87.85
2018	Al Nahid et al. [210]	CNN+Mean shift	Not specified	89
2019	Sudharshan et al. [211]	MIL+CNN	70%,30%	86.02
2019	Zhu et al. [212]	Hybrid CNN	70%,30%	83.37

Table 2.3: A summary studies of different works on histopathological images classification

Bayramoglu et al. [196] proposed a framework to classify breast cancer histology independent of their magnification. This framework contain two CNNs, one is single task used to classify the image as begin and malignant, and the second is multi task used to predict both malignancy and image magnification level. The authors justify the use of all magnification to train a CNN to reduce the training time. Actually, this approach is faster because single training is applied instead of different training for different magnifications. In the CNN multi task, the authors predict the magnification level of image to overcome the limitation of unknown image magnification at the test phase. In the preprocessing, the authors extract a patches of size 460×460, then they resize it to 100×100, thereafter they applied rotation and flipping to augment the dataset. The two proposed CNNs are very similar, in which both of then contain three convolution layers of size (7×7, 5×5, and 3×3), the first two convolution layer are followed by ReLu, max pooling and normalization layer the last convolution layer is followed by ReLu and max pooling, the architectures ended by two fully-connected layers. In the CNN single task only one softmax is use, in the CNN multi task two softmax are used (one for malignancy and the second for magnification prediction).

Spanhol et al. [192] used DeCAF features to classify histopathological images. In fact, the idea of DeCAF features is to reuse a pre-trained CNN (architecture and parameters). The input image is feed-forward into the pre-trained CNN and the result of the last layer was used as input to the classifier. The authors used the CNN CaffeNet trained on ImageNet and they used logistic regression as classifier. Where the combination of the last three fully connected layers (fc6,fc7,fc8) of CaffeNet were used as input to the classifier.

A similar work of [192], Benhammou et al. [205] applied DeCAF features on pretrained Inception-v3, while during the training, they pass the Decaf features outputs through a fully connected to the softmax classifier.

Sun and Binder [197] made several experiments for histopathology images classification, where they used three different CNNs namely Caffenet, Resnet and GoogLeNet. The first experiment concern the kind of transfer learning, in which the authors tested the training of whole network against training only the top network. The results showed that training the whole network is better. In the second experiment they tested the impact of context by testing the full image with resolution 350×230 and crop with size 64 and 128; the best result was obtained by using the whole image. The accuracies given by the three CNN were very close.

Song et al. [198] proposed a method based on CNN and fisher vectors for histopathology image classification. First the image forward to the convolution layers of VGG pretrained on imageNet, then the image features extracted from these layers are coded using Fisher Vector (FV). The authors proposed an Adaptation layer, this layer aim to adapt FV descriptors into the CNN; the adaptation layer was inserted between the convolution layers and the fully connected layers. Finally, the obtained descriptors was classified using Support Vector Machine (SVM).

Han et al. [199] proposed Class Structure-based Deep Convolutional Neural Network (CSDCNN) for breast histopathological image classification. The CSDCNN is a model that is designed to take into account the relation of the feature space among intra-class and inter-class. In fact, the authors integrate to the loss function a distance constraint to control the features similarities of intra-class and inter-class images. CSDCNN was inspired form GoogLeNet, the input layer was used to resize the image to 256×256, followed by a set of convolutional and pooling layers. The augmentation techniques (rotation, flipping and translation) were used to boost the performance and to resolve the imbalanced class problem. The authors adopted the transfer learning to train CSDCNN.

Samah et al. [175] tested a set of textural descriptors to classify histological tissue images. The features descriptors are GLCM, LBP, Pyramid-structured Wavelet Transforms (PWT) and Tree structured Wavelet Transform (TWT). The kNN was used as classifier. By using only the magnifying 400× the best result was given by PWT.

Nejad et al. [200] proposed a CNN to classify the histopathological image at the 40× magnifying factor. First the image was resized to half and the RGB color normalization is applied by subtracting the mean from all images of the dataset, the authors also applied the augmentation techniques using rotation and flipping. The CNN was composed of one hidden layer including a convolutional filters, one rectified linear unit for neuron activation, a normalization unit, a maximum pooling, followed by a fully connected layer.

Sharma et al. [201] have used the hand-crafted features with machine learning approach to diagnose breast cancer from histopathological images. Where they applied the region growing to segment the nuclei from the background, after that, they used the Parameter Free Threshold Adjacency Statistics (PFTAS) to extract the features of nuclei region, then Random forest classifier was used to predict the cancer cases.

Zhi et al. [202] presented a simple architecture CNN to predict malignant cases, this architecture was inspired from the six bottom layers of VGG, where it composed of three time (convolution (3×3), convolution (3×3) and maxpooling) followed by fully connected layer, dropout, fully connected layer and sigmoid. The architecture was initialized by the training weight of ImageNet, then the authors applied the transfer learning with two steps: firstly, they trained the fully connected layers while fixing the convolutional layers, secondly they fine tuning all the layers. According to the results given, applying transfer learning on a smaller architecture outperform the application of transfer learning on VGG model.

Another simple architecture proposed by Kumar and Rao [208] was composed of six convolutional layers, the first three layers have a kernels size of 5×5, that are followed by max pooling layers and the last three layers have a kernels size of 3×3 followed by average pooling layer, the architecture contain two fully connected layers.

Cascianelli et al. [203] used three dimensionality reduction methods on features extracted from a pre-trained VGG to classify histopathological images. The methods tested were Principal Component Analysis (PCA) [219], Gaussian Random Projection (GPR) [220]

and Correlation-Based Feature Selection (CBFS) [221]. The obtained results showed that GRP and CBFS were adequate for this type of classification.

Nejad et al. [204] proposed a content-based medical image retrieval (CBMIR) method based on CNN. The method was composed on two steps. In the first step, the images were resized into 224×224 and feed-forward into a pre-trained VGG, then 1000 features are extracted from the fully connected layer. The second step aim to reduce the dimensionality of the features vector by extracting class-specific and patient specific descriptors. The authors used the ensemble of Error Correcting Output Code (ECOC) [222] to train both multi-patient and breast cancer classifiers. In the test time, the Euclidien distance was used to retrieve the similar images to the image query based on the class-specific and patient-specific descriptors.

Song et al. [206] proposed an improved version of their method [198] by introducing a new method for features dimensionality reduction called the Component Selective Encoding (CSE). This method was used to reduce the high dimensionality of FV descriptors by selecting the discriminate Gaussian components in the FV. The authors used a combination of two quantification metrics to quantify the discriminativeness of each Gaussian component. The first one used the classification probabilities obtained from SVM classifiers trained on the N Gaussian components in the FV. The second metric is based on the discriminate weight obtained from the absolute difference between the benign and malignant weights for each components. The benign /malignant weights are obtained by training set of benign /malignant images, for each Gaussian component.

Sanchez-Morillo et al. [207] proposed a method based on KAZE [223] features and bag-of- words to classify benign and malignant histopathology image. In training step, for each image the KAZE keypoints were extracted, then k-means was applied to build the features bag, in order to quantize the features space of the training data, each cluster centre of the features bag was considered as a vocabulary word in a dictionary of visual words. The bag of visual words was used to encode the input image by using the nearest neighbor algorithm between the image KAZE features and the bag of visual words to encode the image into an histogram. This histogram was fed into SVM classifier for training. In the test step, the bag of words was used to encode the test image, and the SVM classifier is used to predict the image label. This method showed a good performance in magnification 40×.

Alirezazadeh et al. [209] proposed an adaptation method to overcome the mismatch of histopathological images caused by post processing such as staining. The authors project the test and training set into a domain invariant space. In fact, they extract the hand-craft features (PFTAS) forming with them a learning projection matrix. This matrix represent the correlation similarity of benignant and malignant cases, the authors minimize it by using gradient decent. Thereafter the samples are mapped through the projection matrix then to the classifier QDA.

Al Nahid et al. [210] tested CNN, Long Short Term Memory (LSTM) and combined CNN and LSTM to classify the breast cancer images. The authors tested also Softmax layer

and SVM as classifier. First, the K-means and mean-Shift clustering techniques were applied to the input image in order to partition the image into region with structural information, then the image result was feed to each model separately. The CNN model was composed of two convolution layers followed by three time convolution and pooling layers finished by flatten layer and drop-out then decision layer. The LSTM model contain two LSTM layers, followed by drop-out and dense layer finally the decision layer. The third model contain both CNN and LSTM, where the flatten layer of the CNN is followed by dense layer, the output of dense layer has been used as the input layer for LSTM. The result showed that the mean-Shift algorithm with the first model based on CNN and Softmax as classifier outperform the two others models.

Sudharshan et al. [211] explored the impact of Multiple Instance Learning (MIL) to predict breast cancer on histopathological images. From the twelve different MIL methods , the best result was given by non-parametric MIL [224] for two formulation. Where, the first one they used patient as bag and the images as instances, in the second one, they used image as bag and patches as instances. The authors also compare MIL to the single instance classifiers (1-NN, quadratic discriminant analysis, random forest and SVM) trained on the PFTAS features vector. The result showed the efficacy of the non-parametric MIL compared to single instance classifiers.

Zhu et al. [212] developed a hybrid CNN composed of global and local branch model. The two branch have the same model, the difference is only on the input. Where the global model have as input a down-sampled whole image, and the local model received as input a set of patches extracted from the image (the authors used 15 non overlapping patches). In order to reduce the complexity of the CNN, a pruning block was introduced to remove the redundant channels. Finally, to improve the performance, the bagging approach are used by assembling multiple models together.

In the rest of this section, we will present the top performing methods of the BACH challenge 2018 (see Table 2.4), for further details about the rest of the methods, we refer the reader to read the overview paper of the challenge [10].

Authors	Methods	Accuracy (%)
Chennamsetty et al. [225]	Resnet-101; Densenet-161	87
Kwok [226]	Inception-Resnet-v2	87
Brancati et al. [227]	Resnet-34, 50, 101	86
Marami et al. [228]	Inception-v3	84
Kohl et al. [229]	Densenet-161	83
Wang et al. [230]	VGG16	83
Steinfeldt et al.	XCeption	81
Koné and Boulmane [231]	ResNeXt50	81

Table 2.4: Overview of the top performed methods on BACH challenge

The method proposed by Chennamsetty et al. [225] is base on three CNNs, ResNet-101 and two DenseNet-161 networks pre-trained on ImageNet. The authors adopted two approaches of normalizations, normalization scheme−1 and normalization scheme−2. In the first one, the normalization is given by using the mean and standard deviation from ImageNet dataset, while in the normalization scheme−2, they used the mean and standard deviation from histology data.

In the pre-processing the images are resized to 224×224 pixels, then normalization scheme−1 is applied, next the images passed through ResNet-101 and DenseNet-161 separately; on the other side, the images normalized with schema−2 are passed through the second DenseNet-161. Finally the majority voting was used on the three predictions to assign the final label to the image. With an accuracy of 87% this method won the challenge with Kwok's method [226].

Kwok used Inception-Resnet-v2 initialized using ImageNet pre-trained weights to classify H&E stained images [226].

Firstly, the patches of size 1495×1495 pixels and stride of 99 pixels were cropped from each image. In total 5,600 patches where extracted from 400 microscopy images. These patches were then resized to 299×299 pixels. For the augmentation the authors applied the rotational symmetry, random vertical/ horizontal flipping and rotation of 90°, 180°, 270°. Then the patches passed through Inception-Resnet-v2 for classification.

Brancati et al. [227] used combination of three ResNet with different configurations of layers, where 34, 50 and 101 layers are used respectively. First, the authors reduce the size of the image by down-sampling the image by factor k equal to 80%, in which patch image of size 308×308 pixels was extracted from the image center. Then the CNNs were pre-trained on ImageNet and all the layers are fine-tuning by the patches extracted from BACH training dataset. Next the maximum probability rule is used to assign the image label. This approach ranked in the top-three method in the challenge.

Marami et al. [228] constructed an ensemble of four Inception-v3 trained using four different datasets.
The first one, is BACH training dataset part ”A” contain four classes (in-situ carcinoma, invasive tumor, and benign tumor).
The second one, BACH training dataset part ”A” and the training dataset of the part ”B” of the challenge that contain whole slide images with three classes (benign, invasive, and in-situ).
The third one, BACH training dataset part ”A” and whole slide images with expanded annotation for normal tissue (benign, invasive, in-situ and normal).
The fourth one , BACH training dataset part ”A” and whole slide images with expanded annotation for normal tissue, and BreakHis images for the benign tissue class.
The ensemble network models are trained on annotated regions of size 512×512 pixels. The authors modify the inception network by using adaptive pooling before applying the fully connected layers. The class predictions of test images are inferred by averaging the probabilities of the trained CNNs.

Kohl et al. [229] propose to used densely connected convolutional neural networks (DenseNet -161) pre-trained on ImageNet to classify the histopathological images.
In the pre-processing, the images are resized to 205×154 pixels, then data augmentation is applied to overcome the issue of the small number of training images by using arbitrary rotations and random scale. Finally the authors normalized each image by the mean and the standard deviation of all images in the dataset. The training phase was composed of two step: first, the training was applied only on the fully connected layer, in the second step the training was applied to the whole layers.

Wang et al. [230] proposed an approach based on two training stage. In the first stage the training images were resized to 256×256 and normalized to zero mean and unit standard deviation, then the authors augment the training dataset by using random cropping of size 224×224, rotation 90°,181°,270° and random horizontal inversion, and random vertical rotation. After that, they applied the Sample Pairing method for another data augmentation, Sample Pairing method consist to randomly selected two images from different classes, and then they were superimposed together to generate a new image, the image result receives the class label of one of the initial images. Sample Pairing method was applied on the augmented data and the obtained images were passed though VGG-16 network for training. In the second stage, the network weight obtained from the first stage were used to initialize another VGG-16 and in this training stage only the basic data augmentation techniques (random cropping, random 90°,181°,270° rotation, random horizontal inversion, and random vertical rotation) were applied.

Koné et. al [231] used hierarchical binary tree classification approach, in which they used three ResNeXt50. In the root of CNN classifies there is general model aim to classify the image into carcinoma and non-carcinoma. Carcinoma set contains the in situ and the invasive

images, and non-carcinoma set contains normal and benign images. The general model is pre-trained on ImageNet and Fine tuning with patches of size 299×299 extracted from the center of the resized images. Followed by two specialized models, one of them classify the carcinoma set into in situ and invasive and the other one classify the non-carcinoma set into normal and benign. These models were initialized by the weight obtained from the general model. The CNNs used were trained with different learning rates, this method with our proposed method, were ranked 7th out of 51 teams of the challenge.

2.5 Conclusion

This chapter highlighted annotation and classification methods for liver CT, breast density and histopathological images.

In fact, we reviewed in details more than sixty works including the methods proposed for different challenges. In both annotation and classification tasks, ROIs extraction, the features extraction methods and machine learning approaches are used to achieve them. The trend to use the deep learning approaches to analyze the medical image is noteworthy, especially in related methods for histopathological images classification. As we have presented in section 2.4, the majority literature methods used the CNNs, this is due to the capacity of CNNs to discriminate relevant image information from these complex images. The three followed chapters, we will detail the methods used for annotation and classification of liver CT, breast density and histopathological images.

Chapter 3

Liver CT annotation

3.1 Introduction

According to the statistic given by World Health Organization (WHO), liver cancer is one of the fourth most common causes of cancer death after lung, colorectal and stomach [232]. With more than 700 000 deaths each year [233], liver cancer is the fifth most common cause of cancer death for men and the seventh for women [234].
Early diagnostics and treatments can improve the chances of survival. Indeed, the percent of people that live at least 5 years after the liver cancer was improved since 40 years ago, from 3% to 18% now [234]; this despite that, the rate of liver cancer death has tripled from this period [233].
More and more solutions have been increasingly developed and implemented to improve the early diagnosis and treatment, such as the different imaging techniques resulted the prominence of computer-aided detection and diagnosis CADe/CADx systems .
The CAD system help the radiologists in their daily works by providing liver lesions annotation based on image processing and artificial intelligence techniques.

In this chapter, we presented the methods used to annotate the liver lesions, in order to generate a structured radiologic report. The next section, we will present the methods proposed for liver CT image annotation. Thereafter, we will give the experimental results obtained on ImageCLEF2015 liver CT annotation challenge and the comparative study with related works is given in section 3.3.

3.2 Methods

Medical image annotation is the process allowing to assign textural and graphical metadata to the image. In fact, the graphical metadata is manifested by specifying the contour and the regions of organ. In other side, the textural metadata vary from simple information such as image modality and body orientation to more complicate metadata named height level semantic concepts. These concepts are used to describe the proprieties of organ its components and lesions.

In the past years, the radiologist annotated the medical images manually. This process requires time and expertise because it is subjective, and in addition it is expensive [132]. The clinicians got one's way to overcome these issues, by using the support of automatic medical images annotation. Actually, the automatic medical images annotation is an important tool for making an organized semantic archives; that will be used by physicians in their diagnostic as well as their education. Generally, in liver images the annotation include liver features, vessels and lesions.

In this section we will present the methods developed for automatic liver annotation, more precisely the liver CT images, we have chosen this modality because liver lesions and metastases are most often initially indentified and diagnosed in CT images [126] .

The proposed annotation methods are based on Content-Based Image Retrieval (CBIR) and classification approaches.

The CBIR, rely the low level image features to the height level semantic concepts by retrieving the image that have the same low level image features to the image query, then the selection of adequate annotations for a given concept of image test are obtained from the results.

In the classification approaches, each concept's label is considered as a class that we want to predict, so the machine learning methods are used to predict the appropriate annotation according to the low level image features.

The community scientific has been invested on developing a standardized vocabularies in order to facilitate the annotation and the sharing. Such as the lexicon RadLex for radiology terms [235] and ONLIRA (Ontology of the Liver for Radiology) [124].

ONLIRA ontology contains various liver concepts as well as their relationships that help to generate an express radiology reports [124]. In all the presented methods, we have used the concepts and proprieties of ONLIRA ontology to annotate the liver CT image.

In Table 3.1 we will describe the concepts to annotate as well their properties.

Group	Concept	Properties (UsE features)	Possible values (assigned indices)
Liver	Liver	Liver Placement	downward displacement(0), normal placement(1), leftward displacement(2), upward displacement(3), other(4)
		Liver Contour	irregular(0), lobulated(1), nodular(2), regular(3), other(4)
		Liver Size Change	decreased(0), increased(1), normal(2), other(3)
		Liver Craniocaudal Dimension (mm)	The amount change in size of liver(mm)
		Density Type	heterogeneous(0), homogeneous(1), other(2)
		Density Change	decreased(0), increased(1), normal(2), other(3)
	Right Lobe	Right Lobe Craniocaudal Dimension (mm)	The amount change in size of right lobe(mm)
		Right Lobe Size Change	decreased(0), increased(1), normal(2), other(3)
	Left Lobe	Left Lobe Craniocaudal Dimension(mm)	The amount change in size of left lobe(mm)
		Left Lobe Size Change	decreased(0), increased(1), normal(2), other(3)
	Caudate Lobe	Caudate Lobe Craniocaudal Dimension(mm)	The amount change in size of caudate lobe(mm)
		Caudate Lobe Size Change	decreased(0), increased(1), normal(2), other(3)
Vessel	Hepatic Artery	Hepatic Artery Lumen Diameter	decreased(0), increased(1), normal(2), other(3)
		Hepatic Artery Lumen Type	obliterated(0), open(1), partially obliterated(2), other(3)
	Hepatic Portal Vein	Hepatic Portal V. Lumen Diam.	decreased(0), increased(1), normal(2), other(3)
		Hepatic Portal V. Lumen Type	obliterated(0), open(1), partially obliterated(2), other(3)

		is Cavernous Transformation Observed? (Hepatic Portal Vein)	NA(-1),True(1),False(0)
	Left Portal Vein	Left Portal V. Lumen Diam	decreased(0), increased(1), normal(2), other(3)
		Left Portal V. Lumen Type	obliterated(0), open(1), partially obliterated(2), other(3)
		is Cavernous Transformation Observed? (Left Portal Vein)	NA(-1),True(1),False(0)
	Right Portal Vein	Right Portal V. Lumen Diam	decreased(0), increased(1), normal(2), other(3)
		Right Portal V. Lumen Type	obliterated(0), open(1), partially obliterated(2), other(3)
		is Cavernous Transformation Observed? (Right Portal Vein)	NA(-1),True(1),False(0)
	Hepatic Vein	Hepatic V. Lumen Diam	decreased(0), increased(1), normal(2), other(3)
		Hepatic V. Lumen Type	obliterated(0), open(1), partially obliterated(2), other(3)
	Left Hepatic Vein	Left Hepatic V. Lumen Diam	decreased(0), increased(1), normal(2), other(3)
		Left Hepatic V. Lumen Type	obliterated(0), open(1), partially obliterated(2), other(3)
	Middle Hepatic Vein	Middle Hepatic V.Lumen Diam.	decreased(0), increased(1), normal(2), other(3)
		Middle Hepatic V.Lumen Type	obliterated(0), open(1), partially obliterated(2), other(3)
	Right Hepatic Vein	Right Hepatic V. Lumen Diam	decreased(0), increased(1), normal(2), other(3)
		Right Hepatic V. Lumen Type	obliterated(0), open(1), partially obliterated(2), other(3)
General	Patient	Diagnosis	Diagnosis of given image using ICD10 codes (bar separated) and in the free text MD's comments are written (bar separated)

Lesion	Lesion	Cluster Size	1(1), 2(2), 3(3), 4(4), 5(5), multiple(6) For simple cases this value shows number of lesions inside the ROI, but in case of having more than one lesions of a certain type, the biggest lesion is annotated as a sample of that cluster and number of lesions with same properties is written here
		Contrast Uptake	NA(-1), dense(0), heterogeneous(1), homogeneous(2), minimal(3), moderate(4), other(5)
		Contrast Pattern	NA(-1), central(0), early uptake then wash out(1), fixing contrast in late phase(2), heterogeneous(3), homogeneous(4), peripheric(5), peripheric nodular(6), spokes wheel(7), undecided(8), other(9)
		Lesion Composition	SolidCycsticMix(0), Solid(1), SolidWithCystic(2), PureSolid(3), PredominantSolid(4), Cystic(5), PureCystic(6), PredominantCystic(7), CysticWithSolidComponent(8), CysticWithDebris(9), Abcess(10)
		is Leveling Observed?	True(1),False(0)
		Leveling Type	NA(-1), fluid fluid(0), fluid gas(1), fluid solid(2), gas solid(3), other(4)
		is Debris observed?	True(1),False(0),NA(-1)
		Debris Location	NA(-1), floating inside(0), located on dependent position(1),other(2)
		is Close to Vein	NA(-1), HepaticArtery(0), HepaticPortalVein(1), RightPortalVein(2), LeftPortalVein(3), HepaticVein(4), RightHepaticVein(5), MiddleHepaticVein(6), LeftHepaticVein(7), VenacavaInferior(8), PosteriorBranchOfRightPortalVein (9), AnteriorBranchOfRightPortalVein (10), other(11)

		Vasculature Proximity	NA(-1), adjacent(0), adjunct to contact(1), bended(2), circumscribed(3), invaded(4), other(5)
	Area	Lobe	LeftLobe(0), CaudateLobe(1), RightLobe(2)
		Segment	SegmentI(1), SegmentII(2), SegmentIII(3), SegmentIV(4), SegmentV(5), SegmentVI(6), SegmentVII(7), SegmentVIII(8)
		Width	a number in mm which represents width of the lesion
		Height	a number in mm which represents heigth of the lesion
		is Gallbladder Adjacent?	True(1),False(0)
		is Peripherical Localized?	True(1),False(0)
		is Subcapsular Localized?	True(1),False(0)
		is Central Localized	True(1),False(0)
		Margin Type	geographical(0), ill defined(1), irregular(2), lobular(3), serpiginious(4), spiculative(5), well defined(6), other(7)
		Shape	band(0), fusiform(1), irregular(2), linear(3), nodular(4), ovoid(5), round(6), serpiginious(7), other(8)
		is Contrasted	True(1),False(0),NA(-1)
		is Calcified? (Area)	True(1),False(0),NA(-1)
		Area Calcification Type	NA(-1), coarse(0), focal(1), millimetric-fine(2), punctate(3), scattered(4), other(5)
		Density	NA(-1), hyperdense(0), hypodense(1), isodense(2), other(3)
		Density Type	NA(-1), heterogeneous(0), homogeneous(1), other(2)
	Capsule	is Calcified? (Capsule)	True(1),False(0),NA(-1)

		Capsule Calcification Type	NA(-1), coarse(0), focal(1), millimetric-fine(2), punctate(3), scattered(4), other(5)
	Polyp	is Calcified? (Polyp)	True(1),False(0),NA(-1)
		Polyp Calcification Type	NA(-1), coarse(0), focal(1), millimetric-fine(2), punctate(3), scattered(4), other(5)
	Pseudocapsule	is Calcified? (Pseudocapsule)	True(1),False(0),NA(-1)
		Pseudocapsule Calc.Type	NA(-1), coarse(0), focal(1), millimetric-fine(2), punctate(3), scattered(4), other(5)
	Septa	is Calcified? (Septa)	True(1),False(0),NA(-1)
		Septa Calcification Type	NA(-1), coarse(0), focal(1), millimetric-fine(2), punctate(3), scattered(4), other(5)
		Diameter Type	NA(-1), complete(0), incomplete(1), other(2)
		Thickness	NA(-1), thick(0), thin(1), other(2)
	Solid Component	is Calcified? (Solid Component)	True(1),False(0),NA(-1)
		Solid Component Calcification Type	NA(-1), coarse(0), focal(1), millimetric-fine(2), punctate(3), scattered(4), other(5)
	Wall	is Calcified? (Wall)	True(1),False(0),NA(-1)
		Wall Calcification Type	NA(-1), coarse(0), focal(1), millimetric-fine(2), punctate(3), scattered(4), other(5)
		Wall Type	NA(-1), thick(0), thin(1), other(2)
		is Contrasted?(Wall)	True(1),False(0),NA(-1)

Table 3.1: List of Groups, concepts, proprieties and their possible values

Remark

Other: none of the other labels answer the question.

NA: the question is not relevant to this image.

3.2.1 Method n° 1

Our first method for liver CT image annotation is based on a classification approach. Our method is composed of two main steps. The first step consists of features vectors extraction, where two descriptors containing a set of texture and shape features are extracted. In the second step, a classification process is achieved by using random forest classifier.

A. *Features extraction and description*

The descriptor n°1

•The proposed liver features includes

1. Liver Mean: liver's mean intensity value.
2. Liver Variance: liver's variance intensity value.
3. Liver Skewness: liver's skewness value.
4. Liver Kurtosis: liver's kurtosis value.
5. Liver Solidity: solidity of liver.
6. Liver Convexity: convexity of liver.
7. Gray Level Co-occurrence Matrix (GLCM): we have used the features extracted from the spatial GLCM proposed by Haralick that estimates image properties related to second-order statistic. We have calculated the 3D gray level co-occurrence matrix for four different directions (0°, 90°, 45°, and 135°) and distance d=1, the Haralick's texture features extracted are: contrast, entropy, variance, sum mean, correlation, max probability, inverse variance, inertia [216], and also energy, cluster shade, cluster prominence and homogeneity proposed by by Soh and Tsatsoulis [236]. Therefore, our GLCM based feature vector includes 48 elements.

7. 3D Gabor wavelet transform: we have used the mean and the standard deviation as texture features extracted form the images filtred by Gabor wavelet.

   In the following we will provide more details about Gabors wavelet.

   It is a transformation that captures the local structure corresponding to spatial frequency (scale), spatial localization, and orientation selectivity [237]; it is defined in the equation 3.1.

$$\Psi_{u,v}(z) = \frac{\|K_{u,v}\|^2}{\sigma^2} e^{\left(\frac{\|K_{u,v}\|^2 |z|^2}{2\sigma^2}\right)} \left[e^{ik_{u,v}z} - e^{-\frac{\sigma^2}{2}}\right] \tag{3.1}$$

   Where Z=(x,y), u and v define the orientation and the scale of the Gabor kernels, ||.|| denotes the norm operator, and the wave vector $K_{u,v}$ is defined as follows:

$$K_{u,v} = K_v e^{i\theta_\mu} \tag{3.2}$$

Where K_v=k_{max}/f_v , K_{max} is the maximum frequency and f is the spacing factor between kernels in the frequency domain, θ_u= πu / 8
We have used σ = 2π, K_{max} = π /2, and f = $2^{1/2}$.
Let I(x,y) be the gray level distribution of an image, the convolution of the image I and a Gabor kernel $\psi_{u,v}$ is defined as follows:

$$O_{u,v} = I(z) * \Psi_{u,v}(z) \tag{3.3}$$

Where * denotes the convolution operator, and $O_{u,v}$(z) is the convolution result corresponding to the Gabor kernel at orientation u and scale v.
The energy information of the image I (x, y) can be expressed as follows [238]:

$$E_{u,v} = \sum_x \sum_y |O_{u,v}| \tag{3.4}$$

Suppose that I(x,y) denotes an image of M × N pixels, $\mu_{u,v}$(x) and $\sigma_{u,v}$(x) denote its mean and standard deviation computed from the scale v and the direction u, respectively, $\mu_{u,v}$(x) and $\sigma_{u,v}$(x) can be computed as follows :

$$\mu_{u,v} = E_{u,v}/MN \tag{3.5}$$

$$\sigma_{u,v} = \sqrt{\frac{\sum_x \sum_y (|O_{u,v}(z)) - \mu_{u,v}|)^2}{MN}} \tag{3.6}$$

With eight orientations and three scales, the feature vector includes 24 elements for means and 24 elements for deviation. Therefore, the feature vector is composed of 48 features.

• The proposed lesion features

A pre-processing step was applied in order to segment the lesion. To do this, we have applied a morphological operation which is dilatation. This operation was done after thresholding the liver and applying the AND operator between lesion bounding box and the liver mask. Thereafter, we extracted the following features:

1. The Euclidean distance between the centroid of the liver and lesion centroid.
2. The distance between the x coordinate centroid of the liver and the x coordinate centroid of the lesion.
3. The distance between the y coordinate centroid of the liver and the y coordinate centroid of the lesion.
4. Surface area of the lesion.
5. The perimeter of the lesion.

6. The circularity C1 of the lesion: this measure always takes the value of 1 for perfect circles [239] , it is expressed by the following formula:

$$C1 = \sqrt{\frac{Area}{(\pi MaxRadius)^2}} \tag{3.7}$$

7. Dispersion property: the irregularity of the mass is estimated from dispersion property, which identifies the irregular shape characteristics [239]. This value is given by the equation below:

$$Dp = \frac{MaxRadius}{Area} \tag{3.8}$$

8. Elongation property: the regular oval mass can be differentiated from the irregular by using Elongation [239]. Its value is expressed by the following equation :

$$En = \frac{Area}{(2MaxRadius)^2} \tag{3.9}$$

9. The circularity C2 of lesion: this value show a mass is similar to an ellipse. It is useful in differentiating circular / oval masses from irregular masses. This measure always takes a value of 1 for perfect squares, circles [239]. It is calculated by the equation given below:

$$C2 = \sqrt{\frac{MinRadius}{MaxRadius}} \tag{3.10}$$

The total dimension of the first descriptor is 111(6+48+48+9).

The descriptor n°2

We have also investigated the performances of our method by using a second descriptor containing the texture features of the lesion instead of liver texture features. The two texture features are the gray level co-occurrence matrix (GLCM) for four different directions (0°, 90°, 45°, and 135°) and distance d=1. Therefore, our GLCM based features vector includes 48 elements. The second texture features is Gabor wavelet transforms, we have used the mean and the standard deviation, with sixteen orientations and five scales, the features vector includes 80 elements for means and 80 elements for deviation. Therefore, the total dimension of the second descriptor is 223 (6+48+160+9).

Now let's recap:

Descriptor 1: contain shape and texture features of liver with lesion shape features, the total size of the descriptor is 111 features.

Descriptor 2: contain liver shape features with shape and texture features of lesion, the total size of the descriptor is 223 features.

B. *Classification*

In the second phase of our experiments, we have used a supervised multi-class classifier based on Random Forest classifier (RF) [240] and a proposed similarity score calculation. RF is a machine learning technique that builds a forest of classification trees where each tree is grown on a bootstrap sample of data, and the attribute at each tree node is selected from a random subset of all attributes. The final classification of an individual is determined by voting over all trees in the forest. Indeed, there are many advantages of using RF method, that make it an ideal approach for the analysis of biological data. First, it can handle a large number of input attributes - both qualitative and quantitative-. Second, it estimates the relative importance of features in determining classification. Third, RF is fairly robust in the presence of etiological heterogeneity and relatively high amounts of missing data. For the tree type we have used Classification And Regression Tree (CART), and our RF is composed of 500 tree. To obtain the annotation of the liver's concepts, we associate for each concept a classifier. Indeed, the two descriptors extracted are feed forward separately to Random forest classifier in order to predict the correct annotations of the liver's concepts.

The following concept's proprieties are predicted using the classification approach: Is Central Localized, Is Contrasted, Is Gallbladder Adjacent, Is Peripherical Localized, Is Subcapsular Localized, Has Lesion Quantity, Has Area Density, Has Area Shape, Has Area Margin Type, Has Density, Has Lesion Contrast Uptake, Has Lesion Contrast Pattern, Has composition, Has Lesion Vein Proximity, Is Located In Segment, Is Close To Vein. The property "Is Located In Lobe" is estimated according to the property "Is Located In Segment". i.e. if segment is { II,III,IV } the lesion lobe is the left lobe, if the segment is { V,VI,VII,VIII } the lesion lobe is the right lobe, and caudate Lobe for segment I. The height and the width of lesion are extracted directly from the image.

One of the challenge of the used dataset was that some concepts have just a few sample, this was make the application of classifier ineffective. For this reason, to annotate the remaining concepts, we have used the proposed similarity score calculation between the unannotated image (U) and a training image (T) as the distance between their respective features vectors given as bellow:

$$Sim(U,T) = \sum_{i=1}^{d} 1 - \frac{|u_i - t_i|}{v_i} \tag{3.11}$$

Where v_i was the *i-th* maximum feature in dataset , u_i was the *i-th* feature in the features vector of U, t_i was the *i-th* feature in the features vector of T, and d was the dimensionality of the feature set. Thereafter, we selected the five most similar images, and the label that has the majority voting will be assigned to the concept's proprieties.

3.2.2 Method n° 2

Our second method is based on CBIR by using the signature of the liver. To do that, we have taken a slice from 3D Liver CT scans localized at lesion center. First, we normalized the liver into a rectangular block with constant dimensions to account for imaging inconsistencies. The size of the normalized block was (200×190).
Feature encoding was implemented by convolving the normalized liver pattern with 1D Log-Gabor wavelets. The 2D normalized pattern was broken up into a number of 1D signals, and then these 1D signals were convolved with 1D Gabor wavelets. The frequency response of a Log-Gabor filter is given as:

$$G(f) = exp(\frac{-(log(f/f_0))^2}{2(log(\sigma/f_0))^2}) \tag{3.12}$$

Where f_0 represents the centre frequency, and σ gives the bandwidth of the filter.
Thereafter we divided the output of filtering into a small blocks of size (5×5), consequently the size of template becomes (40×38) .
Finally, the dominant angular direction of each block was extracted and quantized to four levels, using the Daugman method [241], where each angular direction produced two bits of data. Indeed when going from one quadrant to another, only 1 bit changes. Figure 3.1 shows the phase quantization.

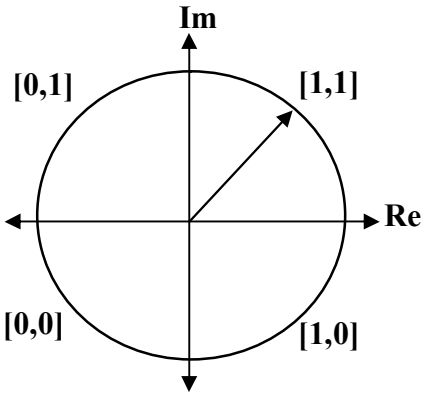

Figure 3.1: Phase Quantization

The encoding process produces a bitwise template containing a number of bits of information, the final size of template is 40×76.
For the retrieval task, the Hamming distance was employed. This distance gives a measure of how many bits are the same between two bit patterns. In comparing with the bit patterns X and Y, the Hamming distance, HD, is defined as the sum of disagreeing bits (sum of the

exclusive-OR between X and Y) over N, the total number of bits in the bit pattern.

$$HD = \frac{1}{N}\sum_{j=1}^{N} X_j(XOR)Y_j \tag{3.13}$$

Thereafter, we selected the five most similar images, and the label that has the majority voting will be assigned to the concept's proprieties. The retrieval process is illustrated in Figure 3.2.

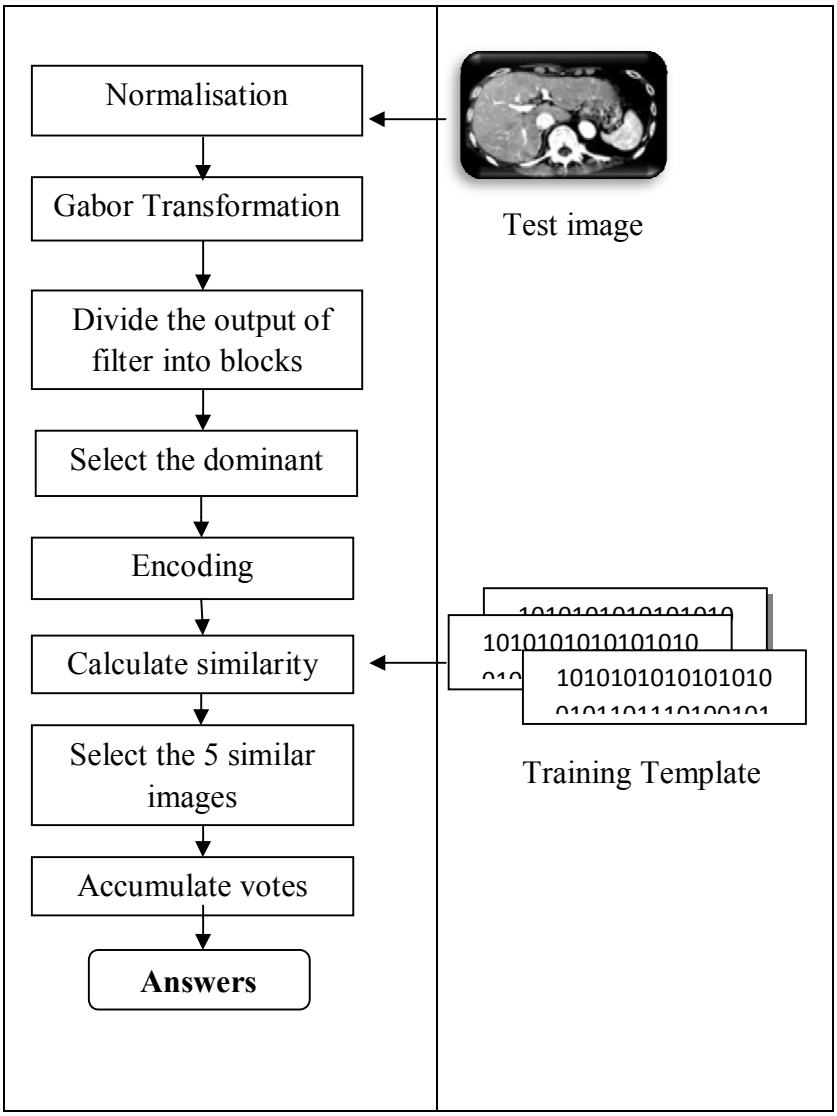

Figure 3.2: An overview of the retrieval process

3.2.3 Method n° 3

This method is based on CBIR using spectral images textural analysis that uses a combination of Bidimensional Empirical Mode Decomposition (BEMD) and Gabor wavelet transform.

A. *Features extraction and description*

First, for each input image we have applied the Bidimensional Empirical Mode Decomposition (BEMD), then we have transformed each Bidimensional Intrinsic Mode Function (BIMF) using the Gabor wavelet transform, thereafter the mean and the standard deviation are extracted.

Based on a similarity distance given in equation 3.11, we selected the five most similar images, and the label that has the majority voting will be assigned to the concept's proprieties.

More details about BEMD is given in the next paragraph.

- **Bidimensional Empirical Mode Decomposition (BEMD)**

  The Bidimensional Empirical Mode Decomposition (BEMD) approach is a highly adaptive decomposition [242]. It is mainly based on the characterization of image by Intrinsic Mode Function (IMF) decomposition, where the image can be decomposed into a redundant set of composite images called IMF and a residue. Adding all the IMFs with the residue allow reconstructing the original image without distortion or loss of information [243]. This method, derived from image data and which is fully unsupervised, permits to analyze nonlinear and non stationary data as texture images.

- **The extracted descriptors**

  In order to evaluate our approach, we calculated two descriptors:

  Descriptor n° 1: is computed by applying Gabor wavelet transform with sixteen orientations and ten scales, so we have extracted 160 elements of means and 160 elements of deviation from the first BIMF decomposition. Therefore, the total dimension of the first descriptor was 320.

  Descriptor n° 2: is calculated from the first, the second and the third BIMF, we have extracted 160 elements of means and 160 elements of deviation for each one of them. Therefore, the total dimension of the second descriptor was 960.

3.3 Experimental results

In this section, we will present the experimental results of the proposed methods for liver CT image annotation. To do an effective and objective evaluation of the methods, we have participated to the second version of ImageCLEF Liver CT Image Annotation challenge in 2015 by submitting the first and the second methods. We will explain in detail this challenge in the next paragraph.

3.3.1 ImageCLEF challenge

A. *Objective of the challenge*

The aim of the liver CT annotation task was to automatically generate a structured reports. Describing the semantic features of the liver, its vascularity, and lesions.
This reports can help to raise the difficult task of annotating the liver CT image [244].

B. *Dataset*

In our experimentations, we have used the ImageCLEF2015 liver CT annotation dataset.
The training dataset includes 50 cases, each consisting of :
• Cropped CT image of the liver, a 3D matrix. The volumes had varied resolutions (x: 190-308 pixels, y: 213-387 pixels, slices: 41-588) and spacing (x, y: 0.674-1.007mm, slice: 0.399-2.5mm),
• A liver mask that specifies the part corresponding to the liver,
•A bounding box (ROI) corresponding to the selected region of the lesion within the liver,
• An RDF file contained 73 ground truth annotations (**Us**er **E**xpress (UsE) features). These annotations were determined by clinician based on the ONLIRA lexicon terms.
The test dataset contained 10 CT volumes, with varied resolutions and pixel spacing, cropped to the region around the liver. The test data also included a mask of the liver pixels and a bounding box (ROI) (see Figure 3.3).

C. *Evaluation criteria*

The evaluation is performed on the basis of the completeness and accuracy of the predicted annotations. Completeness is defined as the number of predicted annotations divided by total number of annotations, while accuracy is the number of correct predicted annotations divided by total number of predicted annotations.

$$Completeness = \frac{Number\_of\_predicted\_UsE\_features}{Total\_number\_of\_UsE\_features} \tag{3.14}$$

$$Accuracy = \frac{Number\_of\_corrected\_predicted\_UsE\_features}{Number\_of\_predicted\_UsE\_features} \tag{3.15}$$

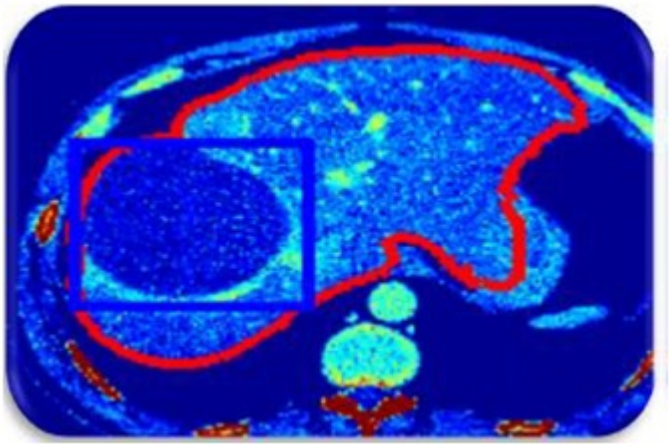

Figure 3.3: Image test of the liver, the contour in red and ROI in blue

Method	Runs	Completeness	Accuracy	Total Score
Method 1:Desriptor 1	01	0.99	0.825	0.904
Method 1:Descriptor 2	02	0.99	0.822	0.902
Method 2	03	0.99	0.836	0.910

Table 3.2: The runs results of Liver CT annotation task 2015 [6][7]

$$Total\_Score = \sqrt{Completeness \times Accuracy} \tag{3.16}$$

D. *The models submitted*

We have submitted three runs to ImageCLEF2015 liver CT annotation challenge, the two first runs correspond to the first method with the first and the second descriptor, and the third run correspond to the second method.

E. *Results*

Among 32 groups, which registered for the challenge, only our group have submitted the runs to the second version of ImageCLEF liver CT annotation challenge in 2015 [6].

The results in Table 3.2 show that all of our runs achieved good scores (>90). In general, there were no large difference between the scores, especially for the first method, where we have used two different descriptors. The score obtained from the first and the second descriptor are respectively 90.4% and 90.2%, this small difference shows that texture features of liver is more descriptive than the texture features of lesion. We achieved a completeness score of 99% for every run, and the best accuracy of 83.6% was given by the second method.

	Liver		Vessel		Lesion-Area		Lesion-Lesion		Lesion-Component	
Run	**Comple**	**Acc**	**Comple**	**Acc**	**Comple**	**Acc**	**Comple**	**Acc**	**Comple**	**Acc**
Run1	1.00	0.925	1.00	1.00	1.00	0.730	1.00	0.47	0.96	0.87
Run2	1.00	0.925	1.00	1.00	1.00	0.746	1.00	0.47	0.96	0.84
Run3	1.00	0.925	1.00	1.00	1.00	0.753	1.00	0.48	0.96	0.89

Table 3.3: Completeness (comple) and Accuracy (Acc) of the five different groups of liver concepts [6] [7]

	Descriptor n°1		Descriptor n°2	
	Completeness	**Accuracy**	**Completeness**	**Accuracy**
Liver	1.00	0.92	1.00	0.92
Vessel	1.00	1.00	1.00	1.00
Lesion-Area	1.00	0.65	1.00	0.67
Lesion-Lesion	1.00	0.48	1.00	0.51
Lesion-component	0.96	0.86	0.96	0.89
Total score	**0.880**		**0.889**	

Table 3.4: The score results obtained for each group of the method n°3 [8]

The results presented in Table 3.3 shows that the scores obtained by the three runs for liver group and vessel group are the same. One explanation for this could be that there were instances where in all the training samples had the same annotation. We notice that the second method outperform the first method in the other groups, which shows its efficacy.

For the first method, descriptor 1 (run1) gives the best discrimination of lesion component compared to the descriptor 2 (run2), in this case the texture features of liver is more suitable than texture features of lesion, in other hand the properties of area lesion were well described by the texture features of lesion.

After the challenge we have developed and evaluated the third method using the same dataset and we obtained the results given in Table 3.4.

The two descriptors achieved the same result with just a few small difference between them , where the best result is obtained by using three BIMFs with the score of 88.9% compared to the first descriptor with the score of 88%. This suggests that, using more details improves the annotation's accuracy.

3.3.2 Comparative study with related works

In this section, we make a comparison with related works that have used the same dataset, this give an objective comparison.

ImageCLEF liver CT annotation challenge was organized on two versions in 2014 and 2015. As we were the only ones group that participated to the 2015 version, we will compare our

Year	Methods	Liver		Vessel		Lesion-Area		Lesion-Lesion		Lesion-Component	
		Comp	**Acc**	**Comp**	**Acc**	**Comp**	**Acc**	**Comp**	**Acc**	**Comp**	**Acc**
2014	A.Kumar et al. [132]	1.00	0.93	1.00	1.00	0.92	0.79	1.00	0.83	1.00	0.94
2014	Spanier and Joskowicz [129]	1.00	0.93	1.00	1.00	0.85	0.81	0.90	0.82	1.00	0.94
2014	Ermis and Cemgil [130]	0.62	0.88	1.00	1.00	0.46	0.77	0.20	1.00	0.12	0.15
2015	Method n°2 [7]	1.00	0.92	1.00	1.00	1.00	0.75	1.00	0.48	0.96	0.89
2017	Method n°3 Descriptor n°2 [8]	1.00	0.92	1.00	1.00	1.00	0.67	1.00	0.51	0.96	0.89

Table 3.5: The comparison of test results [8] [6]

results with the results of 2014 version.
We recall that the dataset of ImageCLEF2014 liver CT annotation challenge was similar to dataset 2015, in addition it contains a set of 60 features extracted from each image.

In ImageCLEF2014 liver CT annotation challenge, Kumar et al. [132], Spanier and Joskowicz [129], Ermis and Cemgil [130] have participated to the challenge, where kurmar's method achieved the first place of this version. Table 3.5 shows the details for each method.

Table 3.5 shows that all authors have completed the liver annotation with accuracy more than 90% except the method proposed in [130]. In other side, they annotated completely and successfully the vessels proprieties.
The two proposed methods are the only ones that annotated completely the concepts related to lesion-area, however a remarkable accuracy difference is obtained between the two methods. The method n°3 achieved a low accuracy compared to the method n°2, this could be explained by the loss of information due to the Bidimensional Empirical Mode Decomposition, which affected the precision of annotation.
The concepts related to lesion-lesion are annotated completely by [132] and our two proposed approaches. However, [132] has got the accuracy of 83% by using a feature set of size 1446, while we achieved 48% and 51%. We attribute this difference to the size of features set which has significantly improved the accuracy of the annotation.
Lesion-components group are annotated with a score higher than 90% by [132] [129] and our two methods [7] [8]. We achieved a completeness score of 96%, and accuracy of 89%.

From the results of the two versions of the challenge, the method proposed by Kumar et al. [132] achieved the first place with a total score of 94.7%, with the difference of 3.7 to our best method (method n°2) [7] that gained a total score of 91% .

A recent study was given by Loveymi et al. [133] in 2020 on ImageCLEF2015 liver CT annotation dataset but using only 43 properties, showed that the features obtained from

GLCMs, Gabor wavelet transform, SURF and their proposed descriptor named Deep Local Binary Pattern (DLBP) gave the accuracy of 93.1%.
It is interesting to note that one of the major considerations in the annotation of the liver is the appropriate combination of features.

3.4 Conclusion

In this chapter, we have presented the methods developed to annotate liver CT scans. The methods have different features descriptors and were based on different strategies such as classification and CBIR. The experiments conducted on the ImageClef 2015 annotation dataset showed that the second proposed method based on the signature of the liver, achieved the best result compared to the remains proposed methods.
This method is based essentially on the features of the image. In order, to improve the efficacy of this method we plan in our futures works to investigate the semantic reasoning by using the ontology ONLIRA.

Chapter 4

Mammographic image classification

4.1 Introduction

Breast cancer affects one in nine women during their lives [245]. It is one of the leading causes of cancer mortality among women in the world.
The mammography is the preferred screening examination for breast cancer used by radiologists, where they estimate the breast density by visual examination of mammography. The low energy X-rays in mammography are used to analyze the breast tissue, and the composition of tissue can predict cancer risk. Patients with higher density breast tissue need to receive special attention since pathologies tend to be hidden by dense backgrounds.

In this work, a CAD system is proposed to classify breast parenchyma tissue using a new approach based on the distribution of the potential correlation of textons.
Furthermore, the CAD system includes a proposed modified Synthetic Minority Over-Sampling Technique Algorithm (SMOTE) allowing equilibration of the datasets.

In this chapter, we present the proposed CAD system and it validation using experimental tests. For this, different datasets were used, in addition, parametrical sensitivity of the proposed methods were investigated to evaluate the main influent parameters and to choose the best combination for the final test. Then the comparisons with the stat-of-the-art results were presented and discussed. In section 4.5, we present our participation in the Digital Mammography DREAM Challenge, which was synchronized with our development of the method. This participation allowed us to see the shortcomings of the method, after the challenge we have introduced the necessary improvements in the method.

4.2 Method

Traditional approaches use images pixels for features descriptors extraction. The approach that we propose for our CAD system is based on textons to classify breast parenchyma tissue. In this method, the images are mapped to a co-occurrence matrix that models the distribution of a defined textons. From the co-occurrence matrix, a set of features are extracted to build the training dataset. In this section, we explain the tree processes involved in the CAD system

that we propose to model the breast parenchyma tissue:

- Textons extraction
- Features descriptor extraction
- Classification process using the modified SMOTE algorithm

4.2.1 Textons extraction

The objective of this task is to represent all the images dataset with a defined pattern of textons. The set of textons are determined from all the images of the dataset and the selection of textons are defined by a frequency range and using the k-means algorithm.
Textons extraction step is organized as follows:

1. First, all the images are rotated (to get the same position for the left and the right breast) and for each input image, textons of size 'N × N' pixels which are spaced by 'M' pixels are extracted
2. Then, for each texton, the following features are calculated: mean, variance, standard deviation, skewness, kurtosis, entropy and energy
3. Next, k-means is used to cluster the textons of the input image to extract the centres textons of the image (we note 'W' the number of image centres)
4. The frequency of the centre given by the number of textons belonging to this centre divided by the total number of textons is calculated
5. All the centres of all images of the training dataset which have a frequency higher than a specified threshold are grouped into one set, (we note 'F' the selection frequency)
6. k-means method is used to extract from the obtained set in step 5, the most represented centres of the dataset. The obtained set is called the dataset-centres (we note 'C' the number of dataset centres). This dataset-centres-set will be used in the next steps

Figure 4.1 shows the schema of textons extraction.

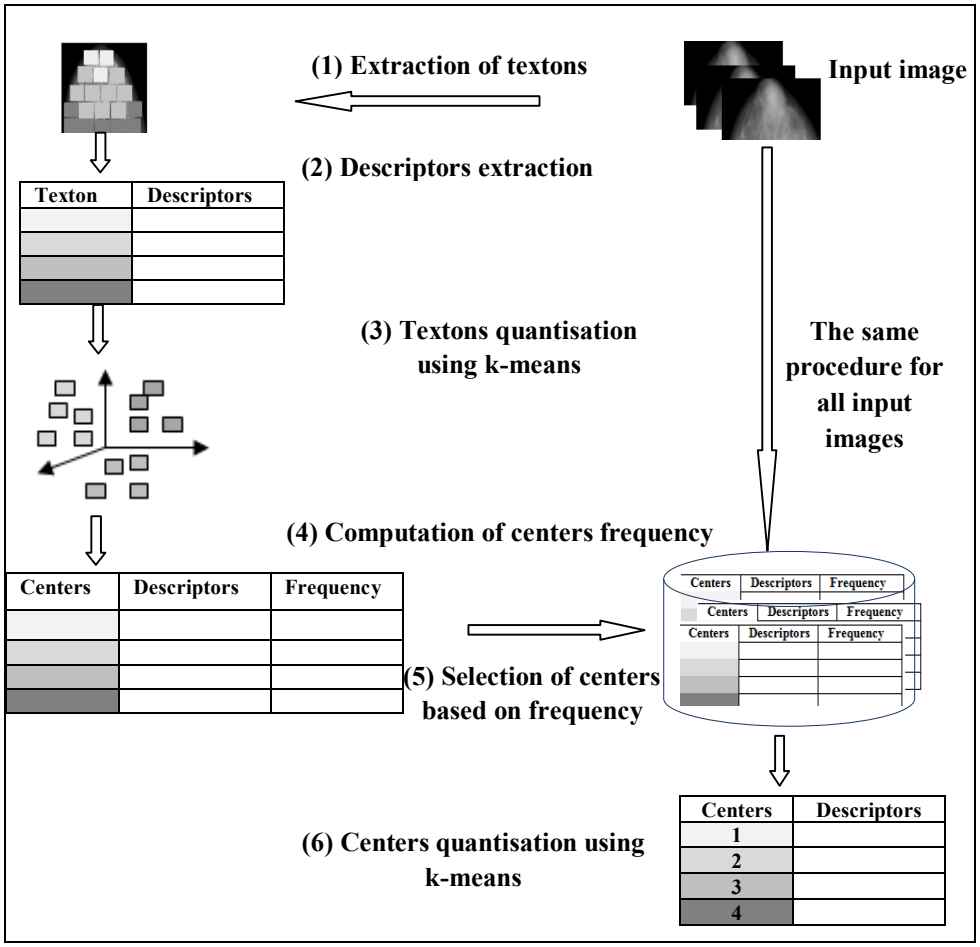

Figure 4.1: Textons extraction

4.2.2 Features descriptors extraction

The dataset-centres-set extracted are used to map each input image to a co-occurrence matrix, then we extract a set of features. The process of features extraction for training and test images follows these consecutive steps:

1. The descriptors of all textons of the image are extracted; this step is done only for the test images because the descriptors of training images are already extracted at the second textons extraction stage

2. Then, each texton in the image is represented by the index of the nearest centre of the dataset-centre-set. The nearest centre is chosen by computing the Euclidian distance between each texton descriptor and the centres descriptors

3. Thereafter, the spatial GLCM [216] is created

4. From the co-occurrence matrix, we have computed the histogram and we have extracted the following features: mean, variance, standard deviation, skewness,

kurtosis, entropy and energy. In addition, we have computed the Haralick features [216] and features proposed by Soh and Tsatsoulis [236] using four different directions 0°, 45°, 90°, and 135°; and distances equal to 1, 5 and 9. The features extracted are: autocorrelation, contrast, correlation, cluster prominence, cluster shad, dissimilarity, energy, entropy, homogeneity, maximum probability, variance, sum average, sum variance, sum entropy, difference variance, difference entropy, information measure of correlation 1, information measure of correlation 2, maximal correlation coefficient, inverse difference, inverse difference normalized and inverse difference moment normalized. So, the final descriptor contains all the extracted features

Figure 4.2 shows the schema of features descriptor extraction.

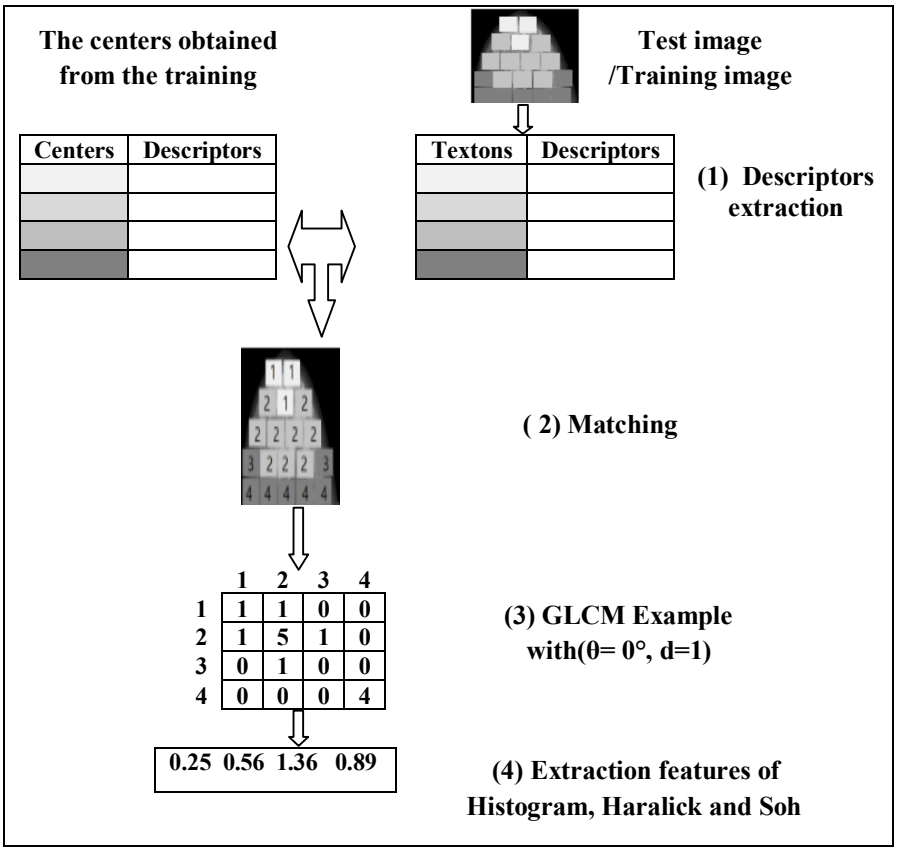

Figure 4.2: Features descriptor extraction

4.2.3 Classification process using the modified SMOTE algorithm

The features extracted are used to train a Random forest classifier in order to generate the classifier model. Inasmuch as the dataset is imbalanced, we propose to apply a step of equilibration before training. When the model is generated, the classifier can predict a new instance. The process of training and prediction follows these consecutive stages (see Figure 4.3):

1. First, we use the proposed modified SMOTE to balance the dataset
2. Then, we train the dataset by using Random Forest Classifier
3. Consequently, the classifier model is generated
4. Next, we classify a novel instance by using Random forest classifier model. The output of the classifier model is the predicted class. As result the class instance is given by the classifier

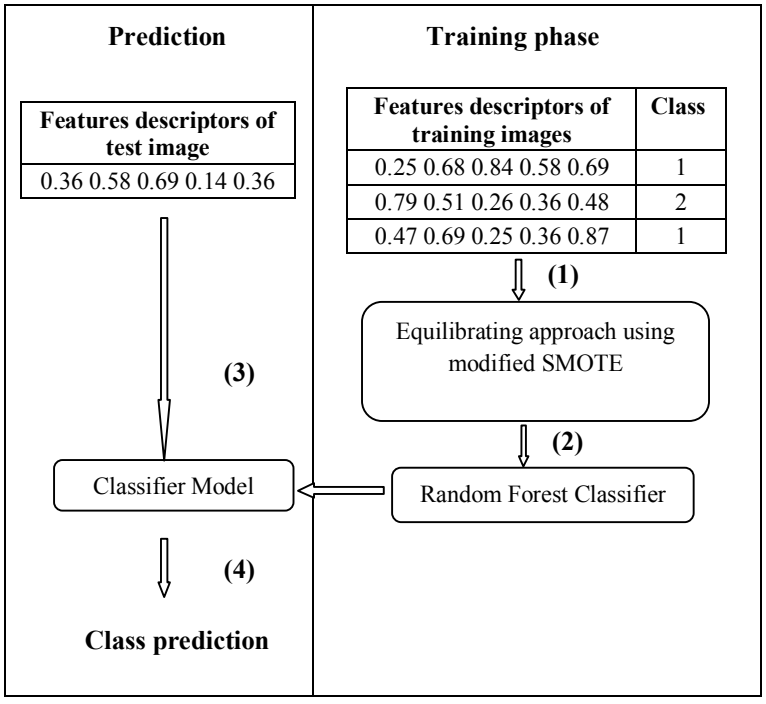

Figure 4.3: The classification process proposed

As it can be seen in the experimental results presented in section 4.3, the application of this procedure will induce a relative accuracy of prediction. The datasets are imbalanced, however using the SMOTE balancing algorithm improved the performance results. Thus, the equilibration of the dataset is a crucial step in the proposed method. In the following paragraph, the proposed modification of the SMOTE algorithm is presented.

A. *The proposed modified SMOTE algorithm*

Our goal is to achieve an equilibration of the dataset on the basis of an improved SMOTE algorithm. The SMOTE algorithm proposed by Chawla et al. [246] is as follow:

Algorithm 1: SMOTE (T, N, k)

Result: (N/100)*T synthetic minority class samples
Input: Number of minority class samples T; Amount of SMOTE N%; Number of nearest neighbours k;
(If N is less than 100%, randomize the minority class samples as only a random percent of them will be SMOTEd.*)*;
if *(N <100)* **then**
    Randomize the T minority class samples (***);
    T = (N/100) * T;
    N = 100;
end
N = (int)(N/100) *(* The amount of SMOTE is assumed to be in integral multiples of 100*)* ;
k = Number of nearest neighbours;
numattrs= Number of attributes;
Sample[ ][ ]: array for original minority class samples ;
newindex: keeps a count of number of synthetic samples generated, initialized to 0 ;
Synthetic[ ][ ]: array for synthetic samples ;
(Compute k nearest neighbours for each minority class sample only.*)*;
for $i \leftarrow 1$ **to** T **do**
    Compute k nearest neighbours for i, and save the indices in the nnarray;
    Populate(N, i, nnarray);
end
Function `Populate(`N, i, $nnarray$`):`
    (* Function to generate the synthetic samples.*);
    while $N \neq 0$ **do**
        Choose a random number between 1 and k, call it nn. This step chooses one of the k nearest neighbors of i;
        for $attr \leftarrow 1$ **to** $numattrs$ **do**
            dif= Sample[nnarray[nn]][attr]−Sample[i][attr];
            gap = random number between 0 and 1;
            Synthetic[newindex][attr] = Sample[i][attr] +gap∗dif;
        end
        newindex++;
        N = N − 1;
    end
    return *(*End of Populate.*)*

The SMOTE method synthesizes randomly the minority instances along a line joining a minority instance and ignoring nearby majority instances. This drawback has an important impact on the results. We have made the modification of the SMOTE algorithm [246] in the random instruction (is marked by *** in the Algorithm 1), in which we have replaced the step of randomization by selection. More precisely we

have selected the minority instances to be over-sampled. The process of selection is based on finding the minority instances that are the most close to all others minority instances in the dataset.
The selection process follows these consecutive stages:

1. For each minority instance we extract the k-nearest neighbours
2. Thereafter, we compute the number of apparition of each minority instance in the k nearest neighbours of all minority instances, and we store the score for each position separately (for example the instance x, occurs as the first nearest #3, as second nearest #6 ,..,as the k nearest #5)
3. Then, we calculate the weighting vector, by dividing each number of occurrence by his number of position (for example the weighting vector for x is [3/1, 6/2,...,5/k])
4. Next, we compute the weighting value for each minority instance by summing the values of the weighting vector, (for example the weighting value for x is 3/1+ 6/2+...+5/k)
5. Finally, we select the k instances that have the maximum weighting value. These instances are selected to generate the synthetic instances

The instances given by the array result of the selection Pseudocode are used to generated the synthetic instances of the minority class.
The parameter k of the k-nearest neighbours is defined as follow:

$$K = (N/100) * T \tag{4.1}$$

Where T is number of minority class samples and N is the amount of SMOTE.
The selection Pseudocode is presented as follows:

Algorithm 2: selection Pseudocode (T, N, k)

```
Result: result[K]: array that contains the indices of the salient instance
Input: Number of minority class samples T; Amount of SMOTE N%; Number of nearest neighbours
  k;
(*initialization*)
closedarray [T][K]: array for indices instance;
coeftarray [K]: 1..K ;
weighinstances [K]: initialized to 0 ;
weightarray [T]:array that contains the sum of weights for each instance;
(*Compute k+1 nearest neighbours for i, and save the indices in the closedarray, then the first nearest
  neighbours is excluded because it is the same instance*)
for i ← 1 to T do
    closedarray [i][k+1]=indice;
end
closedarray= closedarray[:][2:k+1] ;
(* Compute the weight instances*)
for m ← 1 to T do
    for i ← 1 to T do
        for j ← 1 to K do
            if (closedarray[i][j]==m) then
                weighinstances [j]= weighinstances [j]+1;
            end
        end
    end
    S=0;
    for j ← 1 to K do
        S=S+( weighinstances[j]/ coeftarray[j]);
    end
    weightarray [m]=S;
    (*initialization to 0*)
    for j ← 1 to K do
        weighinstances[j]=0;
    end
end
(*We select the K indices that have the maximum distance.*)
c=0 ;
while c<K do
    max=weightarray[1];
    indice=1;
    for i ← 2 to T do
        if (weightarray[i]>max) then
            max = weightarray[i];
            indice=i;
        end
    end
    weightarray[indice]=-inf;
    c=c+1;
    result[c]= indice;
end
```

4.3 Experimental results

4.3.1 Evaluation criteria

The measures considered for the evaluation of the experiments are performed on the basis of accuracy, precision, recall and kappa statistic.

$$Accuracy = \frac{TP + TN}{TP + TN + FP + FN} \tag{4.2}$$

$$Precision = \frac{TP}{TP + FP} \tag{4.3}$$

$$Recall = \frac{TP}{TP + FN} \tag{4.4}$$

$$Kappa = \frac{(Po - Pe)}{(1 - Pe)} \tag{4.5}$$

TP is true positive, the number of positive cases that are correctly identified as positive cases.
TN is true negative, the number of negative cases that are correctly identified as negative cases.
FP is false positive, the number of negative cases that are incorrectly identified as positive cases.
FN is false negative, the number of positive cases that are incorrectly identified as negative cases.
Kappa Statistics is based on the difference between how much agreement is actually present ("observed" agreement-Po) compared to how much agreement would be expected to be present by chance alone ("expected" agreement-Pe) [247].

4.3.2 Equilibrating approach

In order to check the efficiency of the modified SMOTE method proposed versus the basic SMOTE, the experiment studies the cases of two-class and multiclass problem by using different classifiers on two datasets.

A. *Datasets*

Two datasets from the UCI Machine Learning Repository [248] are used: Wisconsin Breast Cancer (WBC), and Breast Tissue with 6 class. The two datasets describe the breast (see Table 4.1).

We refer that a pre-processing of the dataset WBC has been done. In fact, each instance with a missing attribute values is eliminated. In total 16 instance were excluded.

B. *Experimental results*

The experiments were carried out by using three different classifiers: Random Forest

Data set name	Number of Classes	Number of Attributes	Number of Examples
WBC	2	10	699
Breast Tissue	6	10	106

Table 4.1: Datasets characteristics

[240], Multilayer Perceptron [249] and Bayes Network [250].

The performance estimation of each classifier is obtained by means of 10-fold cross-validation. We mention that the experiments include the synthetics samples in the test step to evaluate their quality. Table 4.2 shows that the proposed method gives the best accuracy for the two datasets WBC and Breast Tissue with 6 Class whatever is the classifier.

The Breast Tissue with 6 Class is a multiclass dataset. Therefore, balancing the distribution of dataset is much challenging to get better accuracies. In this case, the proposed method meets this challenge and outperform the basic SMOTE with accuracy gap of 1.52%, 2.27% and 3.79% using respectively Random Forest, Multilayer Perceptron and Bayes Network classifier. We notice that for all cases, the Random Forest with the proposed method gives the best results.

Datasets	Classifier	Models	Precision	Recall	Kappa statistic	Accuracy (%)
WBC	Random Forest	**The proposed method**	**0.986**	**0.985**	**0.970**	**98.536**
		SMOTE	0.982	0.982	0.964	98.198
	Bayes Network	**The proposed method**	**0.982**	**0.982**	**0.964**	**98.198**
		SMOTE	0.980	0.980	0.959	97.973
	MLP	**The proposed method**	**0.977**	**0.976**	**0.952**	**97.635**
		SMOTE	0.972	0.972	0.943	97.184
BT- 6 Class	Random Forest	**The proposed method**	**0.799**	**0.803**	**0.763**	**80.303**
		SMOTE	0.784	0.788	0.745	78.787
	Bayes Network	**The proposed method**	**0.693**	**0.697**	**0.636**	**69.697**
		SMOTE	0.661	0.674	0.609	67.424
	MLP	**The proposed method**	**0.729**	**0.742**	**0.690**	**74.242**
		SMOTE	0.681	0.705	0.645	70.454

Table 4.2: Comparison of the proposed method with SMOTE

4.3.3 CAD system for mammography image classification

In order to validate the whole CAD system (Textons based feature description and equilibration), the following tests are carried out on the Mammographic Image Analysis Society (mini-MIAS) database and the Digital Database of Screening Mammography (DDSM).

For each dataset, we start by the presentation of the dataset then a sensitivity study of the algorithm parameters and the classifier are investigated, and finally the comparison of the results obtained with and without equilibration is presented. The last paragraph gives conclusions of the accuracy of the CAD when different datasets are used.

A. *DDSM classification*

• Dataset presentation

From DDSM database [251], a set of 424 medio lateral-oblique mammograms is used. For each mammogram, the density of the breast determined by the Breast Imaging Reporting and Data System (BI-RADS) are included. The American College of Radiology (ACR) provides four categories according to breast parenchymal density (see also Figure 4.4):

- BI-RADS I: the breast is almost entirely fatty
- BI-RADS II: there is some fibrogandular tissue
- BI-RADS III: the breast is heterogeneously dense
- BI-RADS IV: the breast is extremely dense

The number of mammograms belonging to each category is equal to 74, 156, 99 and 95 for BI-RADS I, BI-RADSII, BI-RADSIII, BI-RADSIV, respectively.

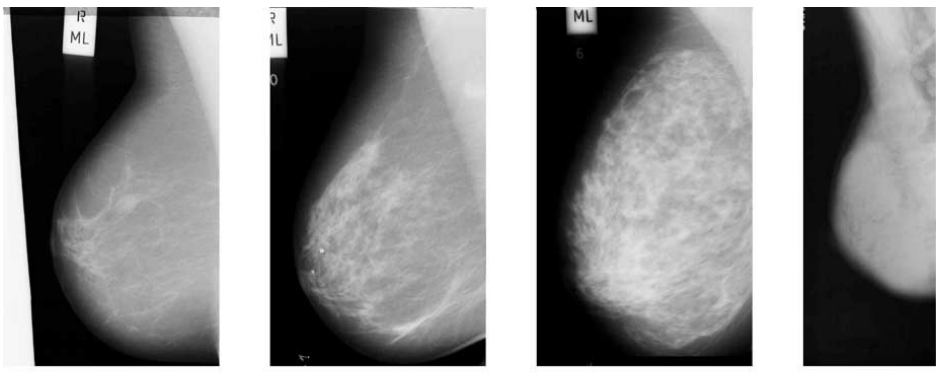

Figure 4.4: Example mammograms (a) BI-RADS I (b) BI-RADS II (c) BI-RADS III (d) BI-RADS IV

Parameters	N	M	W	F	C	Accuracy (%)
Parameter n°1	21	7	15%	0.02	100	62.26
Parameter n°2	61	25	15%	0.02	100	51.02
Parameter n°3	41	15	15%	0.02	100	70.28
Parameter n°4	41	15	10%	0.02	100	65.33
Parameter n°5	41	15	15%	0.02	120	61.08
Parameter n°6	41	15	15%	0.03	100	63.91

Table 4.3: Values of different parameters

• Experimental results

The performance estimation is obtained by means of the leave-one-woman-out methodology, i.e., the left and right mammograms of a woman are analyzed by a classifier trained using the mammograms of all other women in the dataset. The leaveone- woman-out methodology is used to avoid bias as the left and right mammograms of a woman are expected to have similar internal morphology [164].

A sensitivity study of the algorithm parameters is carried out in order to select the best combination for the next tests. The algorithm presented in section 4.2 has different parameters including: the size of textons N×N, the distance between textons M, the number of image centers W, the value of the selected frequency F and the number of the dataset-centers C.

Table 4.3 shows the different parameters tested. (Note that Random Forest classifier with 300 trees is used, furthermore, the tests are done without equilibration for this experimentation).

The textons N-M tested are 21-7, 61-25,41-15, the accuracy obtained was 62.26%, 51.02%, 70.28% respectively, for the rest of experiments N=41 and M=15 are used.

For the quantization, we have taken 10% and 15% of textons image to build the centers of image. The obtained results were 65.33% and 70.28%. So, we have chosen 15% of textons from each image.

For frequency selection, we have tested F=0.02 and F=0.03, the results were 70.28% and 63.91%.

Finally, for the number of centers of dataset we have tested C=100 and C=120, the best results are given using 100 centers. For the rest of experiments, we have used the third parameter (N=41, M=15, W=15%, F=0.02, C=100). After the selection of the parameters of the algorithm, the parameter of the classifier was investigated.

Several experiments have been done (see Figure 4.5) to choose the optimal number of trees for Random Forest. We notice that the accuracy given by 300 trees was 70.28% and 71.22%, for 150 trees was, therefore 150 trees was chosen. After the calibration of the model and the classifier, we proceed with the final test including the

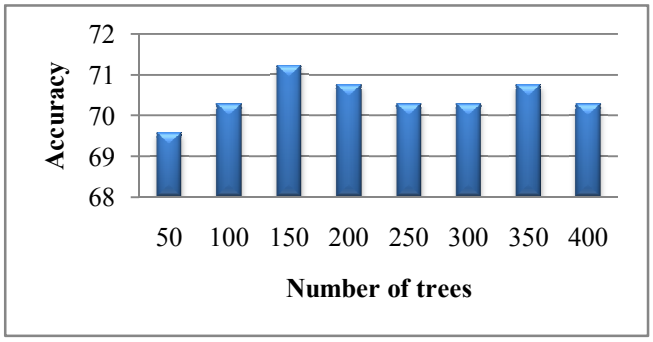

Figure 4.5: Accuracy related to different number of trees

equilibration. Table 4.4 shows the confusion matrix of breast density classification without equilibration, equilibration with SMOTE and using the modified SMOTE.
In order to have a detailed analysis, the results will be presented for each class separately.
The performance of the classification is improved by using equilibrated dataset from 71.22% to 83.25%.
The classification results of the imbalanced dataset in Table 4.4.(A) is better for majority classes compared to minority classes. This is due to the fact that the classifier is biased by the number of images in the majority classes. Thus, the accuracy for the class BI-RADS II are higher than the class BI-RADS I by 32.62%. By using equilibration with SMOTE in Table 4.4.(B), the accuracy of minority class is improved. Unfortunately, the majority class obtained a lowest accuracy of 75.64% (compared to 83.97% for imbalanced dataset).
The modified SMOTE in Table 4.4.(C) improves the total accuracy. In addition, the improved method overcomes the problem of imbalanced accuracy for minority and majority class. (Accuracy is over 80% for all classes).

(A) Total Accuracy 71.22 %					
BI-RADS	**I**	**II**	**III**	**IV**	**Accuracy(%)**
I	38	32	3	1	51.35
II	15	131	8	2	83.97
III	0	13	72	14	72.72
IV	3	18	13	61	64.21
(B) Total Accuracy 79.71 %					
BI-RADS	**I**	**II**	**III**	**IV**	**Accuracy (%)**
I	65	8	1	0	87.83
II	24	118	8	6	75.64
III	1	5	84	9	84.84
IV	4	9	11	71	74.73
(C) Total Accuracy 83.25%					
BI-RADS	**I**	**II**	**III**	**IV**	**Accuracy (%)**
I	66	5	3	0	89.18
II	19	125	8	4	80.12
III	0	9	81	9	81.81
IV	3	5	6	81	85.26

Table 4.4: Confusion matrix of breast density classification: (A) Without equilibrating, (B) The SMOTE algorithm, (C) The modified SMOTE

In order to compare the quality of the synthetic data created by the modified and original SMOTE algorithm, classification accuracy was conducted only with synthetic data. The BI-RADS II was not investigated due to the fact that this class has the majority images and no synthetic data were created for it.

The obtained results shown in Figure 4.6 demonstrated the quality of the synthetic data for BI-RADS I and BI-RADS IV generated by the modified SMOTE algorithm.

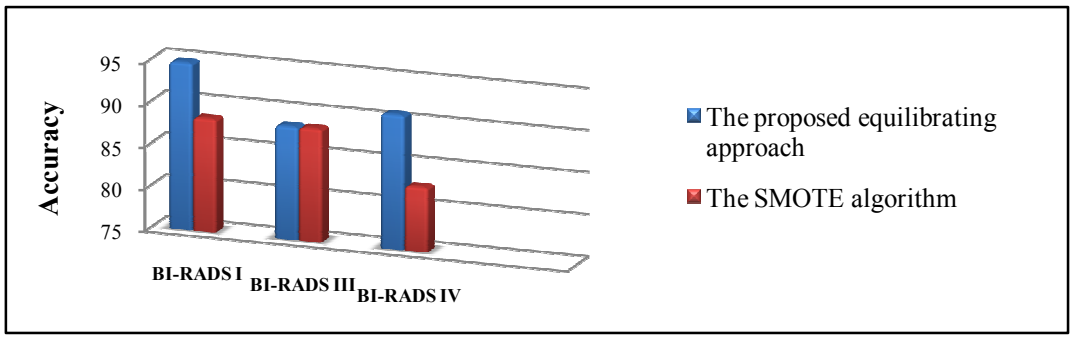

Figure 4.6: Accuracy obtained for the synthetic dataset of BI-RADS I, BI-RADS III, BI-RADS IV

Parameters	N	M	W	F	C	Accuracy (%)
Parameter n°1	21	7	15%	0.02	100	89.13
Parameter n°2	21	7	10%	0.02	100	85.71
Parameter n°3	21	7	15%	0.03	100	84.16
Parameter n°4	31	10	15%	0.02	100	90.99
Parameter n°5	31	10	15%	0.02	120	89.44
Parameter n°6	11	5	15%	0.02	100	87.57

Table 4.5: Values of different parameters

B. *MIAS classification*

• Dataset presentation

The dataset mini-MIAS [252] contains 322 images in Medio Lateral-Oblique (MLO) view. The images in this dataset are classified into three categories based on their density as fatty, fatty-glandular and dense-glandular. In this study, all the fatty-glandular and dense-glandular mammograms are treated as one group of dense mammograms according to what as was used in several related works (Chen et al. [253]; Kriti et al. [169] ; Muštra et al. [167]; Oliver et al. [164]; Virmani and Kriti [170]), thus two-classes are defined fatty and dense, we have 106 and 216 images respectively

• Experimental results

Several experiments were achieved in order to select the best parameters. The classification was achieved by using Random Forest (100 trees) and the leave-one-woman-out methodology, furthermore, the tests are done without equilibration.

We can see from Table 4.5 that the best parameters are: N=31, M=10, for the quantization W=15%, 0.02 for frequency and C=100 for number of center of dataset . For the rest of experiments, we have used the fourth parameter.

Table 4.6 shows the confusion matrix of the breast density classification without equilibration, by using equilibration with SMOTE and by using the modified SMOTE. It can be observed that the accuracy of classification is improved by using equilibration methods with 0.31% for SMOTE and 3.42% for the modified SMOTE.

We notice also that the best score of dense category is given by the imbalanced dataset. This is because the classifier is biased by the majority category that represent 67.08% of dataset. On the other hand, the modified SMOTE gave the best accuracy for the minority category with an accuracy of 94.34% compared to 91.51% and 81.13% for SMOTE and the imbalanced dataset respectively. At the same time, it keeps the accuracy of majority category height.

We attribute the efficiency of the modified SMOTE algorithm compared to the basic SMOTE algorithm to the quality of the synthetic data used in the training step.

In fact, by computing the accuracy of classification of these data only, we obtained

100% of correct classification for the modified SMOTE algorithm and 91.82% for SMOTE algorithm.

(A) Total Accuracy 90.99%			
Categories	**Fatty**	**Dense**	**Accuracy(%)**
Fatty	86	20	81.13
Dense	9	207	95.83
(B) Total Accuracy 91.30 %			
Categories	**Fatty**	**Dense**	**Accuracy (%)**
Fatty	97	9	91.51
Dense	19	197	91.20
(C) Total Accuracy 94.41%			
Categories	**Fatty**	**Dense**	**Accuracy (%)**
Fatty	100	6	94.34
Dense	12	204	94.44

Table 4.6: Confusion matrix of breast density classification: (A)Without equilibrating, (B) The SMOTE algorithm, (C) The modified SMOTE

C. *Discussion on the experimental results*

We notice that the same parameters of the algorithm (frequency, quantization and number of centers) give the best results for MIAS and DDSM. The difference on the parameterization is related to the size of textons (N) and the space between textons (M). We attribute this difference to the size of the image of the two datasets, in fact the images in DDSM are much bigger than the images in MIAS. (In DDSM textons parameters are N=41, M=15, for MIAS N=31, M=10).

In addition to this, the modified SMOTE algorithm achieves the best results for each dataset. As demonstrated earlier this is related to the quality of the synthetic data used in the training step.

Based on these results, it can be concluded that the CAD system present good stability related to the used datasets.

4.4 Comparative study with related works

In this section, both comparison with state of the art for the equilibrating approach and CAD system are presented and commented.

4.4.1 Equilibration approach

First, to demonstrate the effectiveness of the modified SMOTE algorithm, a comparative study with related works regarding the equilibrating approach is presented in Table 4.7.

Datasets	Reference	Models	Accuracy %
WBC	**The proposed method**	**Random Forest**	**97.51**
	Wang et al. [254]	S-AIRS	96.91
Breast-Tissue-6 C1ass	**The proposed method**	**Random Forest**	**77.36**
	Tallón-Ballesteros et al. [255]	TSEAFS	60.93
	Mantovani et al. [256]	SVM	42
	Belarouci et al. [257]	KNN+LMS	71.43

Table 4.7: Comparison of the proposed modified SMOTE with studies in literature

We mention that the synthetics samples were used only in training step in order to avoid biasing in classification accuracy.

• WBC Dataset

Wang et al. [254] proposed a hybrid method by combining Synthetic Minority Over-Sampling Technique (SMOTE) and Artificial Immune Recognition System (AIRS) called SAIRS. SAIRS obtained an accuracy of 96.91% for the dataset WBC.

We obtained an accuracy of 97.51 % which is better than the result given by SAIRS.

•Dataset Breast-Tissue-6 Class

Tallón-Ballesteros et al. [255] proposed a method called TSEAFS, to reduce the complexity of Evolutionary ANNs (EANNs). TSEAFS has been tried out with four filters. The best accuracy of 60.93% is given by using the Fast Correlation-Based Filter.

Mantovani et al. [256] used the Random Search (RS) method with the Genetic Algorithm (GA) for adjusting hyper-parameters of Support Vector Machines, using the dataset Breast-Tissue-6 Class the accuracy of 42% is obtained.

Belarouci et al. [257] have proposed a learning method based on a cost sensitive extension of Least Mean Square (LMS) algorithm. After the balancing phase, they used different classifiers SVM, K-NN and MLP. The best score of 71.43% is given by both MLP and K-NN.

For the dataset Breast-Tissue-6 Class, our proposed method achieved a good performance compared to the above-mentioned methods.

4.4.2 CAD system for mammography image classification

A performance comparison of the proposed CAD system and those of different studies in the literature presented in sate of the art chapter (2.3) is given in Table 4.8. Note that the performances of all these methods were evaluated using DDSM and MIAS datasets.

A. **DDSM dataset**

Bovis and Singh [159] used 377 MLO images, and achieved an overall correct classification of 71.4%.

Oliver et al. [164] improved their proposed approach presented in [161] by using more features and using a Bayesian combination of a number of classifiers. Therefore, the accuracy of 47% was enhanced to 77%.

The proposed method is more accurate than the methods presented in [159] and [161] in spite of using more images (424 images).

Bosch et al. [162] have achieved the accuracy of 84.75%, we attribute this achieved performance to the size of the descriptors used.

B. **MIAS dataset**

Oliver et al. [164] classified mammograms in two categories fatty and dense; they have achieved 89% accuracy for low density, 94% for high density and the total score was 91%. Chen et al. [253] and Muštra et al. [167] obtained precision rates of 88% and 91.6% of correct classified images respectively. The proposed method outperform the methods presented in (Chen et al. [253] ; Kriti et al. [169]; Muštra et al. [167]; Oliver et al. [164]) excepte for [170]. The methods proposed given in (Kriti et al. [169];Virmani and Kriti [170]) used a manual selection of region of interest (ROI) from the central breast region that contains tissue pattern only. This process is not automatic and time consuming. Instead, our method does not use a manual process which makes it easier to use.

All the presented results in this chapter are given in the paper ”A Topological Approach for Mammographic Density Classification Using a Modified Synthetic Minority Over-Sampling Technique Algorithm” [258].

Dataset	Author(s)	Accuracy (%)
DDSM	Bovis and Singh [159]	71.4
	Oliver et al. [161]	47
	Bosch et al. [162]	84.75
	Oliver et al. [164]	77
	The proposed approach	83.25
MIAS	Oliver et al. [164]	91
	Chen et al. [253]	88
	Muštra et al. [167]	91.6
	Kriti et al. [169]	94.4
	Virmani and Kriti [170]	96.2
	The proposed approach	94.41

Table 4.8: Accuracy comparison of the proposed method with studies in literature using DDSM and MIAS

During the development phase of the method, we tested it in the international challenge named the Digital Mammography DREAM (Dialogue for Reverse Engineering Assessment and Methods), to evaluate it and to make the necessary improvements.
In the following section we will present in detail this challenge and the changes that we have made on the method after the challenge.

4.5 The Digital Mammography DREAM Challenge

4.5.1 Objective of the challenge

The aim of the Digital Mammography DREAM Challenge is to establish a new quantitative tool that help to reduce the recall rate for breast cancer screening. In fact, the tool define the likelihood that a patient can be diagnosed with cancer within one year from the given screening digital mammography, and this is done without access to previous exams or historical, clinical and demographic information.
The participants were asked to submit a model that have the input and the output as following:
Input: A screening mammography exam consisting of several images of both breasts.
Output: Two scores, the left breast score and the right breast score, each between 0 and 1, That indicating the likelihood that the subject was tissue-diagnosed with cancer within one year from the given screening exam [4].
The Digital Mammography DREAM Challenge was divided into a Competitive Phase, followed by a Community (collaborative) Phase.
Competitive phase, had three rounds that allows the teams to adjust their models and a final round, in which the best teams were selected to the community phase.
Community phase regroup the teams with the highest predictive performance, they work

together as one team leading by experts in the field, with the goal of building a predictive model that exceeds the performance of the best method from the competitive phase.
A big funding has been dedicated to the challenge by Laura and John Arnold Foundation, Coding4Cancer and White House Office of Science and Technology Policy, in which, up to $1.0 million in prize money was made available to the community phase group based on successful completion of milestone objectives [4].

4.5.2 Dream Mammography Challenge timeline

In the DREAM Mammography Challenge there were four phases: open phase from September 2016 to November 2016, leaderboard phase from November 2016 to March 2017 and validation phase from March 2017 to May 2017 phases, which together constitute the competitive phase. The community phase from July 2017 to November 2017 (see the Figure 4.7).
In the open phase, the teams got the time to exercise the challenge infrastructure before the competition. The Leaderboard phase was composed of three round and the validation phase contain the final round of the competitive period where participants submitted their final models for scoring.

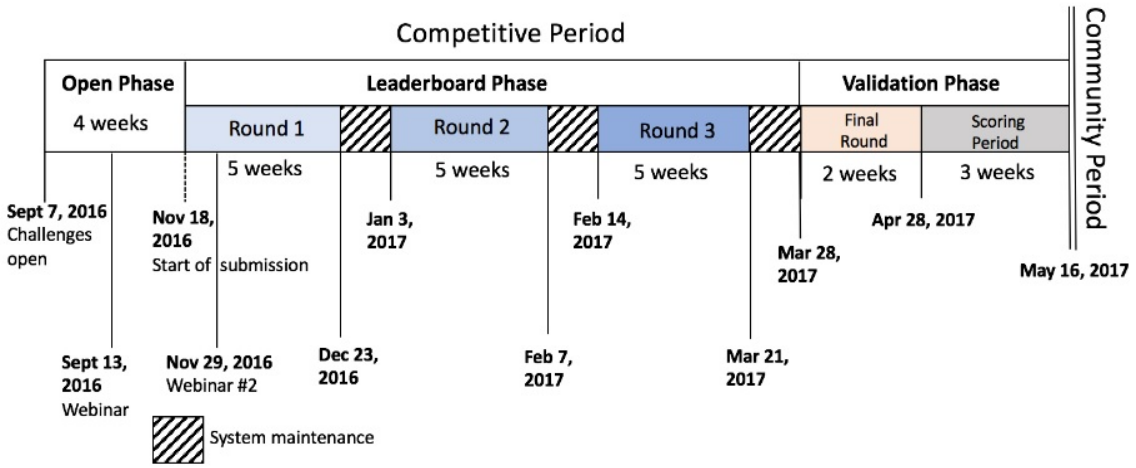

Figure 4.7: The timeline of the Dream Mammography Challenge [4]

4.5.3 Dataset

The Group Health Cooperative (funded by the National Cancer Institute of USA, through Grant No. 5PO1CA154292-05), has provided over 640000 de-identified mammography images from 86000 exams.
The digital mammography images are provided in DICOM format with different sizes ranging from 3328x2560 to 5928x4728 pixels. The DICOM header of these images, have all been de-identified by Group Health, only a binary label was given, that indicate if breast

cancer was diagnosed in the next 12 months after the exam. The mammography image data of the challenge, was not available for download by participants. So, both the training and prediction generation were done on the challenge cloud, given by IBM SoftLayer and Amazon Web Services. The participants were asked to submit trainable model in the form of a Docker[1] image. The machines in the cloud run the training phase using the training data and the test phase using trained model and the test data.
Figure 4.8 shows an example of craniocaudal (CC) view and mediolateral oblique (MLO).

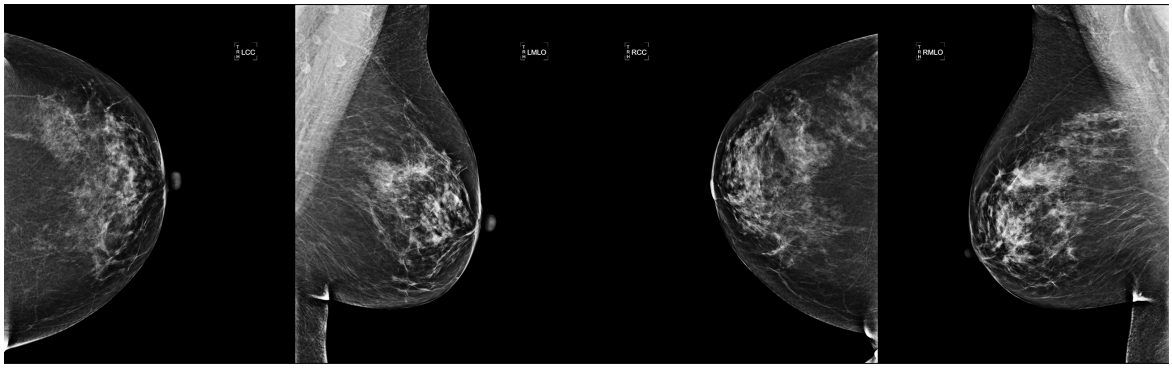

Figure 4.8: CC and MLO views of the left and the right breast

4.5.4 The model submitted

The goal of the challenge was to predict the probability that a patient can develop cancers within 12 months based on mammographic images. Several studies have shown that the breast density is an important breast cancer risk factor [259][260].
Indeed, they indicate that the increase in the breast density is one of the strongest indicators of developing breast cancer.
So, to meet the Digital Mammography DREAM Challenge and to evaluate the initial version of our method, we tested it to automatically discover the development of breast cancer. We entered to the challenge in the validation phase with the alpha version of the method [261]. In fact, at this time the Textons extraction step and Features descriptor extraction step where developed, unfortunately we didn't have time to test the main hyper parameters of the method.
In the Textons extraction step (describe in section 4.2.1), for each image in the training data, textons with a size of 200×200 pixels were extracted, then the mean, variance, standard deviation, skewness, kurtosis, entropy and energy are computed for each texton. Next k-means was used to cluster the textons, we have taken W=15% that represent the number of image centers. The obtained centers of all images of the training dataset which have a frequency higher than 0.02 (F=0.02) are grouped into one set. Finally by using k-means the most represented centers (Dataset-Centers-Set) of the training dataset were extracted, we

[1] Docker is a technology for creating portable virtual machines

have taken C=100.
In Features descriptor extraction step, the Dataset-Centers-Set extracted are used to map each input image to a co-occurrence matrix, then we have extracted a set of features. Thence, each texton in the image is represented by the index of it nearest center of the Dataset-Center-Set. Thereafter, from the co-occurence table, we have extracted the Haralick and Soh features and also we have computed the mean, variance, standard deviation, skewness , kurtosis, entropy and energy from the histogram.
In the test phase, for each input image we have extracted the features vector as it was described before. Then the Euclidian distance was used to retrieve the most similar images to the image query based on their descriptors, we have taken d=50 and d=100.

4.5.5 Results

Evaluation criteria: the models were evaluated using the area under the receiver operating characteristic curve (AUC) as primary metric. AUC measures the overall performance of a binary classifier [262].

Over 1,100 participants comprising 126 teams from 44 countries entered the challenge, only 31 teams submitted their methods for final validation in the competitive phase, the best-performing method achieved the AUC of 0.855. We have submitted two runs to Digital Mammography DREAM Challenge, in the first one we have used fifty nearest images to compute the voting and for the second we have used one hundred nearest images. For the first submitted run, AUC score of 0.53 is obtained making the method rank #22 in the leaderboard, and the second run we have obtained the AUC score of 0.55 [261].
Table 4.9 shows the result of the final ranking of validation phase.

Ranking	Team	AUC
1	Yaroslav Nikulin	0.87
2	Dezso Ribli	0.85
3	Yuanfang Guan	0.84
4	DeepHealth Mammography	0.84
5	Eagle Eye	0.82
6	Lunit-mammo	0.80
7	42 Is the answer	0.79
8	Vivillon	0.78
9	London Mammo	0.73
10	Donuts	0.70
11	UCSF_MammoDeep	0.69
12	Li Shen	0.65
13	DMIS_mammo	0.63
14	FHDO	0.62
15	Deep Blue Lived	0.61
16	Anamaria Vizitiu	0.61
17	NYU Courant-Medicine	0.59
18	Iulian Stroia	0.59
19	SC1 Baseline Method	0.57
20	Dream9 KTH	0.55
21	Alexandre Cadrin-Chênevert	0.54
22	**Our team**	**0.53**
23	David Gutman	0.52
24	Clinical Persona	0.52
25	Jcb	0.5
26	NCKUBME	0.5
27	SciLifeLab	0.5
28	TranLabRocks	0.49
29	INESCTEC_VCMI	0.49
30	Wolfpack	0.48
31	Rui Hou	0.44

Table 4.9: The result of the final ranking of validation phase of the competitive period [9]

In this paragraph we will present the top 5 performing methods of the DM challenge, for further details about the rest of the methods, we refer the reader to read the overview paper of the challenge titled ” Evaluation of Combined Artificial Intelligence and Radiologist Assessment to Interpret Screening Mammograms ” [16].

The best-performing method of the challenge was proposed by Yaroslav Nikulin member

of Therapixel team [263]. The method was based on detecting DCIS cancer that is characterized by micro-calcifications located in the milk ducts, to that end, a CNN based on modified VGG Net architecture was used. The modified architecture was composed of two parts, the first one consist of 12 convolution layers and 6 pooling layers, that aim to produce a heat map of the image that specify the different type of lesion includes: calcification benign, calcification malignant, mass benign, mass malignant and the case of healthy. For this reason, the network is pre-train on labeled patches from DDSM, where the lesions are annotated. The second part refine the classification to get final cancer probability, therefore three fully connected layers are added on top of this heat map and trained with image labels. The method achieve an AUC score of 0.85.

The method proposed by Ribli et al. [264] is based on lesion detection, the method localize each lesion by a bounding box with a score that represent the degree that a given lesion is benign or malignant. The score affected to the image is the maximum scores of all malignant lesions detected on the image. The authors used Faster R-CNN based on VGG16 to localize lesion on the original image and its horizontally, vertically, and horizontally-vertically flipped versions, and they take the average of the 4 scores. The authors trained the model on DDSM and a private dataset from the Department of Radiology at the Semmelweis University in Budapest, Hungary, because the training dataset of the DREAM mammography challenge does not have pixel level annotation. With an AUC of 0.85 the method achieved the 2nd place in the challenge.

Yuanfang Guan's model achieved the 3rd place in the challenge with an AUC of 0.84, the author trained two types of models. The first model predicts calcification and the number of calcifications, for this full resolution model is trained on small region that allows detection of DCIS. The second model trained on low-resolution to predict masses [16].

DeepHealth team developed a two stage training approach, the first one consist of patch-level classifier and the second is a full-image-level classifier. In the patch-level classifier two ResNet were used, the first CNN trained on patches extracted from larger images size for calcification classification, whereas the second CNN trained on patches extracted from smaller images size for mass classification. In this stage the DDSM dataset was used to construct a training set of image patches, using the available lesions to generate labels. The CNNs were used in the second stage to initialize the full-image level classifier, this model consisted of global average pooling on the convolutional feature maps produced by each patch CNN, followed by concatenation of the two resulting feature vectors that form fully-connected classification layer. This model was again trained on DDSM dataset, and then fine-tuned on the DREAM images. DeepHealth's model achieved the 4th best performer from 31 models with an AUC of 0.84 [16].

The team Eagle Eye guided by Mengling Feng [265], proposed a method that used patches of the full mammogram, this help to reduced the size of the input files while maintaining the resolution required to identify lesion in the mammogram. Then a heat map

containing abnormal lesions are constructed using these patches. The risk score for cancer was calculated based on the number of the lesions found on the heat map. The team achieved the 5th place in the challenge with AUC of 0.82.

4.5.6 Discussion

The top five performing methods of the challenge are based on deep learning, in addition they are composed of two steps. In first one, the lesions (microcalcification and masses) are detected, to that end the patches (textons) of the image are used. In second step, the methods gave the likelihood for each image to develop a cancer within one year, this was conducted by using the result obtained of the first step.
Inasmuch as the training dataset of the challenge didn't contain spatially annotated lesions information, to train these methods they used external datasets like DDSM and the models were refined on the training dataset of the challenge.
Comeback now to the proposed method, initially we have developed it to classify the breast density, we supposed that this approach based on a statistical analysis of breast density can discover the development of breast cancer.

There were two common points between the proposed method and the five top performing challenge method:
The first one, is the use of textons (patches) in order to extract information, because doing the processing directly on the complete image does not give a good prediction score, we mention here that the size of the images were from 3328x2560 to 5928x4728 pixels.
The second point, was to extract the overall relationship between the image patches.
In our case we have used the co-occurrence matrix to extract this relation.

As a point of difference, to solve the problem of imbalance in the training dataset, we used an equal number of images between the class of cancer and non-cancer cases, and as the number of cancer cases has been very limited, the training dataset obtained has been small. Contrary to the five top performing challenge method, where they use image data augmentation (the method of deep learning) to make the balance.
The difference of 0.3 in AUC was obtained between the proposed method and the five best methods of the challenge. We attribute this difference to the effectiveness of the deep learning methods, these methods which never fail to give good results in medical field. Also to the strategy of the balancing that we have used.

After the challenge we have proposed the modified SMOTE algorithm (see section 4.2.3) for balancing the training dataset and we have used Random forest classifier instead of Euclidian distance in the final version of the method. This challenge was a good experience for us, the modification that we brought to our method was a consequence from the result obtained in the challenge.

4.6 Conclusion

In this chapter, we have tackled the problem of breast tissue classification, while considering the problem of non-equilibrated dataset.

The first contribution is related to the breast tissue classification. We have modeled the images according to their tissue densities correlation. We have also demonstrated the successful application of textons distribution for the two classes as well as multiclasses breast tissue classification.

We also presented the evaluation of our initial version of the method allowing to predict the probability that a patient can develop cancers within the Digital Mammography DREAM Challenge, what generated the second contribution. In which we have addressed to the equilibration issue by proposing an improved version of the SMOTE approach, the latter has shown a great efficiency.

We have also proved that the use of a balanced dataset improves the results of classification.

Chapter 5

Histopathological image classification

5.1 Introduction

Breast cancer diagnosis pass though the step of detection by using mammography or ultrasound imaging, in the case of cancer detection, the diagnosis is then followed by breast tissue biopsy.

In the part of breast cancer diagnosis, in this thesis, we wanted to give an integrated methods to aid the diagnostic of breast cancer. In which, in the precedent chapter, we concentrated on breast density classification that is one of the criterion used by radiologist to diagnosis breast cancer. As is known, the histopathological analysis is the main reference to determine the existence of breast cancer, this makes histopathological analysis very important task in the breast cancer diagnostic.
Thence, We had to study the histopathological images, indeed the presented work in this chapter is based on the use of the most recent artificial intelligence methods that are deep learning, to classify breast cancer histology images.

The next section is dedicate to give a general overview on deep learning methods, then we present the proposed method for breast cancer classification using histopathological images, after that we will give it evaluation on International Conference on Image Analysis and Recognition (ICIAR) Grand Challenge on **B**re**A**st **C**ancer **H**istology image (BACH) followed by discussion section.

5.2 Deep learning

Since the beginning of computer development, the Artificial Intelligence (AI) theme was considered as one of the exclusive subject in computer science. In fact, in 1950 Alan Turing [266] discussed how to build intelligent machines that can simulate human reasoning and how can be able to do intelligent things, Alan Turing proposed the Turing Test to test machines intelligence [1].

[1] Machines were capable of thinking, if it were able to make small talk with another human and understand the context of the conversation.

The main objective of AI is to provide a set of algorithms that can be used to solve problems that humans perform intuitively, but are otherwise very challenging for machines. Artificial neural network (ANN) methods are a subfield of artificial intelligence. In which, they were inspired by the neural connections in our nervous system, to imitate the human reasoning. As it was described by Soni [267], the word "neural" is the adjective form of "neuron", and "network" denotes a graph-like structure; therefore, "Artificial Neural Network". ANN has gone through different incarnations since 1943, knowing today by deep learning methods.
In the following section we will introduce the fundamentals notions of ANN followed by the basics concept of deep learning methods.

5.2.1 Neural Networks Fundamentals

The researches in neurocomputing started early, in 1943 the neuroscientist Warren MuCulloch and the logician Walter Pitts, published the paper *"A logical calculus of the ideas immanent in nervous activity"*, in which they proposed the first artificial neuron allowing to compute arithmetic and logical functions [268].
In addition, the book *"The Computer and the Brain"* of John von Neumann [269], published in 1958 one year after his death, contribute to pave the way for neurocomputing development.
The next paragraph, we will introduce the anatomy and physiology of biological neurons, then the analogy of the biological neuron with the artificial neuron is presented in the Artificial Neural Networks paragraph. Finally, we will end this section by given the historical passage of ANNs methods towards deep learning methods.

A. *Biological neurons*

   Our brains are composed of billion of neurons, each connected to about 10,000 other neurons. The neuron contain three principals units: cell body (called also soma), dendrites, axon and synapses cells (see the Figure 5.1).

   The dendrites and axon connect the neuron to other neurons. In fact, the axon receives the impulsion, in the form of an electric signal, from the cell body and carries them away to the dendrites of neighboring neuron by using the synapses cells (situated at the end of the axon) that allow to make connection between two neurons. The neuron can be either activates or not, this means that neuron activation is a binary operation. If these electrical inputs are sufficiently powerful to fire the neuron, then the neuron activates and transmits the signal along its axon, passing it along to the dendrites of other neurons. Thus allow to continuing the process of passing the message along.

B. *Artificial Neural Networks*

   The artificial neural networks is represented as a directed graph containing a set of nodes and a set of connections. The node receives inputs signal as stimuli from other nodes in the graph, it compute a simple linear threshold function and transmits the output signal forward to another node only when the signal is stronger than the node's

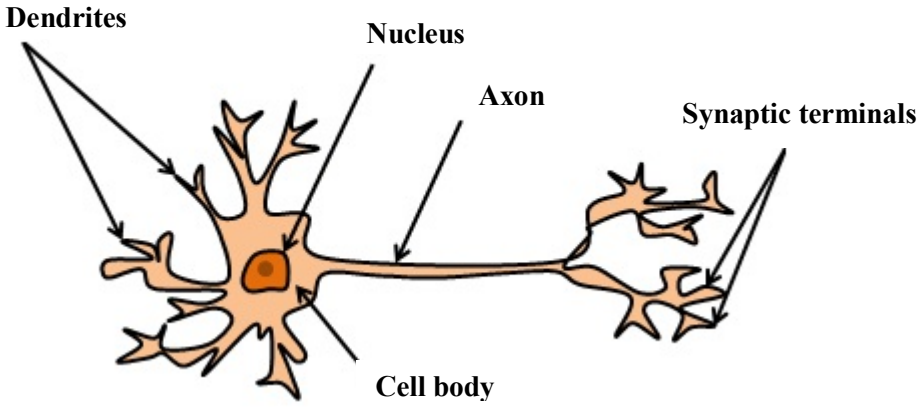

Figure 5.1: Anatomy of a neuron

threshold limit (also called bias b), the resulting signal is labeled by a weight allowing to precise the extent to which the signal is amplified (w>0) or diminished (w<0).

The analogy of the biological neuron and the artificial neuron is that the axons and dendrites represent by the connections between nodes, the synapses represent the connection weights, and the activity in the soma approximates node's computation. According to Zupan and Gasteiger [270], Both the biological network and ANN learn. We can see in the Figure 20, that the Net input is computed as the inner product of the input signals (x_i) impinging on the neuron and their strengths (w_i). For n signals, the activation function is expressed as:

$$y = \begin{cases} 1, if \sum_{i=1}^{n} w_i x_i \geq b \\ 0, if \sum_{i=1}^{n} w_i x_i < b \end{cases} \tag{5.1}$$

1 indicate "ON" and 0 indicate "OFF".

C. *The Perceptron Algorithm*

The neural network proposed by McCulloch and Pitts know also by linear threshold gate was a binary model, In which its input and output are binary values. This neural network can do only a binary classification.

In the linear threshold gate the weight values are (0,1) or (-1,1) and the output Y of the model is computed as following:

$$Y = f(\sum_{i=1}^{n} x_i * w_i) \tag{5.2}$$

Where f is a linear step function at threshold T. Although McCulloch and Pitts proposed a formal model, yet, the linear threshold gate was limited by using a manual values of the weight and threshold.

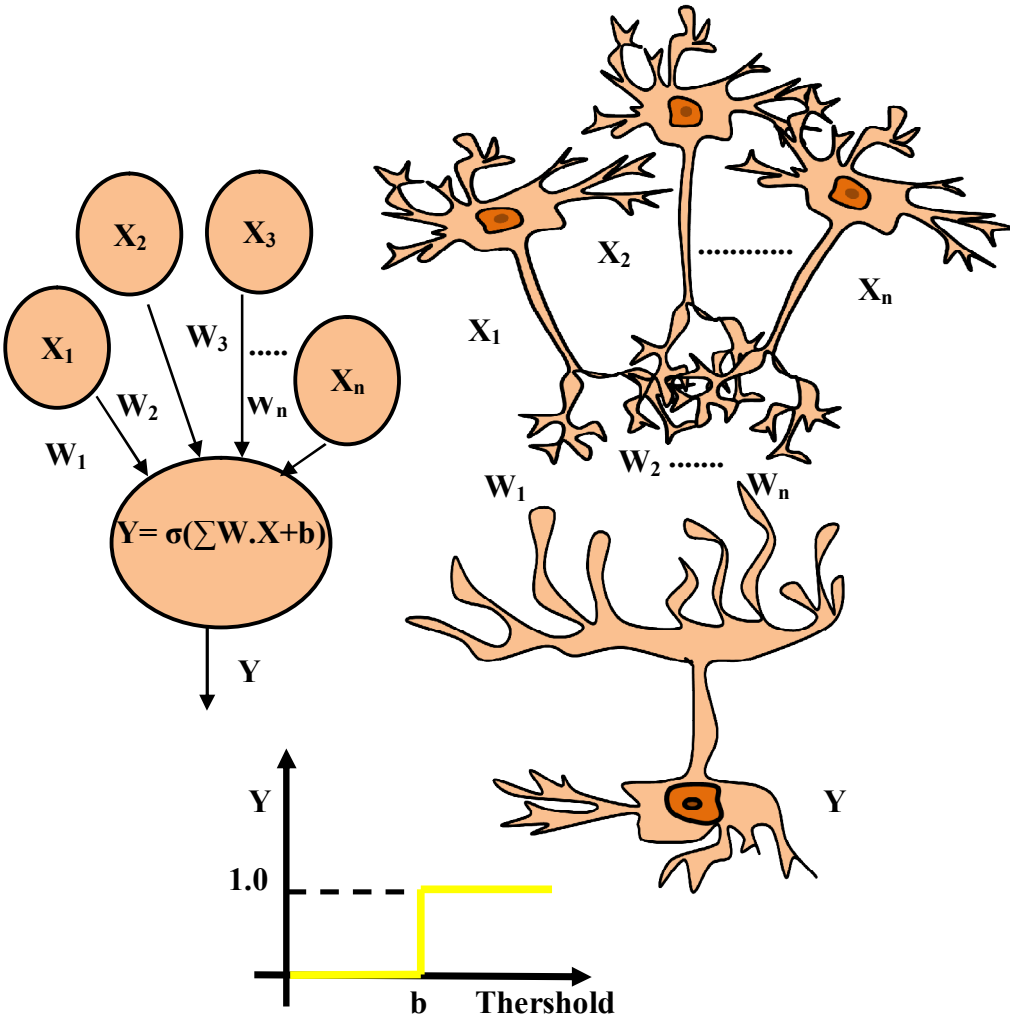

Figure 5.2: Biological and artificial neuron in interaction with other neurons

More flexible model called Perceptron, was proposed by the American psychologist Frank Rosenblatt in his article *"A Probabilistic Model for Information Storage and Organization in the Brain* [271] in 1958. This model could automatically learn the weights by using Hebbian learning rule of adjusting weights that are required to classify an input. The single layer perceptron proposed by Rosenblatt was the simplest type of artificial neural networks that can only classify linearly separable cases, based on a threshold function

$$Y = f(\sum_{i=1}^{n} x_i * w_i) + b) \tag{5.3}$$

Where b represents the threshold (bias) value.

The improvements given Rosenblatt, made perceptron researches, at this era, more attracted by the scientific community.

However, the book of Minsky and Papert *"Perceptrons: an introduction to computational geometry* [272] in 1969, contribute to unveiled the limitation of the perceptron, by demonstrating that the perceptron can't separate nonlinear data points.

This publication caused a stunted growth of neural network researches where they stagnated for nearly a decade.

The illuminated year of ANNs was in 1986, in which Rumelhart et al. [273] introduce in their paper *"Learning representations by back-propagating errors"* a new learning procedure of ANN by using back-propagation algorithm.

The back-propagation algorithm enabled multi-layer ANN to learn nonlinear functions and solve nonlinear problems (like XOR) by using nonlinear activation functions.

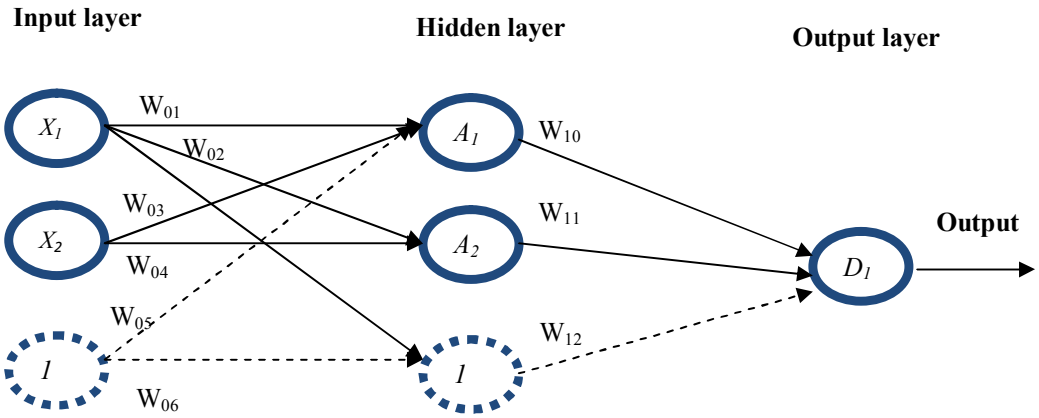

Figure 5.3: Neural Mode with one hidden layer

The back-propagation

The back-propagation was introduced in 1960 by the professor of Aerospace Henry J.Kelley [274] in his paper *" Gradient Theory of Optimal Flight Paths"*.

In 1962 , Stuart Dreyfus [275] proposed in the article *"The numerical solution of variational problems"* a simplification of back-propagation computation from dynamic programming to the chain rule.

In 1970, Seppo Linnainmaa [276], introduced the automatic differentiation (AD) method that compute the derivative of a differentiable composite function for backpropagation algorithm and he implements the computer code. Since the integration of the back-propagation in learning process of ANN by Rumelhart et al. [273] in 1986, Back-propagation algorithm represent one of the cornerstone in ANN. This algorithm is composed of two steps:

1. ***The forward pass:*** inputs are passed through the network and the output predictions are obtained.
2. ***The backward pass:*** the gradient of the loss function at the final layer is computed and it use to recursively apply the chain rule to update the weights in the network.

D. *From ANN to deep learning*

In 1971, the Ukrainian Alexey Grigoryevich Ivakhnenko [277] used the methods of inductive statistical learning known by Group Method of Data Handling (GMDH) to creates 8-layer Deep neural network. Where in each layer, they selected the best features through a polynomial activation functions and forwarded them to the next layer. 9 years after, the Japanese computer scientist Kunihiko Fukushima [278] proposed the first convolutional neural network architecture which could recognize visual patterns named Neocognitron in 1980. In Kunihiko Fukushima's paper [278] *"Neocognitron: A Self-organizing Neural Network Model for a Mechanism of Pattern Recognition Unaffected by Shift in Position"*; he introduce the convolutional and pooling layers that still used until today. Neocognitron was trained by using a reinforcement scheme. In 1989, Yann LeCun [279] used backpropagation to train convolutional neural network to classify handwritten digits; his model was the cornerstone of the modern computer vision foundation. Yann LeCun 's system was used to read handwritten checks in the United States.

A new problem appeared in the growth road way of deep learning methods, discovered by Sepp Hochreiter in 1991 [280], is the vanishing gradient which can make the learning of a big deep neural network methods almost impractical. In fact, the early layers could not be learned because the learning signal can't reach these layers.

Two solutions where proposed for this issue. The first one, proposed by Schmidhuber in 1992 [281], use a pretraining approaches that were developed for recurrent neural networks (RNN); in these approaches the weights layers are initialized in unsupervised learning layer-by-layer; which implies that the weights in early layers only need a slightly adjustment during supervised learning to achieve good results.

The second solution proposed by Sepp Hochreiter and Jürgen Schmidhuber in 1997 [282] is the approach of long short-term memory (LSTM). In 2008, a new idea contribute to the advancement of deep neural networks is the used of GPUs for training and testing. Given by Andrew NG's group in Stanford university. The use of GPUs allowed deep neural networks to train efficiently on huge volume of data. The most important solution of the vanishing gradient problem, was introduced by Glorot et al. in 2011 [283] in their paper "Deep Sparse Rectifier Neural Networks" is the use of Rectified Linear Unit layer (ReLU) activation function.

The deep learning boom globally was in the ImageNet Large Scale Visual Recognition Challenge (ILSVRC 2012). Where Alex Krizhevsky et al. [284] proposed AlexNet with a GPU implementation, that won the challenge with a huge jump over the other methods. Since 2012, the researches in deep learning accelerated rapidly, where many startups and research teams are created and supported by great companies and universities.

5.3 Convolutional Neural Networks (ConvNets/CNNs)

A Convolutional Neural Network (CNN) is a Deep Learning algorithm that used to recognize visual patterns directly from pixel images. ConvNet represent one of the advancements methods in Computer Vision.

The Neocognitron, proposed by Fukushima in 1980 [278] was one of the first CNN that recognize visual patterns such as handwritten characters.

Few years later, LeCuN et al. [285] proposed an improved version of his ConvNet architecture [286] called LeNet used to classify characters in a document.

The cornerstone of CNN is the convolution. The convolution is a mathematical operation on two functions that measure the overlap as they interact; this operation allows the CNN to learn the filters that are used to extract the features of the image.

The automatic features process make CNN most used and advanced compared to other computer vision methods, where the features are hand-engineered.

5.3.1 Convolutional Neural Network principle

ConvNet are based on the concept of artificial ANNs, where they are made up of neurons that have learnable weights and biases. However unlike the fully connected (FC) layers used in neural networks where each neuron in the input layer is connected to every output neuron in the next layer. The CNN use FC only at the last layers. Another difference point is that ConvNet receive an image as input.

The CNN extract the features of the image by assign the importance of learnable weights to salient objects be able to classify the images. Figure 5.4 shows a general schema of a ConvNet.

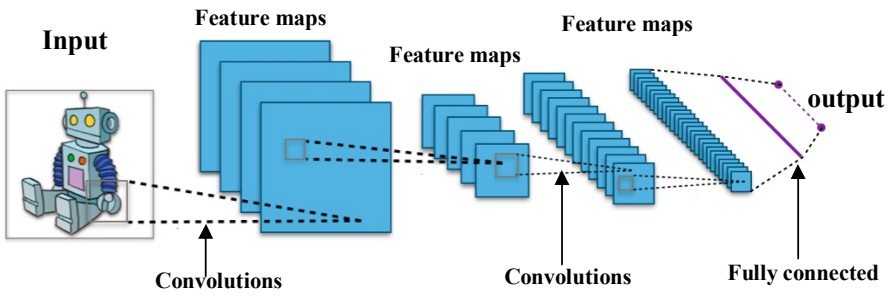

Figure 5.4: Convolutional Neural Networks schema

5.3.2 Layer types in Convolutional Neural Network

ConvNet is a sequence of layers, that are arranged in a 3D volume: width, height, and depth. In the first layer, the depth is equal to the number of image channels usually 3 (RGB), in more advanced layers the depth is equal to the number of filters applied.
Each layer transforms one volume of activations to another through a differentiable function. There are many layer types used to build CNNs, the most used are:
Convolutional (CONV)
Rectified Linear Unit layer (RELU)
Pooling (POOL)
Fully-connected (FC)
Batch normalization (BN)
Dropout (DO)
The next paragraph we describe each layer type separately.

- **Convolutional layer**: computes the convolution between the filters (whose parameters need to be learned) and the local regions of the input that are connected to them.

- **Rectified Linear Unit layer**: this layer applies an activation function to the input of the layer, thresholding at zero like max (0,x). It allows to add non-linearity to the network making him more generalized.

- **Pooling layer**: this layer applies downsampling operation along the width and the height of layer's volume. It represent a method to reduce the size of an input and it is common to insert pooling layer between consecutive convolution layers [287].

- **Fully-connected (FC) layer**: in this layer all activation are fully connected to the previous layers. It always placed at the end of the network. It's common to use one or two FC layers prior to applying the softmax classifier [287].

- **Batch normalization (BN) layer**: this layer normalize the given input volume before passing it into the next layer in the network.

- **Dropout (DO) layer**: this is a regularization layer, which it randomly disconnect inputs from the preceding layer with a probability p, this allow to prevent overfitting.

From all the above layers types, the CONV, FC and BN are the only layers that contain parameters that are learned during the training process. Pooling layers have an impact on the spatial dimensions of an image as it moves through a CNN.

5.3.3 The CNNs architectures

In this section, we will present the first ones CNNs such as LeNet-5 and AlexNet, then we will give a general overview of the CNNs architectures that have been pretrained on ImageNet dataset and shared by Keras deep learning librarie, then we finish by introducing the two recent CNNs.
We refer the readers interested to the CNNs schema to see the Appendix.

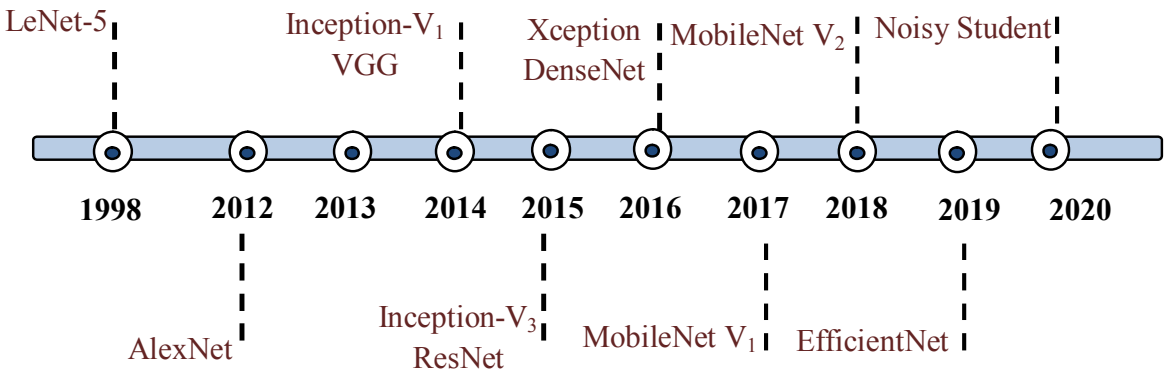

Figure 5.5: Timing Diagram of CNNs development

A. *LeNet-5*

The LeNet developed by LeCun [285] for Optical Character Recognition is a small and simple architectures. This architecture contain: 2 convolutional layers, 2 The average-pooling layers and 3 fully-connected layers. Du to it straightforward composition, LeNet represent the starting point to teach the CNNs concepts.

B. *AlexNet*

Developed by Krizhevsky member of the Geoffrey Hinton's group [284]. This architecture won the 2012 ImageNet classification challenge with a huge difference compared to the other methods; that was contribute to make the deep learning approach in the shine era. AlexNet contain 5 convolutional layers with Rectified Linear Units (ReLUs) as activation functions, 3 max pooling layers and 3 fully-connected layers.

C. *VGG*

The Visual Geometry Group (VGG) of Oxford university [288] developed VGG architecture of 16 layers (VGG-16) and 19 layers (VGG-19). The aim of the group was to make up a deeper networks by using successive convolution layers that used only small filters of size (3×3). VGG-16 has 13 convolutional and 3 fully-connected layers. VGG-19 has 16 convolutional and 3 fully-connected layers.

D. *Inception-v1(GoogleNet)*

It was developed by Christian Szegedy et al. [289] a team at Google. The team design an architecture that are depth but it keep the computation constant. Where they used stack modules called *"Inception module"* instead of stacking convolutional layers, the architecture contains also two auxiliary classifiers. The Inception module contain different filters of size 1×1, 3×3, 5×5 to captures different features, followed by filter Concat that allows to concatenate the filters results. The filters with size 1×1 is used to reduce the dimensionality. The auxiliary classifiers are used in the training process to keep the gradient signal propagated back. In total, Inception-1 architecture contained 22 layer but with only 4 million parameters compared to 60 million parameters in AlexNet.

E. *Inception-v3*

Christian Szegedy et al. [290] proposed two improved version of Inception-v1 named Inception-v2, Inception-v3. The main hallmark in Inception-v2 is to scale up networks by adding factorized convolutions while using an efficient computation. In fact, they factorising n×n convolutions into asymmetric convolutions: 1×n and n×1 convolutions, and 5×5 convolution is factorised to two 3×3 convolution operations. This version also tackled the problem of the representational bottleneck (it manifest by the dimensions reduction of the input that drastically cause loss of information), by using an efficient grid size reduction, where the filter banks were made wider instead of deeper. In addition to the factorized 7x7 convolutions, the regularization solution were introduced in Inception-v3 includes: RMSProp optimizer, batch normalisation in the auxillary classifiers.

F. *ResNet*

The above architectures are based on the increasing number of layers to have a good precision, however this can conduct to the standard problem of vanishing gradient that make the accuracy saturated. He et al. [291] from Microsoft treated this problems by designing ResNet architecture that use skip connections (named also residuals). In fact, ResNet avoid the training difficulty of deeper neural networks making them more depth and less complex. In the traditional connection between layers in CNNs, each layers is connected to its previous, obverse to this, the skip connections allows the layer to be connected to layers behind the previous layer.

G. *Xception*

François Chollet from Google [292] proposed eXtreme Inception architecture named Xception architecture, where Inception modules have been replaced with modified depthwise separable convolutions.

Depthwise separable convolutions was introduced by Laurent Sifre in 2014 [293]. Is a depthwise convolution followed by a pointwise convolution. Depthwise convolution

is the channel-wise convolution, and pointwise convolution is 1×1 convolution. Depthwise separable convolutions help to reduce the computational complexity. Xception architecture used pointwise convolution followed by a depthwise convolution. This modification is inspired from the inception module. In fact, the Inception module consists to independently look at cross-channel correlations and spatial correlations. Where, the cross-channel correlations are captured by 1×1 convolutions, then the spatial correlations within each channel are captured with convolutions of 3×3 and 5×5 [290]. So, Xception perform 1×1 convolution to every channel, then it perform a 3×3 convolution to each output. That represent a linear stack of depthwise separable convolution layers, Xception contain also a residual connections.

H. *DenseNet*

The Dense Convolutional Network (DenseNet), introduce by Huang et al. [294] is based on the idea of skip connection used in ResNet, yet it connects each layer to every other layer in the network, this kind of connection is named Dense connectivity. DenseNets minimize the vanishing-gradient problem, and strengthen propagation and reuse features. In Densely Connected Convolutional Networks paper of Huang et al. [294] introduce DenseNet-121, DenseNet-169, DenseNet-201 and DenseNet-264. Where each architecture is composed of Dense Block and Transition Layer.

I. *MobileNet-v1*

Developed by Howard et al. [295] from Google, MobileNets is a light architecture that is designated to mobile and embedded vision applications. Its lightness is related to the use of depthwise separable convolutions instead of full convolution.
Two hyper-parameters are introduced in MobileNet, that make this architecture more flexible, these parameters are Width Multiplier ” α” and Resolution Multiplier ”ρ”.
The role of α is to thin a network uniformly at each layer, where the number of input channels M becomes αM and the number of output channels N becomes αN.
ρ is used to set the input resolution, where $\rho \in (0, 1]$ that can make the input resolution of the network 224, 192, 160 or 128 [295].

J. *MobileNet-v2*

Sandler et al. [296] introduce the second version of MobileNet by proposing a new module to overcome the drawback of MobileNet-v1. The idea of MobileNet-v1 was to find tradeoff between performance and computation. So the expensive full convolutions were replaced with the cheaper depthwise separable convolutions, thus resulting a low-dimension tensors that conduct to reduce the number of computations. Nevertheless, when a convolution is applied to low-dimensional tensor, it won’t be able to extract a lot of information. Hence, the invented of the bottleneck residual block module. This module first expanded the input to high dimension then it used

depthwise convolution to extract the features, finally it apply a linear convolution to project the features to a low dimensional space, whence name bottleneck. In this module there is also residual connection. Figure 5.6 show an illustration of this module.

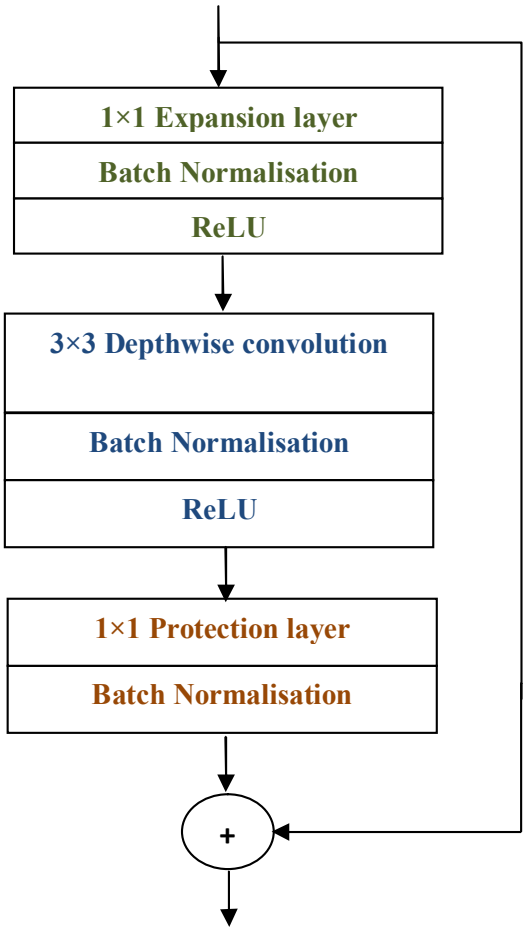

Figure 5.6: Mobile inverted bottleneck

K. *EfficientNet*

In the state-of-the-art CNNs development, scaling the architectures by increasing depth, with or image resolution was a conventional practice to improve model accuracy. However such CNNs scale up method using the three dimensions simultaneous was not defined before the work of Tan and Le [297] in 2019.

In fact, the authors define a new scaling method to scale up CNNs in order to improve model performance. In this method the authors used compound coefficient φ to uniformly scale the hyper parameters include depth, width and resolution (depth: $d = \alpha^{\phi}$, width: $w = \beta^{\phi}$, resolution: $r = \gamma^{\phi}$). α, β and γ are constants determined by a small grid search with the constraint that $\alpha\,\beta^2 \cdot \gamma^2 \approx 2$. The authors also introduce a new CNN called EfficientNet, this architecture is composed of mobile inverted bottleneck (MBConv).

L. *Noisy Student*

In 2020, Noisy Student was introduced by Xie et al. [298] of Google research team. This architecture is based on the concept of semi supervised Learning, where unlabeled images are used to improve the ImageNet accuracy.

The authors used two EfficientNet models, one is considered as teacher and the second as student. First, the teacher is training on ImageNet images, then is used to predict pseudo labels on 300M unlabeled images. It pursue by the EfficientNet student training on both dataset (ImageNet and 300M pseudo labeled images given by the teacher). This two steps are iterate a few times by treating the student as a teacher to relabel the unlabeled data.

The authors used the name Noisy Student, because in the process of student learning they used input noise and model noise by using dropout, data augmentation and stochastic depth, this to push the generalization of the student.

In the next section we will present the CNNs chosen in our method for the histopathological images classification.

5.4 Method

We propose a classification method based on a consensus oriented by three convolutional neural network architectures (CNNs): InceptionV3, ResNet50 and MobileNet.
The consensus is giving by Hard Voting as described in Figure 5.7. Hard voting is the simplest case of majority voting. Here, we predict the class label ŷ via majority (plurality) voting of each CNN C_j:

$$y = mode\{C_1(x), C_2(x), ..., C_m(x)\} \tag{5.4}$$

Assuming that we combine three CNNs that classify a training sample as follows:
• CNN C1 -> class 2
• CNN C2 -> class 2
• CNN C3 -> class 1

$$y = mode\{2, 2, 1\} = 2 \tag{5.5}$$

Via majority vote, we classify the sample as ”class 2.”

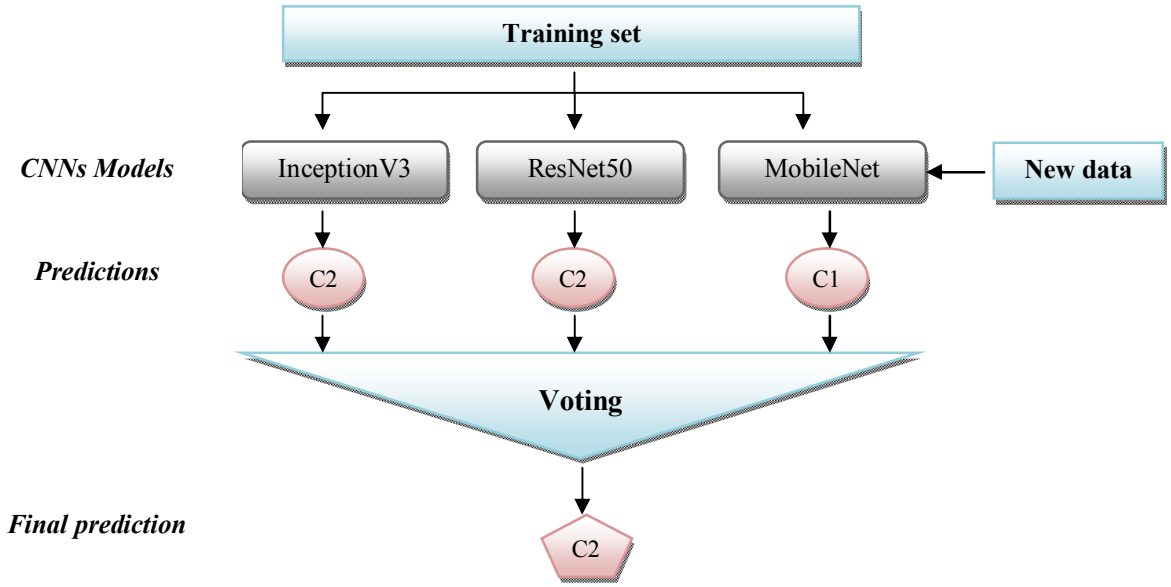

Figure 5.7: The steps of the propose approach

5.5 Experimental results

5.5.1 Dataset

Taking into account the large number of images in BreakHis dataset [5] and it availability, we have chosen it for the evaluations.

The BreaKHis database contains microscopic biopsy images of benign and malignant breast tumors. Samples are generated from breast tissue biopsy slides, stained with Hematoxylin and Eosin (H&E).

H&E is one of the principal stains in histology, the hematoxylin stains cell nuclei into blue, and Eosin stains cytoplasm, connective tissue and other extracellular substances into red or pink.

The database is composed of 7909 images divided into benign and malignant tumors. This dataset provides five training-testing splits, with each split using 70% of images for training and 30% for testing [5].

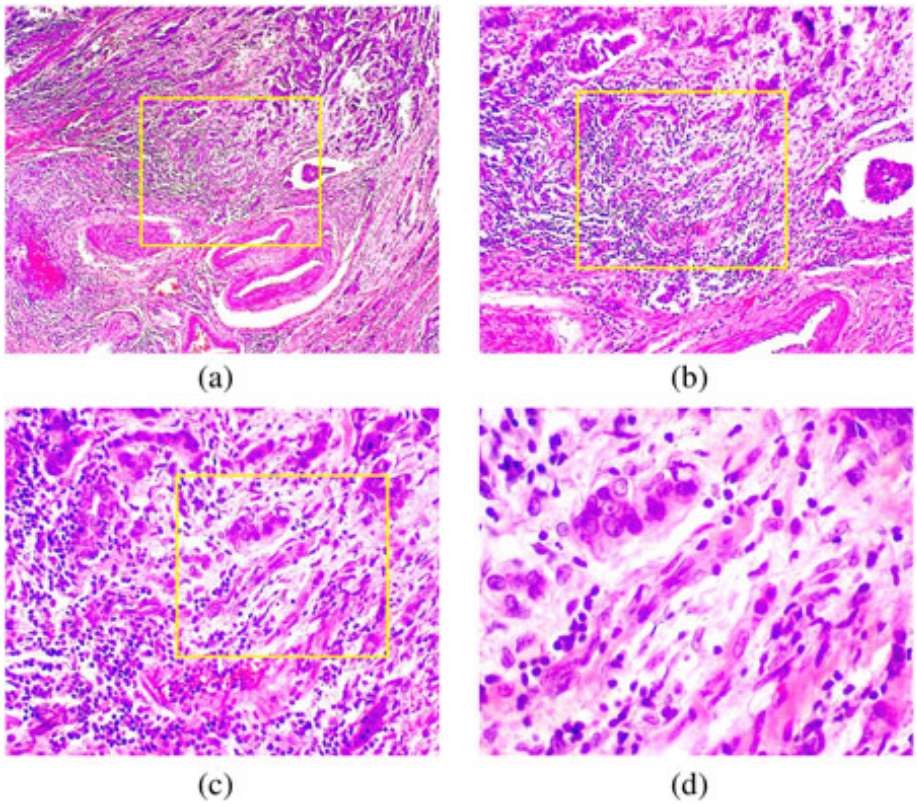

Figure 5.8: Slide of breast malignant tumor (stained with HE) seen in different magnification factors: (a) 40×, (b) 100×, (c) 200×, and (d) 400× [5].

5.5.2 Results

First we have tested each CNN architecture separately, we notice that all CNNs are initialized with the pre-trained imageNet weights. And we have retraining all the network using 30 epochs. The measures considered for the evaluation of the experiments are performed on the basis of accuracy at image level and patient level as was used in [195].
Let:
N_p be the number of total patients
N_{rp} are the images correctly classified
N_{np} be the number of cancer images of patient P
Patient score can be defined as:

$$Patient\_Score = \frac{N_{rp}}{N_{np}} \tag{5.6}$$

Then the global patient recognition rate is:

$$Patient\_Accuracy = \frac{\sum Patient\_Score}{N_p} \tag{5.7}$$

Second, we evaluated the recognition rate at the image level.
Let:
N_r are the histopathological images correctly classified
N_{all} be the number of cancer images of testing set
The recognition rate at the image level is:

$$Image\_Accuracy = \frac{N_r}{N_{all}} \tag{5.8}$$

Figure 5.9 and Figure 5.10 show the accuracy result of InceptionV3, MobileNet and ResNet50.
MobileNet outperform the two other CNNs at patient level and in the majority magnifications at image level.
On the other hand, to select the good combination of CNNs a set of experiment are conducted, we remark that the combination of all CNNs give the best results as shown in Figure 5.11 and Figure 5.12.

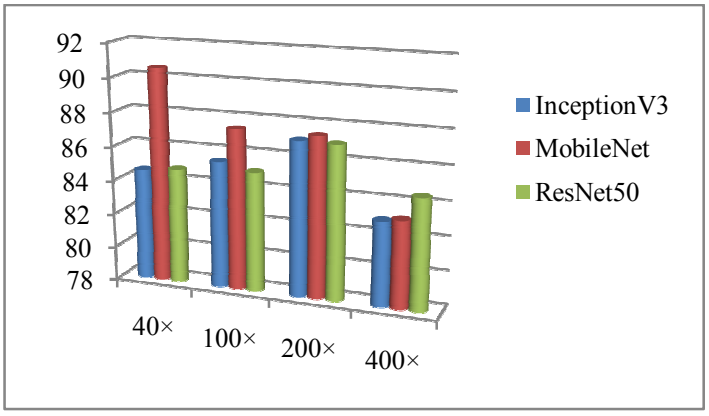

Figure 5.9: The accuracy at image level

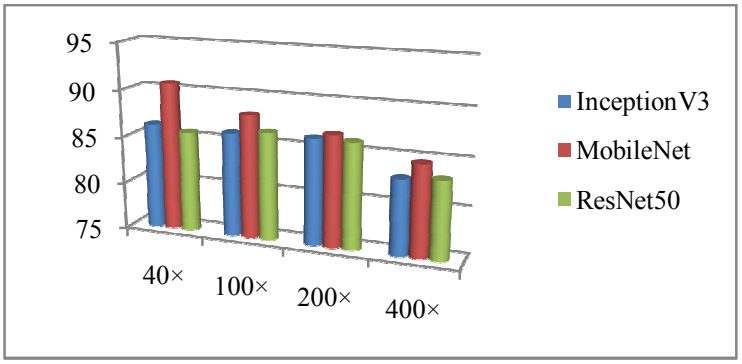

Figure 5.10: The accuracy at patient level

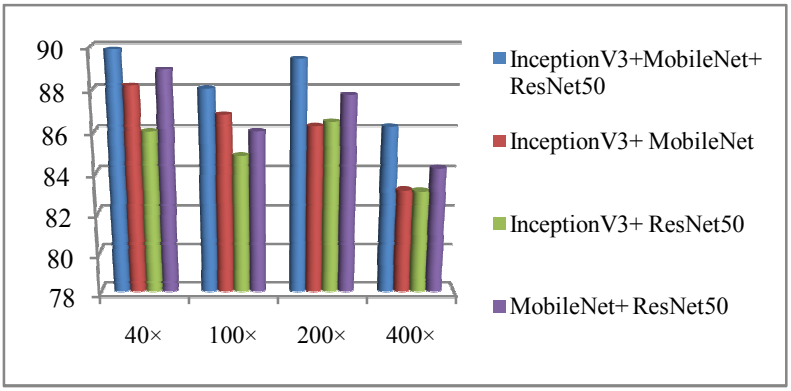

Figure 5.11: The accuracy given at image level for the four combinations

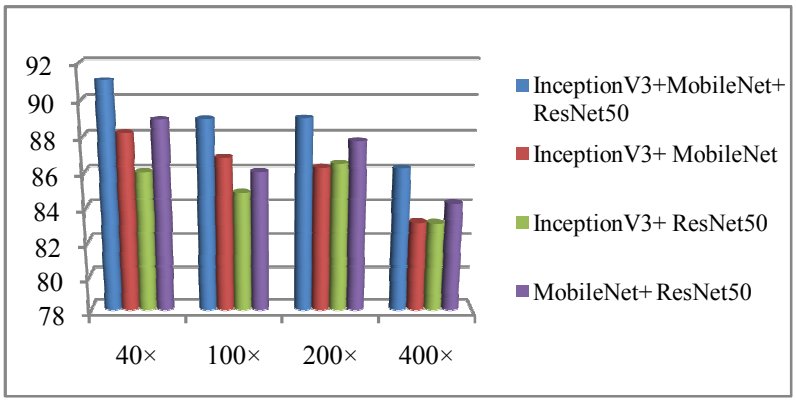

Figure 5.12: The accuracy given at patient level for the four combinations

5.5.3 Comparative study of related works

In this section, we make a comparison with related works given in the state of the art chapter (section 2.4). Table 5.1 summarizes the methods and their accuracies.

Authors	**Methods**	**Image level**					**Patient level**				
		Magnification				**AVG**	**Magnification**				**AVG**
		40×	**100×**	**200×**	**400×**		**40×**	**100×**	**200×**	**400×**	
Spanhol et al. [5]	PFTAS+ QDA	-	-	-	-	-	83.8	82.1	84.2	82	**83.02**
Spanhol et al. [195]	Proposed CNN	89.65	85.0	82.8	80.2	**84.4**	88.6	84.5	83.3	81.7	**84.52**
Spanhol et al. [195]	Combining multi classifier	85.6	83.5	82.7	80.7	**83.12**	90.0	88.4	84.6	86.1	**87.27**
Spanhol et al. [192]	Deep features	84.6	84.8	84.2	81.6	**83.8**	84.0	83.9	86.3	82.1	**84.07**
Benhammou et al. [205]	Inception V3	86.5	83.2	85.4	80.3	**83.85**	87.6	82.4	86.1	79.7	**83.95**
Bayramoglu et al. [196]	CNN using multi magnification	-	-	-	-	-	83.08	83.17	84.63	82.10	**83.24**
Sun and Binder [197]	Google LeNet	87.59	85.67	89.86	84.12	**86.81**	-	-	-	-	-
Song et al. [198]	Fisher Vector +VGG model	87.0	86.2	85.2	82.9	**85.32**	90.0	88.9	86.9	86.3	**88.02**
Song et al. [206]	Fisher Vector +VGG19+ Component Selective Encoding	87.5	88.6	85.5	85.0	**86.65**	88.5	90.8	89.2	89.2	**89.42**
Sanchez-Morillo et al. [207]	KAZE Features	85.9	80.4	78.1	71.1	**78.87**	86.4	81.6	77.8	72.9	**79.67**
Han et al. [199]	CSDCNN With the modification of the loss function	95.8	96.9	96.7	94.9	**96.07**	97.1	95.7	96.5	95.7	**96.25**
Al Nahid et al. [210]	CNN+Mean shift	90	85	91	90	**89**	-	-	-	-	-

Samah et al. [175]	Pyramid-structure Wavelet	-	-	-	85.62	**85.62**	-	-	-	-	-
Nejad et al. [200]	Proosed CNN	77.5	-	-	-	**77.5**	-	-	-	-	-
Sharma et al. [201]	PFTAS+ RF	81.7	81.2	80.7	81.5	**81.27**	-	-	-	-	-
Sudharshan et al. [211]	MIL+CNN	87.8	85.6	80.8	82.9	**84.27**	92.1	89.1	87.2	82.7	**87.77**
Zhi et al. [202]	Proposed CNN	91.28	91.45	88.57	84.58	**88.97**	-	-	-	-	-
Kumar and Rao [208]	Proosed CNN	82	86.2	84.6	84	**84.2**	83	81	84.2	81	**81.66**
Cascianelli et al. [203]	VGG+ Reduction strategies	84	88.2	87	81.2	**81.27**	-	-	-	-	-
Alirezazadeh et al. [209]	Adapation+ PFTAS+ QDA	-	-	-	-	-	89.1	87.3	88.4	86.6	**87.85**
Nejad et al. [204]	VGG+SVM	80				**80**	-	-	-	-	-
Zhu et al. [212]	Hybrid CNN	85.7	84.2	84.9	80.1	**83.72**	85.2	83.5	84.1	79.3	**83.02**
Nedjar et al. [299]	Inceptionv3+ ResNet-50+ MobileNet	89.87	88.05	89.42	86.23	**88.39**	91.06	88.96	89.01	86.21	**88.81**

Table 5.1: Accuracy comparison of the proposed method with studies in literature

Different approaches were developed and tested to predict malignant breast tumor from histopathological images.

We can classify these approaches according to three propositions:

• The use of Hand craft features versus CNNs approaches

• The use of patches versus images as input to the CNN

• The use of Single CNN versus multiple CNNs

We start by the first proposition, the works based on the traditional approaches using the hand craft features with machine learning are [5] [207] [175] [201] obtained less accuracy compared to the works based on CNN methods [195] [197] [206] [199].

The strategy used by Alirezazadeh et al. [209] that used an adaptation method to overcome the variance of hand craft features in the histopathological images achieved a remarkable performance compared to the traditional approaches.

In other hand, the single layer CNN proposed by Nejad et al. [200] proved that a CNN with just one hidden layer can gave a result that exceed 70%. This is due to that the hand craft features are very hard to define, because they were selected based on domain specific knowledge, however, the CNN beat this problem by making the computer able to learn the salient features.

Secondly, the use of patches or images as input to the CNN have an impact on prediction, among the works that used the patch, we quote the works of [195] [202]. The statistical analysis given Spanhol et al. [195] showed that the biggest size of patch gave a good prediction, this result strengthens the idea of Sun and Binder [197] which they sad *"The large size of image we use for training, the better performance we get"*. They augmented their saying by the fact that the tumor descriptor that discriminate between malignant and benignant should be extracted from a large number of nuclei.

In other hand, the authors that used the patches as input to the CNN justify their chose to the relevant nuclei features (color and shape) that can be captured using a small regions of interest to differentiate between tumors type.

In our proposed method we have used the full size of images. We found that the images contain mixed region with malignant, benignant and normal tissue, as the dataset contain the annotation only at the image level, the extracted patches will receive the class of the image, this can cause problem. Given a malignant image when a patch is extracted from this image and it contain only the normal tissue, it will be considered as malignant because it belong to malignant image.

A compromised solution was proposed recently by Zhu et al. [212] which they used both concepts of the full image and the patches by using two separately branch in the CNN. This approach allows to get all tissue structure information from the nuclei features to the organization of several nuclei in the tissue.

However, even if the CNN capture the full image information, the obtained results were less compared to the methods that used the full image. In fact, from the best four methods at the image level accuracy three of them, were used the full image as input to the CNN [199] [210] [299]. As well, at the patient level accuracy the best four methods used the full image [199] [206] [299] and [198]. The method of Han et al. [199] outperform all the presented methods, where they proposed a new loss function that take into account the relation of the intra-class and inter-class instances, this function allows the model to be more general. In addition, we remark that only the method proposed by Han et al. [199] and our method [299], are in the four best results both at image level and patient level.

Finally, from the CNNs approaches we distingue the works that used single CNN [205] [206] [208] against three works based on combined CNNs [195] [212] and our proposed method.

The combined methods were based on different ideas, Spanhol et al. [195] used four CNNs trained on different patches size, their idea was to get image class prediction using different

parts information of a given image. The second method proposed by Zhu et al. [212] used the bagging combination approach to reinforce the generalization of their model, where the same model are duplicated and trained with different data and the final result is obtained by using the vote.
In the model that we have proposed, we combine three different model namely InceptionV3, ResNet50 and MobileNet. Our supposition is based on the fact that each CNN have it capacity and methodology to extract the salient features from the image. The goal was to give a confidant prediction score based on all different features. For this, we have applied the vote on the final prediction given by each CNN.
As the three combination used different strategies to improve the accuracy, the proposed strategy overcome the two previous method on the accuracy at the image level with a gap around 5%, where we got 88.39% compared to 83.12% and 83.72% given by [195] and [212]. At the patient level, we obtained 88.81% compared to 87.27% [195] and 83.02% [212].
The presented comparison was based on BreaKhis dataset. In order to validate the proposed approach on another dataset, we have participated to BACH challenge 2018. We will give more detail about it in the next section.

5.6 BACH challenge

5.6.1 Objective of the challenge

The ICIAR 2018 Grand Challenge on BreAst Cancer Histology image (BACH) was composed of two mains goals. The part A of the challenge consists of automatically classifying Haemotoxylin and Eosin (H&E) stained breast histology microscopy images in four classes: normal, benign, in situ carcinoma and invasive carcinoma. The part B consists of performing pixel-wise labelling of whole-slide images in the same four classes [11].

We participated to the part A of the challenge, where the participants were asked to submit CSV file containing the class prediction of all images in the test dataset, the assigning prediction can be 0 , 1, 2 or 3 for Normal, Benign, in situ and Invasive, respectively.

5.6.2 Dataset

The dataset was composed of Hematoxylin and eosin (H&E) stained breast histology images with .tiff format of size 2048 x1536 pixels.
The microscopy images were annotated as normal, benign, in situ carcinoma or invasive carcinoma according to the predominant cancer type in each image.
The training dataset contains a total of 400 microscopy images, distributed fairly between the four classes, 100 images for each class. The test dataset contains a total of 100 microscopy images.

5.6.3 The model submitted

The model that we have submitted is the same model that we have presented above.

5.6.4 Results

Evaluation criteria

The performance on histology images is evaluated on the basis of the overall prediction accuracy (the ratio between correct samples and the total number of evaluated images).

The challenge received a total of 51 submissions, out of 677 registrations and the performance of each model was computed by the challenge organizers.

We obtained an accuracy of 81%, this allowed us to be in the 10 top performing challenge methods. Four experts have classified test images, Expert 1 and Expert 3 are breast cancer specialists, Expert 2 and Expert 4 are pathologists.

The organizers of challenge [10] mention that Expert 1 contributed in the construction of dataset challenge, where the pathologists in this phase have used other information (of other region and Immunohistochemistry (IHC) analysis[2]) to annotate the images.

Table 5.2 and 5.3 present the final results of the submission models to BACH challenge. We remind the readers that the top performing methods are detailed in the state of the art chapter.

[2]Immunohistochemistry (IHC) analysis is a method for demonstrating the presence and location of proteins in tissue.

Team	Authors	Country	Approach	Accuracy (%)
216	Chennamsetty et al. [225]	India	ResNet-101; DenseNet-161	87
248	Kwok [226]	Hong Kong SAR	Inception-ResNet-v2	87
1	Brancati et al. [227]	Italy	ResNet-34, 50, 101	86
16	Marami et al. [228]	USA	Inception-v3	84
54	Kohl et al. [229]	UK|Germany	DenseNet-161	83
157	Wang et al. [230]	China	VGG-16	83
186	Steinfeldt et al.	-	Xception	81
19	Koné and Boulmane [231]	Morocco	ResNeXt50	81
36	**Nedjar et al.**	**Algeria|Belgium**	**Inceptionv3,ResNet-50, MobileNet**	**81**
412	Ravi et al.	India	ResNet-152	80
22	Wang et al. [300]	USA	VGG-16	79
425	Cao et al. [301]	Canada|France	PTFAS,GLCM, ResNet-18, ResNeXt, NASNet-A,ResNet-152, VGG16, Random Forest SVM	79
60	Seo et al.	Korea	ResNet, Inception- V3, Random Forests	79
370	Sidhom et al.	USA	ResNet-50	78
242	Guo et al. [302]	China	GoogLeNet	77
61	Ranjan et al.	-	AlexNet	77
73	Mahbod et al. [303]	Austria|Sweden	ResNet-50, ResNet-101	77
18	Ferreira et al. [304]	Portugal	Inception-ResNet-v2	76
256	Pimkin et al. [305]	Russia	ResNet34, DenseNet169, DenseNet201,XGBoost	76

358	Sarker et al.	South Korea Russia	Inception-v4	75
98	Rakhlin et al. [306]	Russia|USA	VGG16,ResNet-50, IcenptionV3	74
164	Iesmantas and Alzbutas [307]	Lithuania	Custom CNN (CapsuleNetwork)	72
253	Xie et al.	China	CNN	72
268	Weiss et al. [308]	Germany	Xception, Logistic Regression	72
6	Awan et al. [309]	UK	ResNet50,SVM	71
62	Liang	-	VGG16,VGG19, ResNet50, InceptionV3, Inception-ResNet, k-NN	70
248	Kwok [226]	Hong Kong SAR	Inception-ResNet-v2	69
16	Marami et al. [228]	USA	Inception-v3+adaptive pooling	55
296	Jia et al.	China	ResNet-50 + multiscale atrous convolution	52
137	Li et al.	-	VGG16,DeepLabV2 ,ResNet50	52
91	Murata et al.	Japan	U-Net	50
264	Galal and Sanchez-Freire [310]	USA	DenseNet	50
166	Vu et al. [311]	Korea	DenseNet,SENet,ResNet	49
54	Kohl et al. [229]	UK|Germany	DenseNet-161	42

Table 5.2: The final results of BACH challenge [10][11]

Team	Acc	Normal		Benign		In situ		Invasive	
		Se	Sp	Se	Sp	Se	Sp	Se	Sp
216	0.87	0.96	0.88	0.8	0.96	0.84	1.0	0.88	0.99
248	0.87	0.96	0.93	0.72	0.96	0.88	0.97	0.92	0.96
1	0.86	0.96	0.91	0.68	0.97	0.84	0.99	0.96	0.95
16	0.84	0.92	0.95	0.64	0.96	0.84	0.99	0.96	0.89
54	0.83	0.96	0.92	0.52	0.97	0.88	0.92	0.96	0.96
157	0.83	0.96	0.91	0.64	0.99	0.92	0.91	0.8	0.97
186	0.81	0.96	0.92	0.68	0.96	0.76	0.95	0.84	0.92
19	0.81	1.0	0.95	0.4	0.99	0.92	0.92	0.92	0.89
36	0.81	0.88	0.92	0.6	0.96	0.88	0.95	0.88	0.92
412	0.8	0.92	0.96	0.48	0.97	0.84	0.92	0.96	0.88
Exp1	0.96	0.96	0.99	0.92	0.97	1.0	1.0	0.96	0.99
Exp2	0.94	0.96	0.99	0.88	0.96	1.0	1.0	0.92	0.97
Exp3	0.78	0.88	0.99	0.76	0.79	0.56	0.97	0.92	0.96
Exp4	0.73	0.40	0.99	0.84	0.71	0.76	0.97	0.92	0.97
Exp avg	0.85 ±0.10	0.80 ±0.23	0.99 ±0.00	0.85 ±0.06	0.86 ±0.11	0.83 ±0.18	0.99 ±0.01	0.93 ±0.02	0.97 ±0.01

Table 5.3: Details results at sensitivity (Se) and specificity (SP) of the 10 top performing challenge methods for the four classes [10]

5.6.5 Discussion

The histological images classification is a very difficult task. This is due to several reasons in particular the intra-class variability, whether in the color and spatial arrangement of the tissues structures, often experts use IHC analysis as additional information to classify the images.

As deep learning methods have proven to be effective in the medical field, all participants of the challenge used these methods to overcome the problem of histological images classification.

The top 10 performing methods of the BACH challenge, outperform two expert (see Table 5.3) Expert 3 is breast cancer specialist and Expert 4 is pathologist. This prove that the IA methods can bring a lot of reassuring in the medical field.

The two methods [225] [226] that won the challenge were based on using an ensemble of CNNs for images classification, because the performance of deep learning methods depend on the hyper parameters of the CNNs and the training dataset, using a combined CNNs with different configuration and training on varying datasets, was the best strategy used by the winners.

We recall that the CNNs need large amounts of training data to produce a generalizable model, as the training dataset given by the challenge contain only 400 images, to overcome this issue, some submitted methods used data augmentation approach to augment the training data, others have used external dataset like BreakHis and some of them used the training data

given in the part B of the challenge (10 Whole-slide images).

The 10 performing methods have used different architectures: ResNet, DenseNet, Inception,VGG, XCeption, MobileNet. Despite to this, the results were very close with a standard deviation of 0.026. We notice that some architectures have been more used than others, for example ResNet was the most used, in which from the 10 methods 6 of them used it, followed by Inception used in 3 methods and then DenseNet in 2 methods. This CNNs were used in different manner but they give a good results in this specific classification problem.

We also remark that the three best methods are based on combination of CNNs, Chennamsetty et al. [225] used ResNet-101 and DenseNet-161, Kwok [226] used Inception and ResNet-v2, Brancati et al. [227] used ResNet-34, 50, 101.

In our proposed method we have used the combination of the two most used architectures namely ResNet and Inception with MobileNet. A difficulty was found by our method to predict the normal case (see Table 5.3), in which there was a remarkable difference in sensitivity compared to others methods. We explains this by the fact that the images in the benign and normal case have a great resemblance which make their classification difficult. As was mentioned in the overview paper of the challenge [10] the benign class presents considerable histological structures variability, where the tissue contains normal and benign lesions structures, makes this class hard to distinguish from normal tissue. Also the organizers report in [10] that in the image acquisition of normal tissue, the specialists tend to capture non-relevant structures, such as fat cells; that affect the efficacy of the method. Despite this, the method achieved the score of 0.88 for In situ sensitivity, that outperform 5 methods and is equal to 2 methods of the 10 performing methods. The same sensitivity score is obtained for Invasive with a specificity of 92%.

We conclude that the efficacy of CNN depend on the network architecture and the training dataset used.

5.7 Conclusion

We have presented the proposed method for tumor cancer detection using histopathological image, as the method was based on convolutional neural networks in the first part of this chapter, we have reviewed the history of deep learning and the fundamentals concept of CNNs starting by defining layers types and the different architectures. Then, the proposed method was detailed by the experimental results shown and the comparative study with related works was achieved. In fact, among the 22 methods of the state of art that classify histopathological image as malignant and benignant, our method outperform 19 methods at the image level and 20 methods at the patient level. Also, the proposed method was among the first 10 methods of BACH challenge for multiclass classification of the histopathological images.

General conclusion

Computer-aided detection and diagnosis CADe/CADx systems have been extensively investigated in the clinical diagnoses, because they contribute to help the radiologists in their diagnostic by reducing the perceptual errors, also by providing image analysis based on computer image quantification resulting a comprehensive and exhaustive information.

In this thesis, the main aim was to develop several methods of CAD systems for liver and breast lesions description and discrimination. To achieve these objectives, the proposed work was partitioned on two axes, the first one is liver CT annotation, the second is breast density and lesions classification.

In the first part of this thesis, we have developed three different methods for liver CT images annotation.

The first method was based on the classification approach, in which the shape and texture features extracted from the liver CT images are feed forward to random forest classifier, where for each annotation a classifier was trained to predict the appropriate annotation.

The second method was based on content-based image retrieval approach, where we have applied a binary indexation of the liver CT image to extract its signature. This last one was used to retrieve similar images to the test image from the dataset. Thereafter the majority vote was applied to assign the elected annotations to the adequate liver image properties.

The third method developed for liver CT annotation was based on spectral image textural analysis, by using a combination of Bidimensional Empirical Mode Decomposition (BEMD) and Gabor wavelet transform to index the images content. Then the similarity distance was applied to retrieve the most similar images to the test image, where the suitable annotations were assigned to the test image.

The second part of this thesis concern breast study, where we focused on breast density classification and breast lesions discrimination. In fact, we have developed a whole end to end method for breast density classification according to the standard Breast Imaging Reporting and Data System (BI-RADS) that classify the density into four classes, in addition we have performed the two classes classification (fatty and dense). Given that the two datasets used in the experimentation were unbalanced, we have also proposed a modification to the existing equilibrate algorithm named Synthetic Minority Over-Sampling Technique Algorithm (SMOTE). The obtained results showed that the modification introduced make the SMOTE algorithm more efficient. In the breast lesions classification problem, we have

used the Convolutional Neural Networks (CNNs) to give an efficient solution. The strategy that we followed was based on the combination of three different CNN namely InceptionV3, ResNet50 and MobileNet. Our supposition is based on the fact that each CNN have its capacity and characteristics to extract the salient features from the image. The experiments were carried out on two different datasets. Where, in the first dataset we used the method to classify the benignant and malignant lesions. In the second dataset, the method was used to classify the histopathology images into normal, benign, in situ and invasive cases.

All the proposed methods were evaluated on international challenges, in order to prove their effectiveness compared to the new methods that have been developed by the community scientific. We concluded that the results achieved were satisfactory, despite the fact that we found some limitations to realize them.

Limitations

Liver CT annotation

- The dataset that we have used contain a small number of images and some properties didn't have any sample in the dataset. Which affected the performance of the machine learning used.
- There isn't another public dataset for liver annotation, that led us to test the methods only on the dataset given by challenge.
- The dataset contains only four common types of liver lesions namely Cysts, Haemangiomas for benign cases and HCC, Metastases for malignant.

Breast lesion classification

- There isn't a public annotated dataset for lesions in the histopathology images, therefore we were limited to use the classification approaches.
- The BreakHis dataset was unbalanced, despite that we have used the augmentation techniques to overcome this problem, but this technique doesn't represent an effective solution in the medical field.
- The dataset of BreAst Cancer Histology image (BACH) challenge contained a small number of images, that conducted us to use the transfer learning approaches to train the model.

Future works

The methods presented can be extended and improved to enhance the computer-aided diagnostic systems by investigating several aspects that include:

- The use of ontology not only in the annotations but also for inference to interpret the annotations.
- The combination of different modalities to extract more precise information.
- The use of the CNN visualization methods to understand and improve the CNN classification decision.
- The use of relevance feedback approaches to improve the retrieval accuracy.
- Investigate more recent deep learning methods.
- Explore more efficient low level features.
- Setting up an online platform for diagnosis based on content-based medical image retrieval.
- Finally, to avoid the limited access to datasets. The necessity to collect, to organize and to share an annotated database is an important step to facilitate the research for us and also the scientific community.

Appendix A

In this appendix, we will present the different CNNs architectures defined in section 5.3.3. We recall that the architectures are: LeNet-5, AlexNet, Inception-v1, Inception-v3, Resnet, Xception, DenseNet, MobileNet-v1, MobileNet-v2, EfficientNet, Noisy Student.

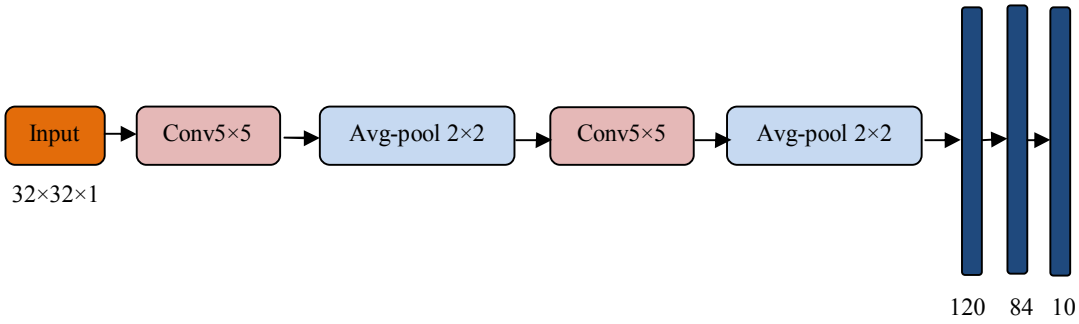

Figure A.1: LeNet-5 architecture

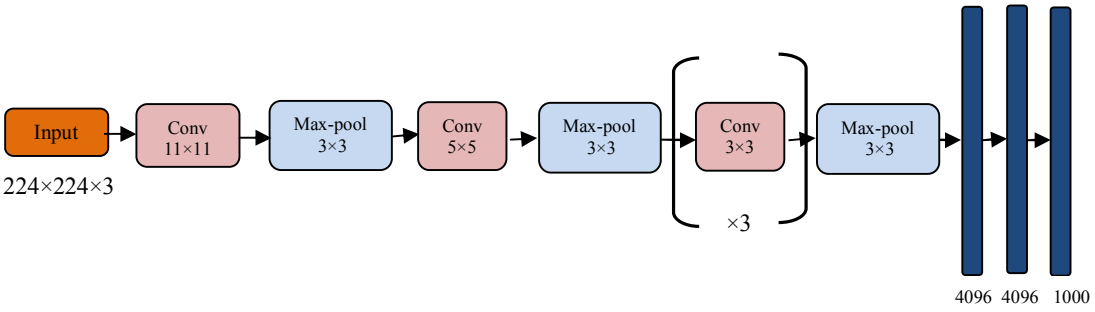

Figure A.2: AlexNet architecture

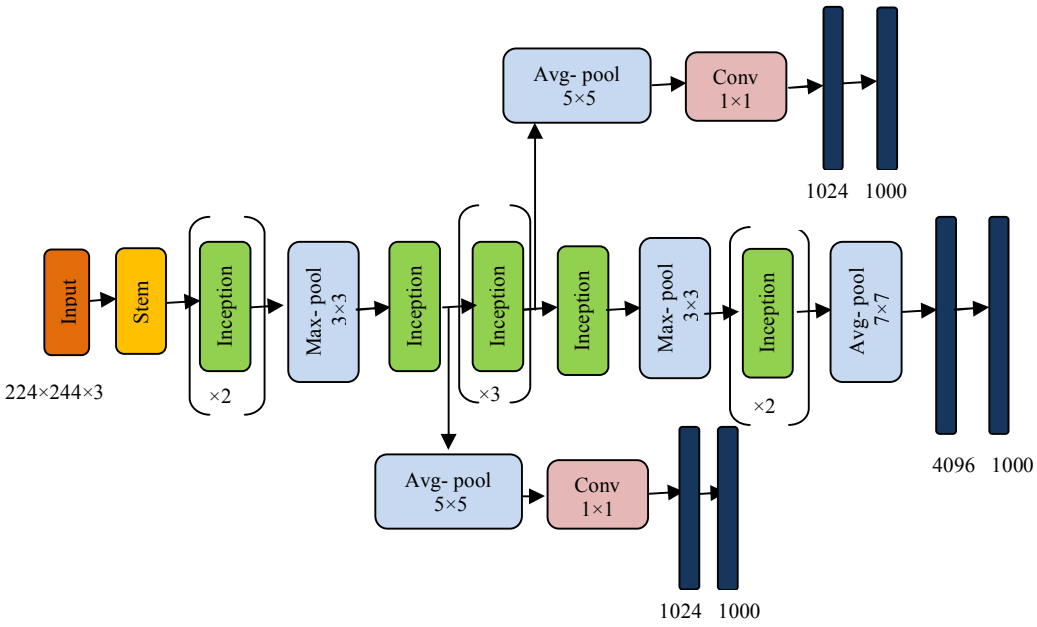

Figure A.3: Inception-v1 architecture

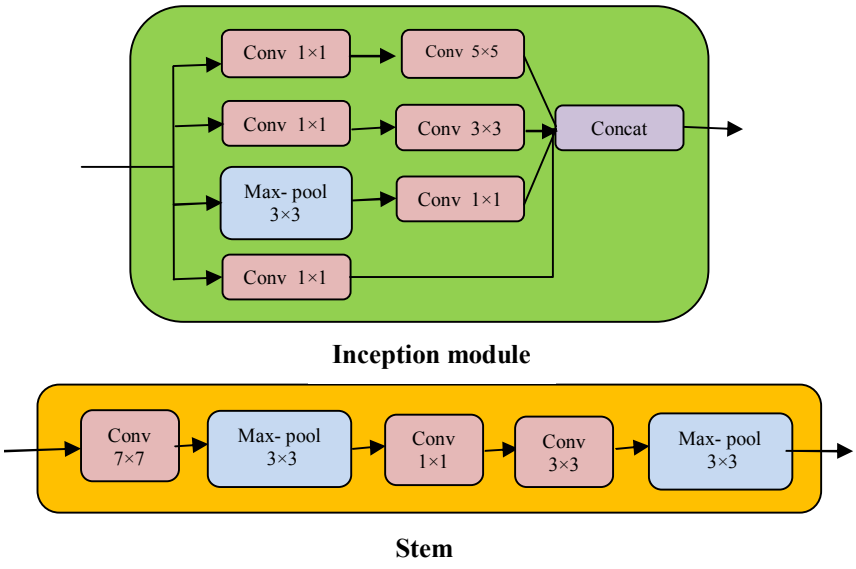

Figure A.4: Inception module and Stem architecture

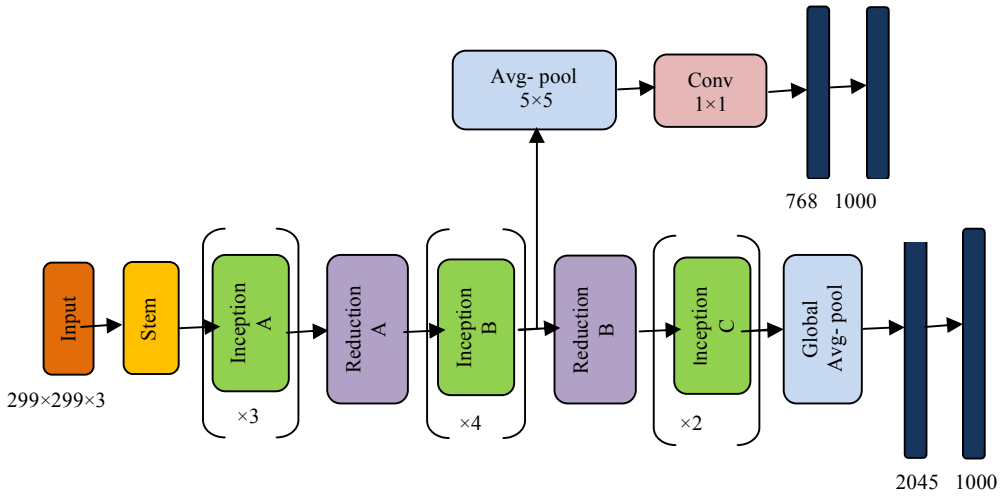

Figure A.5: Inception-v3 architecture

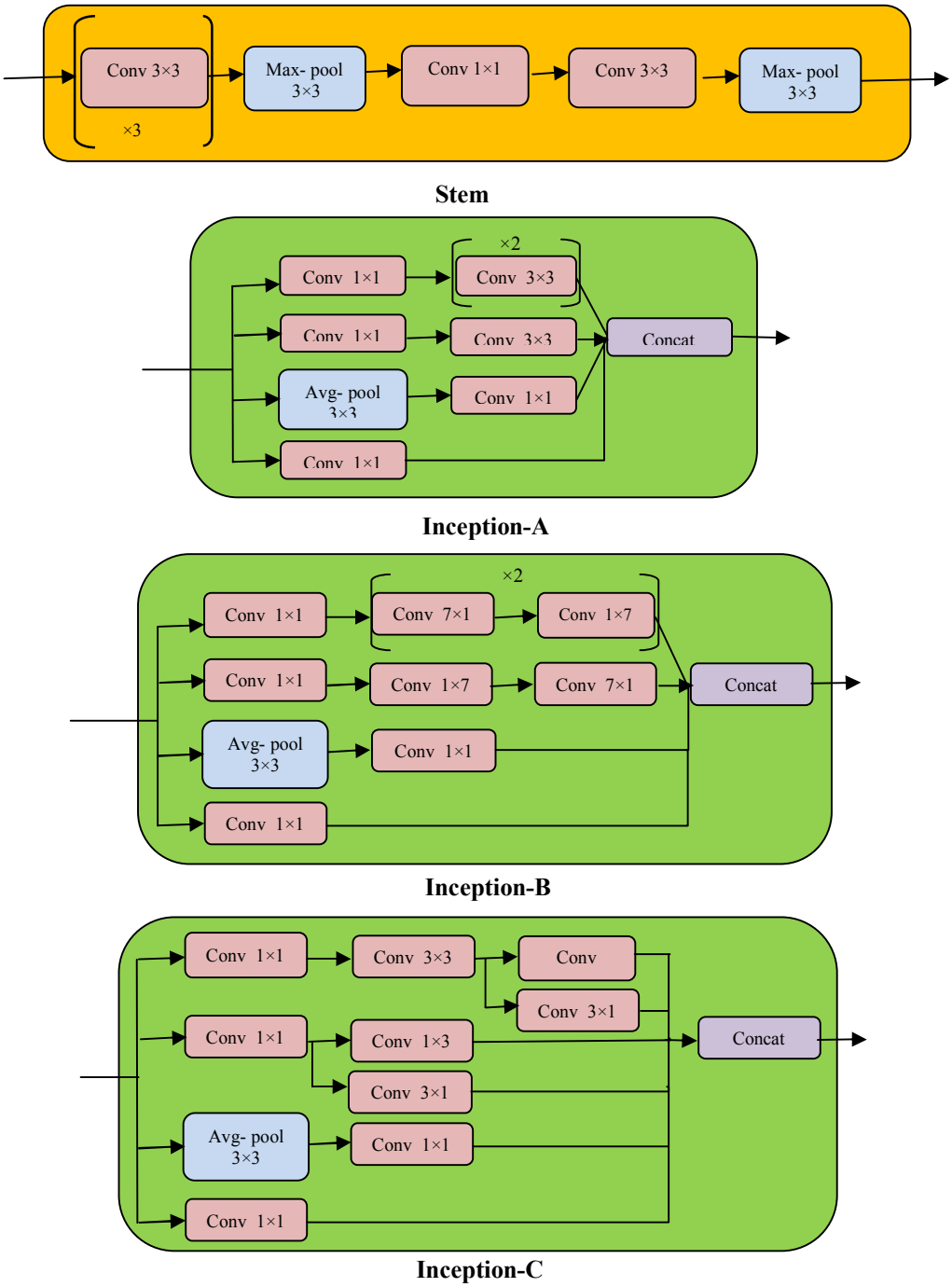

Figure A.6: InceptionV3 module A-B-C and Stem

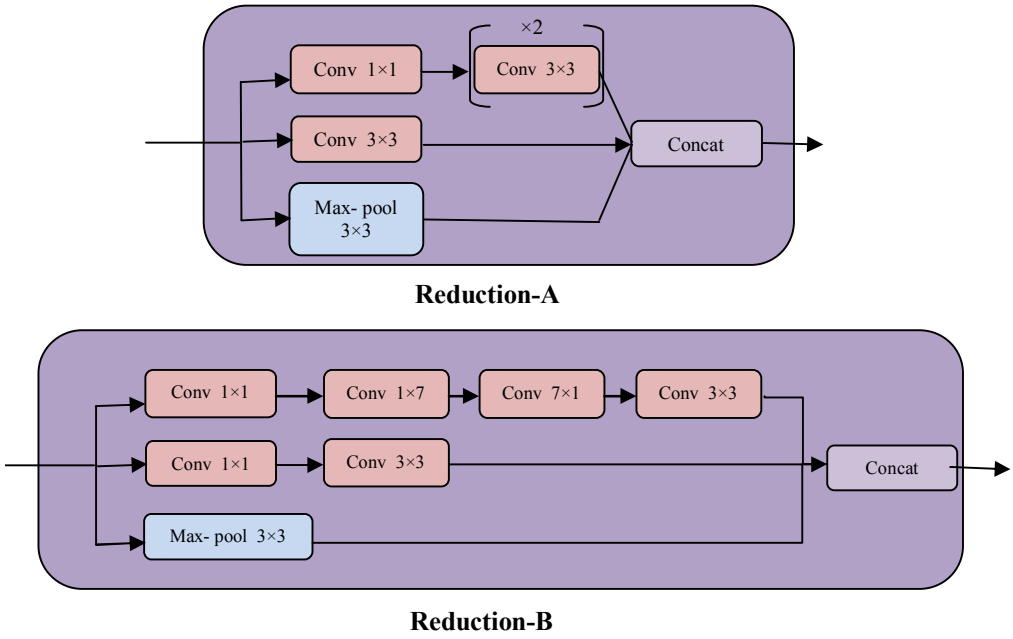

Figure A.7: Reduction A-B of InceptionV3 architecture

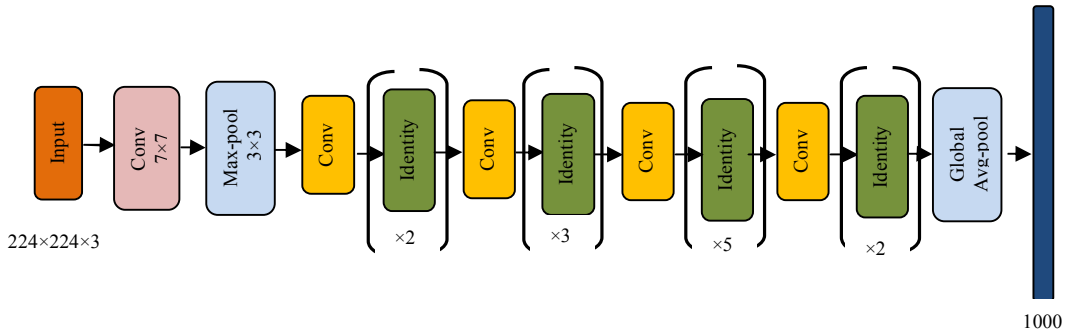

Figure A.8: ResNet architecture

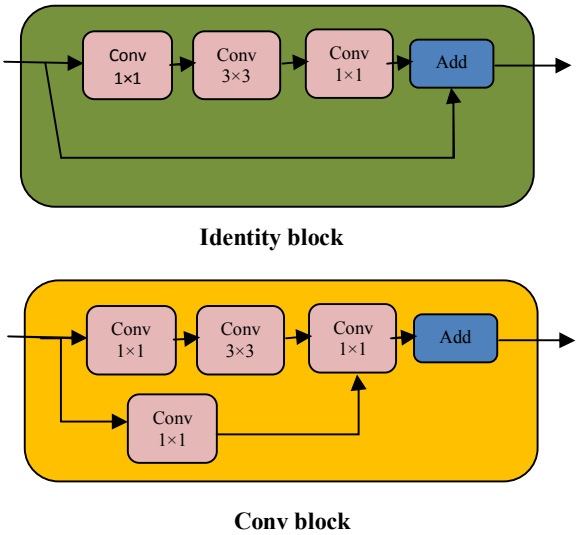

Figure A.9: Identity and convolution block of ResNet

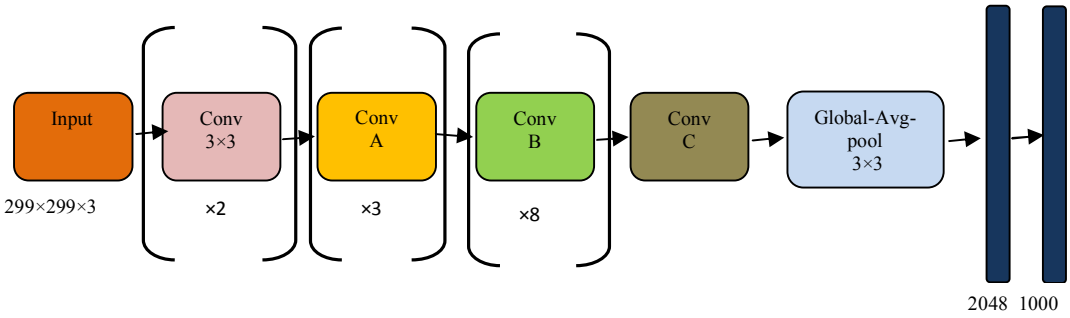

Figure A.10: Xception architecture

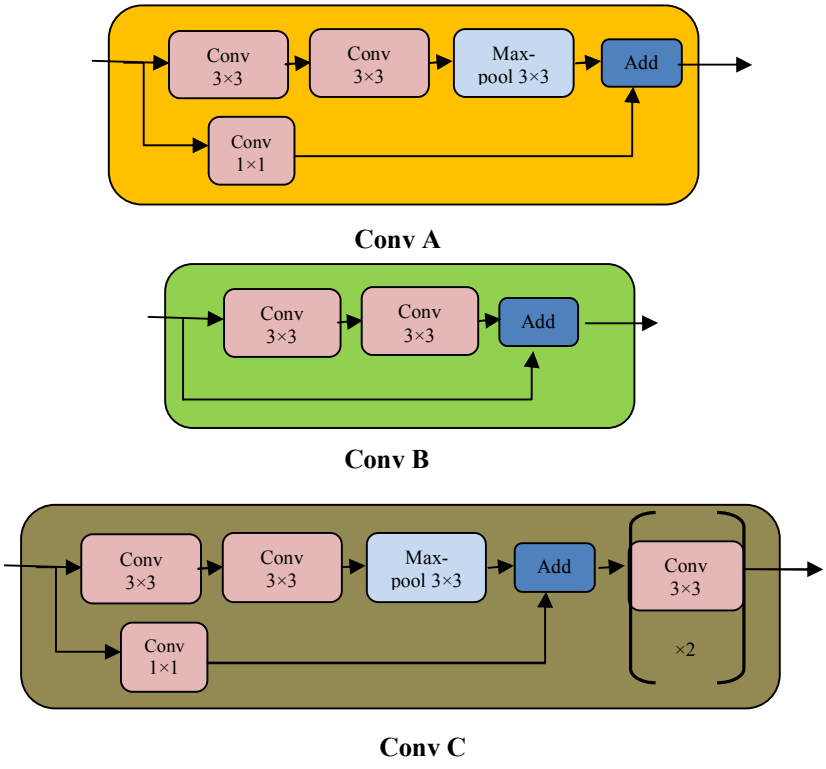

Figure A.11: Conv A,B,C of Xception

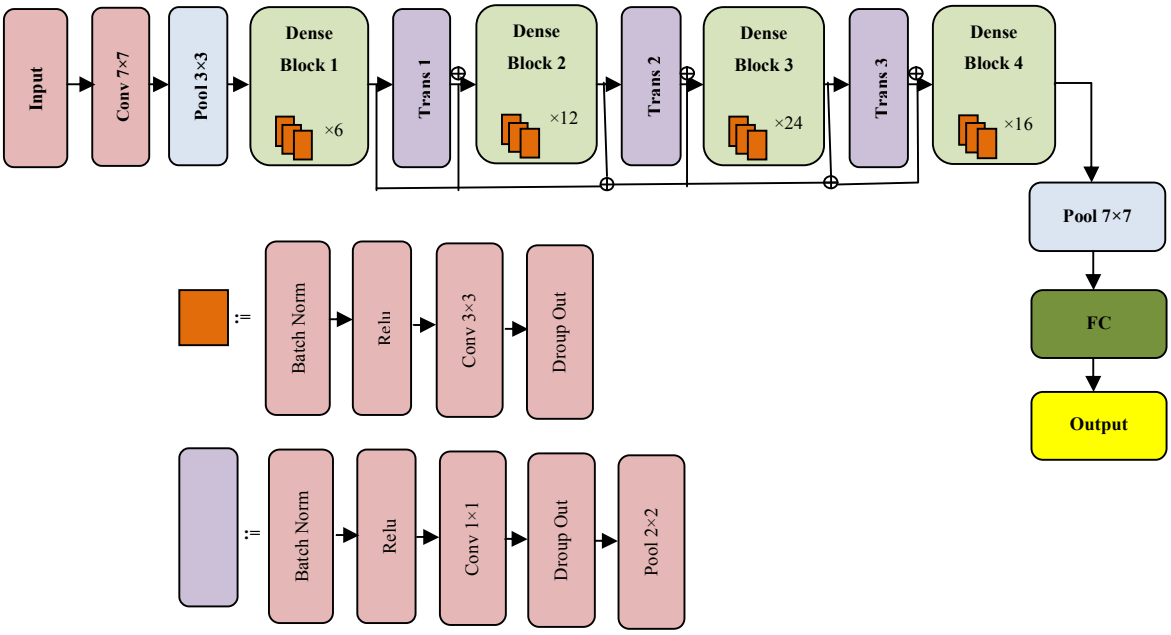

Figure A.12: DenseNet-121 architecture

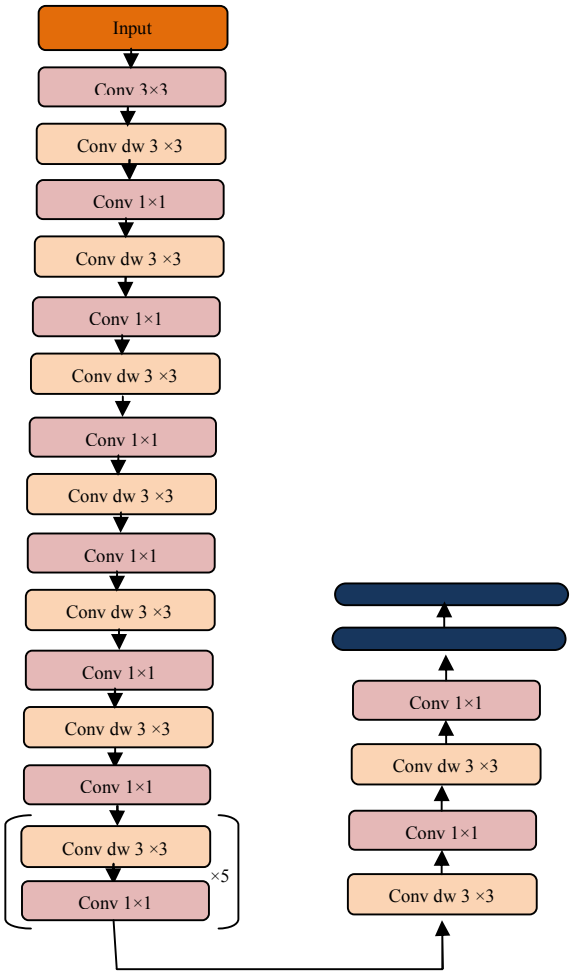

Figure A.13: MobileNet-v1 Architecture

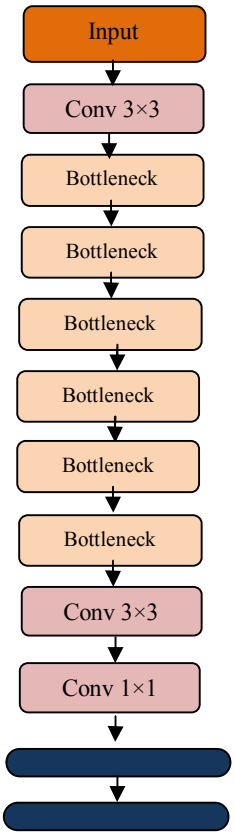

Figure A.14: MobileNet-v2 Architecture

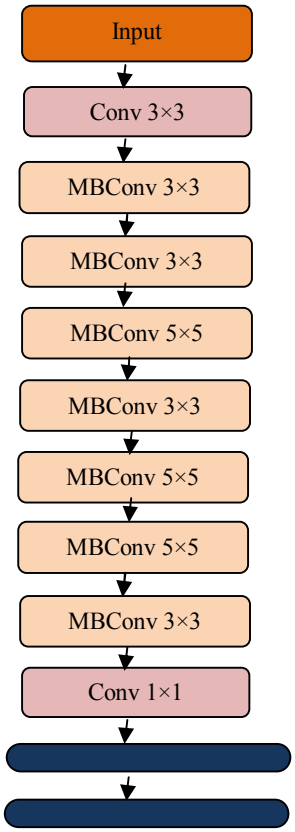

Figure A.15: EfficientNet architecture

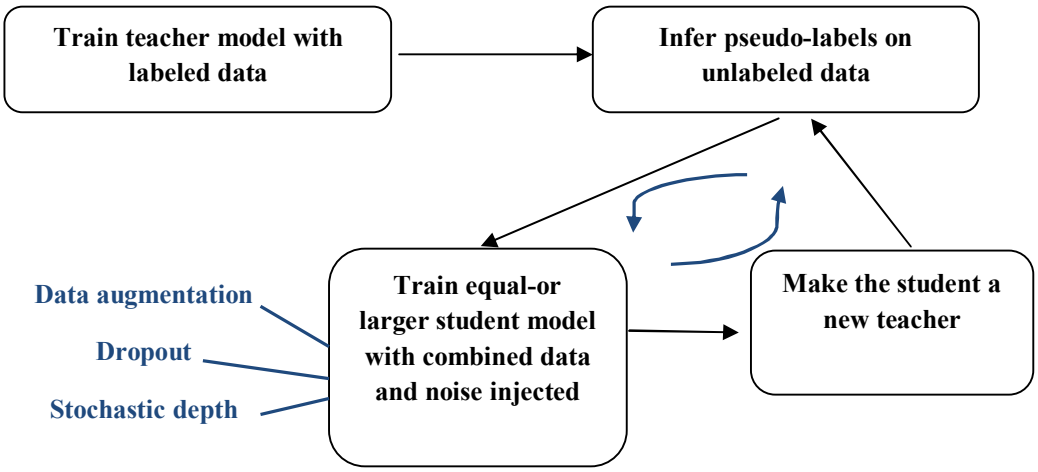

Figure A.16: Noisy Student architecture

References

[1] livercentrewa, "Liver resection-hepatectomy," https://www.livercentrewa.com.au/treatments/liver-treatment-surgery-specialist-perth, visited on April 13,2020.

[2] cancer.org, "What is liver cancer?" https://www.cancer.org/cancer/liver-cancer/about/what-is-liver-cancer.html, visited on April 12,2020.

[3] A. Javed and A. Lteif, "Development of the human breast," in *Seminars in plastic surgery*, vol. 27, no. 01. Thieme Medical Publishers, 2013, pp. 005–012.

[4] DREAM-Challenge, "The digital mammography dream challenge," https://www.synapse.org/#!Synapse:syn4224222/wiki/401749, visited on May 29,2020.

[5] F. A. Spanhol, L. S. Oliveira, C. Petitjean, and L. Heutte, "A dataset for breast cancer histopathological image classification," *IEEE Transactions on Biomedical Engineering*, vol. 63, no. 7, pp. 1455–1462, 2016.

[6] N. B. Marvasti, M. d. M. R. García, S. Üsküdarli, J. F. A. Montes, and B. Acar, "Overview of the imageclef 2015 liver ct annotation task." in *CLEF (Working Notes)*, 2015.

[7] I. Nedjar, S. Mahmoudi, and M. A. Chikh, "Content-based medical image retrieval for liver ct," in *CLEF2015 Working Note.CEUR Workshop Proceedings,CEUR-WS.org, Toulouse,France, Septembre 8-11*, 2015.

[8] ——, "Content-based medical image tetrieval for liver ct annotation," *Transactions on Machine Learning and Artificial Intelligence*, vol. 5, no. 4, 2017.

[9] V. Agarwal and D. Odgers, "Predicting semantic features from ct images of liver lesions using deep learning," *CS 229 Final Project Autumn*, 2013.

[10] G. Aresta, T. Araújo, S. Kwok, S. S. Chennamsetty, M. Safwan, V. Alex, B. Marami, M. Prastawa, M. Chan, M. Donovan *et al.*, "Bach: Grand challenge on breast cancer histology images," *Medical image analysis*, vol. 56, pp. 122–139, 2019.

[11] iciar2018 challenge, "Part a - microscopy images," https://iciar2018-challenge.grand-challenge.org/Legacy-results/, visited on May 29,2020.

[12] World-Health-Organization, "Cancer," https://www.who.int/news-room/fact-sheets/detail/cancer, visited on April 25,2020.

[13] Peconic-Bay-Medical, "The important role medical imaging plays in diagnosis and treatment," https://www.pbmchealth.org/news-events/blog/important-role-medical-imaging-plays-diagnosis-and-treatment, visited on April 24,2020.

[14] R. Smith-Bindman, D. L. Miglioretti, and E. B. Larson, "Rising use of diagnostic medical imaging in a large integrated health system," *Health affairs*, vol. 27, no. 6, pp. 1491–1502, 2008.

[15] World-Health-Organization, "Cancer profile 2020," https://www.paho.org/hq/index.php?option=com_docman&view=download&category_slug=4-cancer-country-profiles-2020&alias=51561-global-cancer-profile-2020&Itemid=270&lang=fr, visited on April 25,2020.

[16] T. Schaffter, D. S. Buist, C. I. Lee, Y. Nikulin, D. Ribli, Y. Guan, W. Lotter, Z. Jie, H. Du, S. Wang *et al.*, "Evaluation of combined artificial intelligence and radiologist assessment to interpret screening mammograms," *JAMA network open*, vol. 3, no. 3, pp. e200 265–e200 265, 2020.

[17] imaginis, "The role of medical imaging in the prevention, diagnosis and treatment of cancer," https://www.imaginis.com/cancer/the-role-of-medical-imaging-in-the-prevention-diagnosis-and-treatment-of-cancer, visited on April 25,2020.

[18] B. L. Sprague, E. F. Conant, T. Onega, M. P. Garcia, E. F. Beaber, S. D. Herschorn, C. D. Lehman, A. N. Tosteson, R. Lacson, M. D. Schnall *et al.*, "Variation in mammographic breast density assessments among radiologists in clinical practice: a multicenter observational study," *Annals of internal medicine*, vol. 165, no. 7, pp. 457–464, 2016.

[19] A. Kalra and F. Tuma, "Physiology, liver," in *StatPearls [Internet]*. StatPearls Publishing, 2018.

[20] Pharma-Tips, "Human anatomy & physiology of the liver," http://www.pharmatips.in/Articles/Human-Anatomy/Human-Anatomy-Physiology-Of-The-Liver.aspx, visited on April 06,2020.

[21] healthline, "Portal vein," https://www.healthline.com/human-body-maps/portal-vein#1, visited on April 06,2020.

[22] pie.med.utoronto, "Interactive 3d liver anatomy," http://pie.med.utoronto.ca/vliver/VLiver_content/VLiver_interactiveLiver.html, visited on April 07,2020.

[23] R. Saxena, N. D. Theise, and J. M. Crawford, "Microanatomy of the human liver—exploring the hidden interfaces," *Hepatology*, vol. 30, no. 6, pp. 1339–1346, 1999.

[24] B. J. Potter, "Components of the hepatic system,," in *xPharm: The Comprehensive Pharmacology Reference*. science Direct, 2007, pp. 1–5.

[25] R. C. Cattley and J. M. Cullen, "Liver and gall bladder," in *Haschek and Rousseaux's Handbook of Toxicologic Pathology*. Elsevier, 2013, pp. 1509–1566.

[26] L. Rui, "Energy metabolism in the liver," *Comprehensive physiology*, vol. 4, no. 1, pp. 177–197, 2011.

[27] D. Raddatz and G. Ramadori, "Carbohydrate metabolism and the liver: actual aspects from physiology and disease," *Zeitschrift für Gastroenterologie*, vol. 45, no. 01, pp. 51–62, 2007.

[28] T. Physiology, "Metabolic functions of the liver," https://teachmephysiology.com/gastrointestinal-system/liver/metabolic-functions-liver/, visited on April 09,2020.

[29] P. Nguyen, V. Leray, M. Diez, S. Serisier, J. L. Bloc'h, B. Siliart, and H. Dumon, "Liver lipid metabolism," *Journal of animal physiology and animal nutrition*, vol. 92, no. 3, pp. 272–283, 2008.

[30] V. Pathophysiology, "Metabolic functions of the liver," http://www.vivo.colostate.edu/hbooks/pathphys/digestion/liver/metabolic.html, visited on April 09,2020.

[31] Centre-hepato, "Les fonctions du foie," https://www.centre-hepato-biliaire.org/maladies-foie/fonctions-h\%C3\%A9patiques.html, visited on April 09,2020.

[32] Futura-sciences, "Foie," https://www.futura-sciences.com/sante/definitions/biologie-foie-6966/, visited on April 09,2020.

[33] K. Sheth and P. Bankey, "The liver as an immune organ," *Current opinion in critical care*, vol. 7, no. 2, pp. 99–104, 2001.

[34] B. Gao, "Basic liver immunology," *Cellular & molecular immunology*, vol. 13, no. 3, pp. 265–266, 2016.

[35] H. Peng, X. Jiang, Y. Chen, D. K. Sojka, H. Wei, X. Gao, R. Sun, W. M. Yokoyama, and Z. Tian, "Liver-resident nk cells confer adaptive immunity in skin-contact inflammation," *The Journal of clinical investigation*, vol. 123, no. 4, pp. 1444–1456, 2013.

[36] medlineplus, "Liver diseases," https://medlineplus.gov/liverdiseases.html, visited on April 09,2020.

[37] P. Angulo, "Obesity and nonalcoholic fatty liver disease," *Nutrition reviews*, vol. 65, no. suppl_1, pp. S57–S63, 2007.

[38] Sante-net, "Cirrhose du foie," https://www.sante-sur-le-net.com/maladies/hepato-gastro/cirrhose-du-foie, visited on April 11,2020.

[39] American-Liver-Foundation, "Wilson disease," https://liverfoundation.org/for-patients/about-the-liver/diseases-of-the-liver/wilson-disease/, visited on April 11,2020.

[40] ——, "Benign liver tumors," https://liverfoundation.org/for-patients/about-the-liver/diseases-of-the-liver/benign-liver-tumors/, visited on April 11,2020.

[41] N. Bajenaru, V. Balaban, F. Săvulescu, I. Campeanu, and T. Patrascu, "Hepatic hemangioma-review," *Journal of medicine and life*, vol. 8, no. Spec Issue, p. 4, 2015.

[42] A. Venturi, F. Piscaglia, G. Vidili, S. Flori, R. Righini, R. Golfieri, and L. Bolondi, "Diagnosis and management of hepatic focal nodular hyperplasia," *Journal of ultrasound*, vol. 10, no. 3, pp. 116–127, 2007.

[43] B. N. Nguyen, J.-F. Fléjou, B. Terris, J. Belghiti, and C. Degott, "Focal nodular hyperplasia of the liver: a comprehensive pathologic study of 305 lesions and recognition of new histologic forms," *The American journal of surgical pathology*, vol. 23, no. 12, p. 1441, 1999.

[44] M. Caremani, A. Vincenti, A. Benci, S. Sassoli, and D. Tacconi, "Ecographic epidemiology of non-parasitic hepatic cysts," *Journal of clinical ultrasound*, vol. 21, no. 2, pp. 115–118, 1993.

[45] healthline, "Liver cyst," https://www.healthline.com/health/liver-cyst, visited on April 11,2020.

[46] M. G. Thomeer, M. Broker, J. Verheij, M. Doukas, T. Terkivatan, D. Bijdevaate, R. A. De Man, A. Moelker, and J. N. IJzermans, "Hepatocellular adenoma: when and how to treat? update of current evidence," *Therapeutic advances in gastroenterology*, vol. 9, no. 6, pp. 898–912, 2016.

[47] radiopaedia, "Hepatic adenoma," https://radiopaedia.org/articles/hepatic-adenoma, visited on April 12,2020.

[48] J. Balogh, D. Victor III, E. H. Asham, S. G. Burroughs, M. Boktour, A. Saharia, X. Li, R. M. Ghobrial, and H. P. Monsour Jr, "Hepatocellular carcinoma: a review," *Journal of hepatocellular carcinoma*, vol. 3, p. 41, 2016.

[49] centre hepato, "Le carcinome hépatocellulaire (chc)," https://www.centre-hepato-biliaire.org/maladies-foie/cancers-foie/carcinome-hepatocellulaire.html, visited on April 12,2020.

[50] ——, "Le cholangiocarcinome intra-hépatique," https://www.centre-hepato-biliaire.org/maladies-foie/cancers-foie/cholangiocarcinome/cholangiocarcinome-intra-hepatique.html, visited on April 12,2020.

[51] C.-Y. Chien, C.-c. Hwang, C.-n. Yeh, H.-y. Chen, J.-T. Wu, S.-C. Chan, C.-L. Lin, C.-l. Yen, W.-y. Wang, and K.-C. Chiang, "Liver angiosarcoma, a rare liver malignancy, presented with intraabdominal bleeding due to rupture-a case report," *World journal of surgical oncology*, vol. 10, no. 1, p. 23, 2012.

[52] infocancer, "Les cancers primitifs du foie," https://www.arcagy.org/infocancer/localisations/appareil-digestif/cancers-du-foie/formes-de-la-maladie/les-cancers-primitifs-du-foie.html/, visited on April 12,2020.

[53] E. Hiyama, "Pediatric hepatoblastoma: diagnosis and treatment," *Translational pediatrics*, vol. 3, no. 4, p. 293, 2014.

[54] cancer.org, "Liver cancer risk factors," https://www.cancer.org/cancer/liver-cancer/causes-risks-prevention/risk-factors.html, visited on April 13,2020.

[55] ——, "Tests for liver cancer," https://www.cancer.org/cancer/liver-cancer/detection-diagnosis-staging/how-diagnosed.html, visited on April 13,2020.

[56] H. Ellis and V. Mahadevan, "Anatomy and physiology of the breast," *Surgery (Oxford)*, vol. 31, no. 1, pp. 11–14, 2013.

[57] M. sloan kettering, "Anatomy of the breast," https://www.mskcc.org/cancer-care/types/breast/anatomy-breast, visited on April 13,2020.

[58] A.bonnies, BA.Barnes, and H.Xuan, "Breast-anatomy-and-physiology," https://fr.slideshare.net/RishabhaSharma1/breast-anatomy-and-physiology, visited on October 31,2019.

[59] National-Breast-Cancer, "Breast cancer anatomy and how cancer starts," https://nbcf.org.au/about-breast-cancer/diagnosis/breast-cancer-anatomy/, visited on November 25,2019.

[60] Imaginis, "Breast anatomy and physiology," https://www.imaginis.com/breast-health-non-cancerous/breast-anatomy-and-physiology-1, visited on November 25,2019.

[61] Breast-Cancer-Now, "Breast changes during and after pregnancy," https://breastcancernow.org/information-support/have-i-got-breast-cancer/breast-changes-during-after-pregnancy, visited on November 25,2019.

[62] M. Guray and A. A. Sahin, "Benign breast diseases: classification, diagnosis, and management," *The oncologist*, vol. 11, no. 5, pp. 435–449, 2006.

[63] N. Masciadri and C. Ferranti, "Benign breast lesions: ultrasound," *Journal of ultrasound*, vol. 14, no. 2, pp. 55–65, 2011.

[64] L. C. Hartmann, T. A. Sellers, M. H. Frost, W. L. Lingle, A. C. Degnim, K. Ghosh, R. A. Vierkant, S. D. Maloney, V. S. Pankratz, D. W. Hillman *et al.*, "Benign breast disease and the risk of breast cancer," *New England Journal of Medicine*, vol. 353, no. 3, pp. 229–237, 2005.

[65] T. M. D'Alfonso, P. S. Ginter, and S. J. Shin, "A review of inflammatory processes of the breast with a focus on diagnosis in core biopsy samples," *Journal of pathology and translational medicine*, vol. 49, no. 4, p. 279, 2015.

[66] Y. Cong, H. Zou, G. Qiao, J. Lin, X. Wang, X. Li, Y. Li, and S. Zhu, "Bilateral mammary duct ectasia induced by sulpiride-associated hyperprolactinemia: A case report," *Oncology letters*, vol. 9, no. 5, pp. 2181–2184, 2015.

[67] R. A. Jensen, D. L. Page, W. D. Dupont, and L. W. Rogers, "Invasive breast cancer risk in women with sclerosing adenosis," *Cancer*, vol. 64, no. 10, pp. 1977–1983, 1989.

[68] J. R. Asirvatham, M. M. G. Falcone, and C. G. Kleer, "Atypical apocrine adenosis: diagnostic challenges and pitfalls," *Archives of pathology & laboratory medicine*, vol. 140, no. 10, pp. 1045–1051, 2016.

[69] cancer.org, "Hyperplasia of the breast (ductal or lobular)," https://www.cancer.org/cancer/breast-cancer/non-cancerous-breast-conditions/hyperplasia-of-the-breast-ductal-or-lobular.html#written_by, visited on November 08,2019.

[70] A. F. Logullo and C. Nimir, "Columnar cell lesions of the breast: a practical review for the pathologist," *Surgical and Experimental Pathology*, vol. 2, no. 1, pp. 1–8, 2019.

[71] S. E. Pinder and J. S. Reis-Filho, "Non-operative breast pathology: columnar cell lesions," *Journal of clinical pathology*, vol. 60, no. 12, pp. 1307–1312, 2007.

[72] S. P. Mishra, S. K. Tiwary, M. Mishra, and A. K. Khanna, "Phyllodes tumor of breast: a review article," *ISRN surgery*, vol. 2013, 2013.

[73] W. Y. Y. Chou, D. J. Veis, and R. Aft, "Radial scar on image-guided breast biopsy: is surgical excision necessary?" *Breast cancer research and treatment*, vol. 170, no. 2, pp. 313–320, 2018.

[74] A. Li and L. Kirk, "Intraductal papilloma," *StatPearls [Internet]*, 2019.

[75] cancer.org, "Fibroadenomas of the breast," https://www.cancer.org/cancer/breast-cancer/non-cancerous-breast-conditions/fibroadenomas-of-the-breast.html#references, visited on November 10,2019.

[76] K. Geethamala, B. Vani, V. S. Murthy, M. Radha *et al.*, "Fibroadenoma: A harbor for various histopathological changes," *Clinical Cancer Investigation Journal*, vol. 4, no. 2, p. 183, 2015.

[77] cancer.org, "Other non-cancerous breast conditions," https://www.cancer.org/cancer/breast-cancer/non-cancerous-breast-conditions/other-non-cancerous-breast-conditions.html, visited on November 11,2019.

[78] M. A. Kosir, "Breast cancer," https://www.merckmanuals.com/home/women-s-health-issues/breast-disorders/breast-cancer, visited on November 11,2019.

[79] cancer.org, "Invasive breast cancer (idc/ilc)," https://www.cancer.org/cancer/breast-cancer/understanding-a-breast-cancer-diagnosis/types-of-breast-cancer/invasive-breast-cancer.html, visited on November 17,2019.

[80] hopkinsmedicine.org, "Papillary breast cancer," https://www.hopkinsmedicine.org/kimmel_cancer_center/centers/breast_cancer_program/treatment_and_services/rare_breast_tumors/papillary_breast_cancer.html, visited on November 26,2019.

[81] Institut-cancer, "Cancers du sein," https://www.e-cancer.fr/Patients-et-proches/Les-cancers/Cancer-du-sein/Les-maladies-du-sein/Cancers-du-sein, visited on November 26,2019.

[82] Breastcancer.org, "Paget's disease of the nipple," https://www.breastcancer.org/symptoms/types/pagets, visited on November 26,2019.

[83] T. K. Arora, K. P. Terracina, J. Soong, M. O. Idowu, and K. Takabe, "Primary and secondary angiosarcoma of the breast," *Gland surgery*, vol. 3, no. 1, p. 28, 2014.

[84] cancer.org, "Breast mri," https://www.cancer.org/cancer/breast-cancer/screening-tests-and-early-detection/breast-mri-scans.html, visited on November 23,2019.

[85] T. Araújo, G. Aresta, E. Castro, J. Rouco, P. Aguiar, C. Eloy, A. Polónia, and A. Campilho, "Classification of breast cancer histology images using convolutional neural networks," *PloS one*, vol. 12, no. 6, 2017.

[86] Y. Chen, X. Yue, C. Zhong, and G. Wang, "Functional region annotation of liver ct image based on vascular tree," *BioMed research international*, vol. 2016, 2016.

[87] H. Alahmer *et al.*, "Automated characterisation and classification of liver lesions from ct scans," Ph.D. dissertation, University of Lincoln, 2018.

[88] X. Lu, J. Wu, X. Ren, B. Zhang, and Y. Li, "The study and application of the improved region growing algorithm for liver segmentation," *Optik*, vol. 125, no. 9, pp. 2142–2147, 2014.

[89] L. Rusko, G. Bekes, G. Nemeth, and M. Fidrich, "Fully automatic liver segmentation for contrast-enhanced ct images," *MICCAI Wshp. 3D Segmentation in the Clinic: A Grand Challenge*, vol. 2, no. 7, 2007.

[90] L. Massoptier and S. Casciaro, "A new fully automatic and robust algorithm for fast segmentation of liver tissue and tumors from ct scans," *European radiology*, vol. 18, no. 8, p. 1658, 2008.

[91] M. Moghbel, S. Mashohor, R. Mahmud, and M. I. B. Saripan, "Automatic liver tumor segmentation on computed tomography for patient treatment planning and monitoring," *EXCLI journal*, vol. 15, p. 406, 2016.

[92] L. Soler, H. Delingette, G. Malandain, J. Montagnat, N. Ayache, C. Koehl, O. Dourthe, B. Malassagne, M. Smith, D. Mutter *et al.*, "Fully automatic anatomical, pathological, and functional segmentation from ct scans for hepatic surgery," *Computer Aided Surgery*, vol. 6, no. 3, pp. 131–142, 2001.

[93] M. Ciecholewski and M. R. Ogiela, "Automatic segmentation of single and multiple neoplastic hepatic lesions in ct images," in *International work-conference on the interplay between natural and artificial computation*. Springer, 2007, pp. 63–71.

[94] H. Jiang, B. He, D. Fang, Z. Ma, B. Yang, and L. Zhang, "A region growing vessel segmentation algorithm based on spectrum information," *Computational and mathematical methods in medicine*, vol. 2013, 2013.

[95] Y.-j. QIAN, "A method for quickly and exactly extracting hepatic vessel," *DEStech Transactions on Computer Science and Engineering*, no. cece, 2017.

[96] K. Ahmadi, A. Karimi, and B. Fouladi Nia, "New technique for automatic segmentation of blood vessels in ct scan images of liver based on optimized fuzzy-means method," *Computational and mathematical methods in medicine*, vol. 2016, 2016.

[97] J. Wang, Y. Cheng, C. Guo, Y. Wang, and S. Tamura, "Shape–intensity prior level set combining probabilistic atlas and probability map constrains for automatic liver segmentation from abdominal ct images," *International journal of computer assisted radiology and surgery*, vol. 11, no. 5, pp. 817–826, 2016.

[98] A. Saito, S. Yamamoto, S. Nawano, and A. Shimizu, "Automated liver segmentation from a postmortem ct scan based on a statistical shape model," *International journal of computer assisted radiology and surgery*, vol. 12, no. 2, pp. 205–221, 2017.

[99] D. Smeets, B. Stijnen, D. Loeckx, B. De Dobbelaer, and P. Suetens, "Segmentation of liver metastases using a level set method with spiral-scanning technique and supervised fuzzy pixel classification," in *MICCAI workshop*, vol. 42, 2008, p. 43.

[100] S. Lu, H. Huang, P. Liang, G. Chen, and L. Xiao, "Hepatic vessel segmentation using variational level set combined with non-local robust statistics," *Magnetic resonance imaging*, vol. 36, pp. 180–186, 2017.

[101] M. Liao, Y.-q. Zhao, X.-y. Liu, Y.-z. Zeng, B.-j. Zou, X.-f. Wang, and F. Y. Shih, "Automatic liver segmentation from abdominal ct volumes using graph cuts and border marching," *Computer methods and programs in biomedicine*, vol. 143, pp. 1–12, 2017.

[102] G. Li, X. Chen, F. Shi, W. Zhu, J. Tian, and D. Xiang, "Automatic liver segmentation based on shape constraints and deformable graph cut in ct images," *IEEE Transactions on Image Processing*, vol. 24, no. 12, pp. 5315–5329, 2015.

[103] J. Stawiaski, E. Decenciere, and F. Bidault, "Interactive liver tumor segmentation using graph-cuts and watershed," in *11th International Conference on Medical Image Computing and Computer Assisted Intervention (MICCAI 2008)*, 2008.

[104] V. Pamulapati, A. Venkatesan, B. J. Wood, and M. G. Linguraru, "Liver segmental anatomy and analysis from vessel and tumor segmentation via optimized graph cuts," in *International MICCAI workshop on computational and clinical challenges in abdominal imaging*. Springer, 2011, pp. 189–197.

[105] P. Hu, F. Wu, J. Peng, P. Liang, and D. Kong, "Automatic 3d liver segmentation based on deep learning and globally optimized surface evolution," *Physics in Medicine & Biology*, vol. 61, no. 24, p. 8676, 2016.

[106] W. Li *et al.*, "Automatic segmentation of liver tumor in ct images with deep convolutional neural networks," *Journal of Computer and Communications*, vol. 3, no. 11, p. 146, 2015.

[107] D. L. Rubin, C. Rodriguez, P. Shah, and C. Beaulieu, "ipad: Semantic annotation and markup of radiological images," in *AMIA annual symposium proceedings*, vol. 2008. American Medical Informatics Association, 2008, p. 626.

[108] S. A. Napel, C. F. Beaulieu, C. Rodriguez, J. Cui, J. Xu, A. Gupta, D. Korenblum, H. Greenspan, Y. Ma, and D. L. Rubin, "Automated retrieval of ct images of liver lesions on the basis of image similarity: method and preliminary results," *Radiology*, vol. 256, no. 1, pp. 243–252, 2010.

[109] A. Baâzaoui, W. Barhoumi, A. Ahmed, and E. Zagrouba, "Semi-automated segmentation of single and multiple tumors in liver ct images using entropy-based fuzzy region growing," *IRBM*, vol. 38, no. 2, pp. 98–108, 2017.

[110] A. Mir, M. Hanmandlu, and S. Tandon, "Texture analysis of ct images," *IEEE Engineering in Medicine and Biology Magazine*, vol. 14, no. 6, pp. 781–786, 1995.

[111] K. Mala and V. Sadasivam, "Classification of fatty and cirrhosis liver using wavelet-based statistical texture features and neural network classifier," *International Journal of Software and Informatics*, vol. 4, no. 2, pp. 151–163, 2010.

[112] B. Ganeshan, K. A. Miles, R. C. Young, and C. R. Chatwin, "Texture analysis in non-contrast enhanced ct: impact of malignancy on texture in apparently disease-free areas of the liver," *European journal of radiology*, vol. 70, no. 1, pp. 101–110, 2009.

[113] M. Safdari, R. Pasari, D. Rubin, and H. Greenspan, "Image patch-based method for automated classification and detection of focal liver lesions on ct," in *Medical Imaging 2013: Computer-Aided Diagnosis*, vol. 8670. International Society for Optics and Photonics, 2013, p. 86700Y.

[114] I. Diamant, A. Hoogi, C. F. Beaulieu, M. Safdari, E. Klang, M. Amitai, H. Greenspan, and D. L. Rubin, "Improved patch-based automated liver lesion classification by separate analysis of the interior and boundary regions," *IEEE journal of biomedical and health informatics*, vol. 20, no. 6, pp. 1585–1594, 2015.

[115] I. Diamant, E. Klang, M. Amitai, E. Konen, J. Goldberger, and H. Greenspan, "Task-driven dictionary learning based on mutual information for medical image classification," *IEEE transactions on biomedical engineering*, vol. 64, no. 6, pp. 1380–1392, 2017.

[116] J. Stoitsis, I. Valavanis, S. G. Mougiakakou, S. Golemati, A. Nikita, and K. S. Nikita, "Computer aided diagnosis based on medical image processing and artificial intelligence methods," *Nuclear Instruments and Methods in Physics Research Section A: Accelerators, Spectrometers, Detectors and Associated Equipment*, vol. 569, no. 2, pp. 591–595, 2006.

[117] S. G. Mougiakakou, I. K. Valavanis, A. Nikita, and K. S. Nikita, "Differential diagnosis of ct focal liver lesions using texture features, feature selection and ensemble driven classifiers," *Artificial Intelligence in Medicine*, vol. 41, no. 1, pp. 25–37, 2007.

[118] J. Ye, Y. Sun, S. Wang, L. Gu, L. Qian, and J. Xu, "Multi-phase ct image based hepatic lesion diagnosis by svm," in *2009 2nd International Conference on Biomedical Engineering and Informatics*. IEEE, 2009, pp. 1–5.

[119] Y. Chi, J. Zhou, S. K. Venkatesh, Q. Tian, and J. Liu, "Content-based image retrieval of multiphase ct images for focal liver lesion characterization," *Medical physics*, vol. 40, no. 10, p. 103502, 2013.

[120] Y. Doron, N. Mayer-Wolf, I. Diamant, and H. Greenspan, "Texture feature based liver lesion classification," in *Medical Imaging 2014: Computer-Aided Diagnosis*, vol. 9035. International Society for Optics and Photonics, 2014, p. 90353K.

[121] M. I. Obayya, N. Areed, and A. O. Abdulhadi, "Liver cancer identification using adaptive neuro-fuzzy inference system," *International Journal of Computer Applications*, vol. 140, no. 8, pp. 1–7, 2016.

[122] C.-C. Chang, H.-H. Chen, Y.-C. Chang, M.-Y. Yang, C.-M. Lo, W.-C. Ko, Y.-F. Lee, K.-L. Liu, and R.-F. Chang, "Computer-aided diagnosis of liver tumors on computed tomography images," *Computer methods and programs in biomedicine*, vol. 145, pp. 45–51, 2017.

[123] A. Depeursinge, C. Kurtz, C. Beaulieu, S. Napel, and D. Rubin, "Predicting visual semantic descriptive terms from radiological image data: preliminary results with liver lesions in ct," *IEEE transactions on medical imaging*, vol. 33, no. 8, pp. 1669–1676, 2014.

[124] N. Kökciyan, R. Türkay, S. Üsküdarlı, P. Yolum, B. Bakır, and B. Acar, "Semantic description of liver ct images: an ontological approach," *IEEE journal of biomedical and health informatics*, vol. 18, no. 4, pp. 1363–1369, 2014.

[125] C. P. Langlotz, "Radlex: a new method for indexing online educational materials," 2006.

[126] A. B. Spanier, N. Caplan, J. Sosna, B. Acar, and L. Joskowicz, "A fully automatic end-to-end method for content-based image retrieval of ct scans with similar liver lesion annotations," *International journal of computer assisted radiology and surgery*, vol. 13, no. 1, pp. 165–174, 2018.

[127] D. Korenblum, D. Rubin, S. Napel, C. Rodriguez, and C. Beaulieu, "Managing biomedical image metadata for search and retrieval of similar images," *Journal of digital imaging*, vol. 24, no. 4, pp. 739–748, 2011.

[128] F. Gimenez, J. Xu, Y. Liu, T. Liu, C. Beaulieu, D. Rubin, and S. Napel, "Automatic annotation of radiological observations in liver ct images," in *AMIA Annual Symposium Proceedings*, vol. 2012. American Medical Informatics Association, 2012, p. 257.

[129] A. B. Spanier and L. Joskowicz, "Towards content-based image retrieval: From computer generated features to semantic descriptions of liver ct scans." in *CLEF (Working Notes)*, 2014, pp. 438–447.

[130] B. Ermis, A. T. Cemgil, N. B. Marvasti, and B. Acar, "Liver ct annotation via generalized coupled tensor factorization." in *CLEF (Working Notes)*, 2014, pp. 421–427.

[131] C. Kurtz, P.-A. Idoux, A. Thangali, F. Cloppet, C. F. Beaulieu, and D. L. Rubin, "Semantic retrieval of radiological images with relevance feedback," in *International Workshop on Multimodal Retrieval in the Medical Domain*. Springer, 2015, pp. 11–25.

[132] A. Kumar, S. Dyer, J. Kim, C. Li, P. H. Leong, M. Fulham, and D. Feng, "Adapting content-based image retrieval techniques for the semantic annotation of medical images," *Computerized Medical Imaging and Graphics*, vol. 49, pp. 37–45, 2016.

[133] S. Loveymi, M. H. Dezfoulian, and M. Mansoorizadeh, "Generate structured radiology report from ct images using image annotation techniques: Preliminary results with liver ct," *Journal of digital imaging*, vol. 33, p. 375–390, 2020.

[134] J. Pan, J. Zhang, S. Luo, J. Zhang, and Y. Liang, "Automatic annotation of liver computed tomography images based on a vessel-skeletonization method," *International Journal of Imaging Systems and Technology*, 2020.

[135] C. Kurtz, P. Gançarski, N. Passat, and A. Puissant, "A hierarchical semantic-based distance for nominal histogram comparison," *Data & Knowledge Engineering*, vol. 87, pp. 206–225, 2013.

[136] R. Nithya and B. Santhi, "Computer aided diagnosis system for mammogram analysis: a survey," *Journal of Medical Imaging and Health Informatics*, vol. 5, no. 4, pp. 653–674, 2015.

[137] A. M. Khuzi, R. Besar, W. W. Zaki, and N. Ahmad, "Identification of masses in digital mammogram using gray level co-occurrence matrices," *Biomedical imaging and intervention journal*, vol. 5, no. 3, 2009.

[138] F. Moayedi, R. Boustani, A. Kazemi, S. Katebi, and E. Dashti, "Subclass fuzzy-svm classifier as an efficient method to enhance the mass detection in mammograms," *Iranian Journal of Fuzzy Systems*, 2010.

[139] B. Zheng, X. Wang, D. Lederman, J. Tan, and D. Gur, "Computer-aided detection: the effect of training databases on detection of subtle breast masses," *Academic radiology*, vol. 17, no. 11, pp. 1401–1408, 2010.

[140] W. B. Sampaio, E. M. Diniz, A. C. Silva, A. C. De Paiva, and M. Gattass, "Detection of masses in mammogram images using cnn, geostatistic functions and svm," *Computers in Biology and Medicine*, vol. 41, no. 8, pp. 653–664, 2011.

[141] W. Zhu, X. Xiang, T. D. Tran, G. D. Hager, and X. Xie, "Adversarial deep structured nets for mass segmentation from mammograms," in *2018 IEEE 15th International Symposium on Biomedical Imaging (ISBI 2018)*. IEEE, 2018, pp. 847–850.

[142] V. K. Singh, S. Romani, H. A. Rashwan, F. Akram, N. Pandey, M. M. K. Sarker, S. Abdulwahab, J. Torrents-Barrena, A. Saleh, M. Arquez *et al.*, "Conditional generative adversarial and convolutional networks for x-ray breast mass segmentation and shape classification," in *International Conference on Medical Image Computing and Computer-Assisted Intervention*. Springer, 2018, pp. 833–840.

[143] L. de Oliveira Martins, G. B. Junior, E. C. da Silva, A. C. Silva, and A. C. de Paiva, "Classification of breast tissues in mammogram images using ripley's k function and support vector machine," in *International Conference Image Analysis and Recognition*. Springer, 2007, pp. 899–910.

[144] M. Samulski, N. Karssemeijer, P. Lucas, and P. Groot, "Classification of mammographic masses using support vector machines and bayesian networks," in *Medical Imaging 2007: Computer-Aided Diagnosis*, vol. 6514. International Society for Optics and Photonics, 2007, p. 65141J.

[145] F. Moayedi, Z. Azimifar, R. Boostani, and S. Katebi, "Contourlet-based mammography mass classification," in *International Conference Image Analysis and Recognition*. Springer, 2007, pp. 923–934.

[146] D. Davies and D. Dance, "Automatic computer detection of clustered calcifications in digital mammograms," *Physics in Medicine & Biology*, vol. 35, no. 8, p. 1111, 1990.

[147] C.-H. Wei and C.-T. Li, "Calcification descriptor and relevance feedback learning algorithms for content-based mammogram retrieval," in *International Workshop on Digital Mammography*. Springer, 2006, pp. 307–314.

[148] X. Zhang, "A new ensemble learning approach for microcalcification clusters detection." *JSW*, vol. 4, no. 9, pp. 1014–1021, 2009.

[149] H.-D. Cheng and J. Wang, "Fuzzy logic and scale space approach to microcalcification detection," in *2003 IEEE International Conference on Acoustics, Speech, and Signal Processing, 2003. Proceedings.(ICASSP'03).*, vol. 2. IEEE, 2003, pp. II–345.

[150] S. Oporto-Díaz, R. Hernández-Cisneros, and H. Terashima-Marín, "Detection of microcalcification clusters in mammograms using a difference of optimized gaussian filters," in *International Conference Image Analysis and Recognition*. Springer, 2005, pp. 998–1005.

[151] H. Soltanian-Zadeh, F. Rafiee-Rad *et al.*, "Comparison of multiwavelet, wavelet, haralick, and shape features for microcalcification classification in mammograms," *Pattern recognition*, vol. 37, no. 10, pp. 1973–1986, 2004.

[152] L. Wei, Y. Yang, and R. M. Nishikawa, "Microcalcification classification assisted by content-based image retrieval for breast cancer diagnosis," *Pattern recognition*, vol. 42, no. 6, pp. 1126–1132, 2009.

[153] densebreast info.org, "dense breast," https://densebreastinfo.org/legislation.aspx, visited on May 02,2020.

[154] J. N. Wolfe, "Risk for breast cancer development determined by mammographic parenchymal pattern," *Cancer*, vol. 37, no. 5, pp. 2486–2492, 1976.

[155] L. Tabár and P. B. Dean, "Mammographic parenchymal patterns: risk indicator for breast cancer?" *Jama*, vol. 247, no. 2, pp. 185–189, 1982.

[156] A. C. of Radiology *et al.*, "Breast imaging reporting and data system," *BI-RADS*, 2003.

[157] A.-E. Hassanien and F. Tolba, *Applications of Intelligent Optimization in Biology and Medicine*. Springer, 2016.

[158] N. Karssemeijer, "Automated classification of parenchymal patterns in mammograms," *Physics in medicine & biology*, vol. 43, no. 2, p. 365, 1998.

[159] K. Bovis and S. Singh, "Classification of mammographic breast density using a combined classifier paradigm," in *4th international workshop on digital mammography*, 2002, pp. 177–180.

[160] S. Petroudi, T. Kadir, and M. Brady, "Automatic classification of mammographic parenchymal patterns: A statistical approach," in *Proceedings of the 25th Annual International Conference of the IEEE Engineering in Medicine and Biology Society (IEEE Cat. No. 03CH37439)*, vol. 1. IEEE, 2003, pp. 798–801.

[161] A. Oliver, J. Freixenet, and R. Zwiggelaar, "Automatic classification of breast density," in *IEEE International Conference on Image Processing 2005*, vol. 2. IEEE, 2005, pp. II–1258.

[162] A. Bosch, X. Munoz, A. Oliver, and J. Marti, "Modeling and classifying breast tissue density in mammograms," in *2006 IEEE Computer Society Conference on Computer Vision and Pattern Recognition (CVPR'06)*, vol. 2. IEEE, 2006, pp. 1552–1558.

[163] C. Castella, K. Kinkel, M. P. Eckstein, P.-E. Sottas, F. R. Verdun, and F. O. Bochud, "Semiautomatic mammographic parenchymal patterns classification using multiple statistical features," *Academic radiology*, vol. 14, no. 12, pp. 1486–1499, 2007.

[164] A. Oliver, J. Freixenet, R. Marti, J. Pont, E. Pérez, E. R. Denton, and R. Zwiggelaar, "A novel breast tissue density classification methodology," *IEEE Transactions on Information Technology in Biomedicine*, vol. 12, no. 1, pp. 55–65, 2008.

[165] Q. Liu, L. Liu, Y. Tan, J. Wang, X. Ma, and H. Ni, "Mammogram density estimation using sub-region classification," in *2011 4th International Conference on Biomedical Engineering and Informatics (BMEI)*, vol. 1. IEEE, 2011, pp. 356–359.

[166] Z. Chen, E. Denton, and R. Zwiggelaar, "Local feature based mammographic tissue pattern modelling and breast density classification," in *2011 4th International Conference on Biomedical Engineering and Informatics (BMEI)*, vol. 1. IEEE, 2011, pp. 351–355.

[167] M. Muštra, M. Grgić, and K. Delač, "Breast density classification using multiple feature selection," *automatika*, vol. 53, no. 4, pp. 362–372, 2012.

[168] A. D. Masmoudi, N. G. B. Ayed, D. S. Masmoudi, and R. Abid, "Lbpv descriptors-based automatic acr/birads classification approach," *EURASIP Journal on Image and Video Processing*, vol. 2013, no. 1, p. 19, 2013.

[169] Kriti, J. Virmani, N. Dey, V. Kumar *et al.*, "Pca-pnn and pca-svm based cad systems for breast density classification," in *Applications of intelligent optimization in biology and medicine*. Springer, 2016, pp. 159–180.

[170] J. Virmani and Kriti, "Breast tissue density classification using wavelet-based texture descriptors," in *Proceedings of the Second International Conference on Computer and Communication Technologies*. Springer, 2016, pp. 539–546.

[171] C. K. Ahn, C. Heo, H. Jin, and J. H. Kim, "A novel deep learning-based approach to high accuracy breast density estimation in digital mammography," in *Medical Imaging 2017: Computer-Aided Diagnosis*, vol. 10134. International Society for Optics and Photonics, 2017, p. 101342O.

[172] J. Xu, C. Li, Y. Zhou, L. Mou, H. Zheng, and S. Wang, "Classifying mammographic breast density by residual learning," *arXiv preprint arXiv:1809.10241*, 2018.

[173] A. A. Mohamed, W. A. Berg, H. Peng, Y. Luo, R. C. Jankowitz, and S. Wu, "A deep learning method for classifying mammographic breast density categories," *Medical physics*, vol. 45, no. 1, pp. 314–321, 2018.

[174] N. Wu, K. J. Geras, Y. Shen, J. Su, S. G. Kim, E. Kim, S. Wolfson, L. Moy, and K. Cho, "Breast density classification with deep convolutional neural networks," in *2018 IEEE International Conference on Acoustics, Speech and Signal Processing (ICASSP)*. IEEE, 2018, pp. 6682–6686.

[175] A. A. Samah, M. F. A. Fauzi, and S. Mansor, "Classification of benign and malignant tumors in histopathology images," in *2017 IEEE International Conference on Signal and Image Processing Applications (ICSIPA)*. IEEE, 2017, pp. 102–106.

[176] N. H. Motlagh, M. Jannesary, H. Aboulkheyr, P. Khosravi, O. Elemento, M. Totonchi, and I. Hajirasouliha, "Breast cancer histopathological image classification: A deep learning approach," *bioRxiv*, p. 242818, 2018.

[177] Z. Gandomkar, P. C. Brennan, and C. Mello-Thoms, "Mudern: Multi-category classification of breast histopathological image using deep residual networks," *Artificial intelligence in medicine*, vol. 88, pp. 14–24, 2018.

[178] K. H. Allison, L. M. Reisch, P. A. Carney, D. L. Weaver, S. J. Schnitt, F. P. O'Malley, B. M. Geller, and J. G. Elmore, "Understanding diagnostic variability in breast pathology: lessons learned from an expert consensus review panel," *Histopathology*, vol. 65, no. 2, pp. 240–251, 2014.

[179] B. Weyn, G. Van De Wouwer, A. Van Daele, P. Scheunders, D. Van Dyck, E. Van Marck, and W. Jacob, "Automated breast tumor diagnosis and grading based on wavelet chromatin texture description," *Cytometry: The Journal of the International Society for Analytical Cytology*, vol. 33, no. 1, pp. 32–40, 1998.

[180] M. Kowal, P. Filipczuk, A. Obuchowicz, J. Korbicz, and R. Monczak, "Computer-aided diagnosis of breast cancer based on fine needle biopsy microscopic images," *Computers in biology and medicine*, vol. 43, no. 10, pp. 1563–1572, 2013.

[181] S. Naik, S. Doyle, S. Agner, A. Madabhushi, M. Feldman, and J. Tomaszewski, "Automated gland and nuclei segmentation for grading of prostate and breast cancer histopathology," in *2008 5th IEEE International Symposium on Biomedical Imaging: From Nano to Macro*. IEEE, 2008, pp. 284–287.

[182] M. M. Dundar, S. Badve, G. Bilgin, V. Raykar, R. Jain, O. Sertel, and M. N. Gurcan, "Computerized classification of intraductal breast lesions using histopathological images," *IEEE Transactions on Biomedical Engineering*, vol. 58, no. 7, pp. 1977–1984, 2011.

[183] F. Dong, H. Irshad, E.-Y. Oh, M. F. Lerwill, E. F. Brachtel, N. C. Jones, N. W. Knoblauch, L. Montaser-Kouhsari, N. B. Johnson, L. K. Rao *et al.*, "Computational pathology to discriminate benign from malignant intraductal proliferations of the breast," *PloS one*, vol. 9, no. 12, 2014.

[184] J. Xu, L. Xiang, Q. Liu, H. Gilmore, J. Wu, J. Tang, and A. Madabhushi, "Stacked sparse autoencoder (ssae) for nuclei detection on breast cancer histopathology images," *IEEE transactions on medical imaging*, vol. 35, no. 1, pp. 119–130, 2015.

[185] Y. Zheng, Z. Jiang, F. Xie, H. Zhang, Y. Ma, H. Shi, and Y. Zhao, "Feature extraction from histopathological images based on nucleus-guided convolutional neural network for breast lesion classification," *Pattern Recognition*, vol. 71, pp. 14–25, 2017.

[186] D. C. Cireşan, A. Giusti, L. M. Gambardella, and J. Schmidhuber, "Mitosis detection in breast cancer histology images with deep neural networks," in *International conference on medical image computing and computer-assisted intervention*. Springer, 2013, pp. 411–418.

[187] S. Albarqouni, C. Baur, F. Achilles, V. Belagiannis, S. Demirci, and N. Navab, "Aggnet: deep learning from crowds for mitosis detection in breast cancer histology images," *IEEE transactions on medical imaging*, vol. 35, no. 5, pp. 1313–1321, 2016.

[188] H. Wang, A. C. Roa, A. N. Basavanhally, H. L. Gilmore, N. Shih, M. Feldman, J. Tomaszewski, F. Gonzalez, and A. Madabhushi, "Mitosis detection in breast cancer pathology images by combining handcrafted and convolutional neural network features," *Journal of Medical Imaging*, vol. 1, no. 3, p. 034003, 2014.

[189] D. O. T. Bruno, M. Z. do Nascimento, R. P. Ramos, V. R. Batista, L. A. Neves, and A. S. Martins, "Lbp operators on curvelet coefficients as an algorithm to describe texture in breast cancer tissues," *Expert Systems with Applications*, vol. 55, pp. 329–340, 2016.

[190] M. Balazsi, P. Blanco, P. Zoroquiain, M. D. Levine, and M. N. Burnier, "Invasive ductal breast carcinoma detector that is robust to image magnification in whole digital slides," *Journal of Medical Imaging*, vol. 3, no. 2, p. 027501, 2016.

[191] A. Cruz-Roa, A. Basavanhally, F. González, H. Gilmore, M. Feldman, S. Ganesan, N. Shih, J. Tomaszewski, and A. Madabhushi, "Automatic detection of invasive ductal carcinoma in whole slide images with convolutional neural networks," in *Medical Imaging 2014: Digital Pathology*, vol. 9041. International Society for Optics and Photonics, 2014, p. 904103.

[192] F. A. Spanhol, L. S. Oliveira, P. R. Cavalin, C. Petitjean, and L. Heutte, "Deep features for breast cancer histopathological image classification," in *2017 IEEE International Conference on Systems, Man, and Cybernetics (SMC)*. IEEE, 2017, pp. 1868–1873.

[193] S. Doyle, S. Agner, A. Madabhushi, M. Feldman, and J. Tomaszewski, "Automated grading of breast cancer histopathology using spectral clustering with textural and architectural image features," in *2008 5th IEEE International Symposium on Biomedical Imaging: From Nano to Macro*. IEEE, 2008, pp. 496–499.

[194] B. E. Bejnordi, G. Zuidhof, M. Balkenhol, M. Hermsen, P. Bult, B. van Ginneken, N. Karssemeijer, G. Litjens, and J. van der Laak, "Context-aware stacked convolutional neural networks for classification of breast carcinomas in whole-slide histopathology images," *Journal of Medical Imaging*, vol. 4, no. 4, p. 044504, 2017.

[195] F. A. Spanhol, L. S. Oliveira, C. Petitjean, and L. Heutte, "Breast cancer histopathological image classification using convolutional neural networks," in *2016 international joint conference on neural networks (IJCNN)*. IEEE, 2016, pp. 2560–2567.

[196] N. Bayramoglu, J. Kannala, and J. Heikkilä, "Deep learning for magnification independent breast cancer histopathology image classification," in *2016 23rd International conference on pattern recognition (ICPR)*. IEEE, 2016, pp. 2440–2445.

[197] J. Sun and A. Binder, "Comparison of deep learning architectures for h&e histopathology images," in *2017 IEEE Conference on Big Data and Analytics (ICBDA)*. IEEE, 2017, pp. 43–48.

[198] Y. Song, J. J. Zou, H. Chang, and W. Cai, "Adapting fisher vectors for histopathology image classification," in *2017 IEEE 14th International Symposium on Biomedical Imaging (ISBI 2017)*. IEEE, 2017, pp. 600–603.

[199] Z. Han, B. Wei, Y. Zheng, Y. Yin, K. Li, and S. Li, "Breast cancer multi-classification from histopathological images with structured deep learning model," *Scientific reports*, vol. 7, no. 1, pp. 1–10, 2017.

[200] E. M. Nejad, L. S. Affendey, R. B. Latip, and I. Bin Ishak, "Classification of histopathology images of breast into benign and malignant using a single-layer convolutional neural network," in *Proceedings of the International Conference on Imaging, Signal Processing and Communication*, 2017, pp. 50–53.

[201] M. Sharma, R. Singh, and M. Bhattacharya, "Classification of breast tumors as benign and malignant using textural feature descriptor," in *2017 IEEE International Conference on Bioinformatics and Biomedicine (BIBM)*. IEEE, 2017, pp. 1110–1113.

[202] W. Zhi, H. W. F. Yueng, Z. Chen, S. M. Zandavi, Z. Lu, and Y. Y. Chung, "Using transfer learning with convolutional neural networks to diagnose breast cancer from histopathological images," in *International Conference on Neural Information Processing*. Springer, 2017, pp. 669–676.

[203] S. Cascianelli, R. Bello-Cerezo, F. Bianconi, M. L. Fravolini, M. Belal, B. Palumbo, and J. N. Kather, "Dimensionality reduction strategies for cnn-based classification of histopathological images," in *International Conference on Intelligent Interactive Multimedia Systems and Services*. Springer, 2018, pp. 21–30.

[204] E. M. Nejad, L. S. Affendey, R. B. Latip, I. B. Ishak, and R. Banaeeyan, "Transferred semantic scores for scalable retrieval of histopathological breast cancer images," *International Journal of Multimedia Information Retrieval*, vol. 7, no. 4, pp. 241–249, 2018.

[205] Y. Benhammou, S. Tabik, B. Achchab, and F. Herrera, "A first study exploring the performance of the state-of-the art cnn model in the problem of breast cancer," in *Proceedings of the International Conference on Learning and Optimization Algorithms: Theory and Applications*, 2018, pp. 1–6.

[206] Y. Song, H. Chang, Y. Gao, S. Liu, D. Zhang, J. Yao, W. Chrzanowski, and W. Cai, "Feature learning with component selective encoding for histopathology image classification," in *2018 IEEE 15th International Symposium on Biomedical Imaging (ISBI 2018)*. IEEE, 2018, pp. 257–260.

[207] D. Sanchez-Morillo, J. González, M. García-Rojo, and J. Ortega, "Classification of breast cancer histopathological images using kaze features," in *International Conference on Bioinformatics and Biomedical Engineering*. Springer, 2018, pp. 276–286.

[208] K. Kumar and A. C. S. Rao, "Breast cancer classification of image using convolutional neural network," in *2018 4th International Conference on Recent Advances in Information Technology (RAIT)*. IEEE, 2018, pp. 1–6.

[209] P. Alirezazadeh, B. Hejrati, A. Monsef-Esfahani, and A. Fathi, "Representation learning-based unsupervised domain adaptation for classification of breast cancer histopathology images," *Biocybernetics and Biomedical Engineering*, vol. 38, no. 3, pp. 671–683, 2018.

[210] A.-A. Nahid, M. A. Mehrabi, and Y. Kong, "Histopathological breast cancer image classification by deep neural network techniques guided by local clustering," *BioMed research international*, vol. 2018, 2018.

[211] P. Sudharshan, C. Petitjean, F. Spanhol, L. E. Oliveira, L. Heutte, and P. Honeine, "Multiple instance learning for histopathological breast cancer image classification," *Expert Systems with Applications*, vol. 117, pp. 103–111, 2019.

[212] C. Zhu, F. Song, Y. Wang, H. Dong, Y. Guo, and J. Liu, "Breast cancer histopathology image classification through assembling multiple compact cnns," *BMC medical informatics and decision making*, vol. 19, no. 1, p. 198, 2019.

[213] T. Ojala, M. Pietikainen, and T. Maenpaa, "Multiresolution gray-scale and rotation invariant texture classification with local binary patterns," *IEEE Transactions on pattern analysis and machine intelligence*, vol. 24, no. 7, pp. 971–987, 2002.

[214] Z. Guo, L. Zhang, and D. Zhang, "A completed modeling of local binary pattern operator for texture classification," *IEEE transactions on image processing*, vol. 19, no. 6, pp. 1657–1663, 2010.

[215] V. Ojansivu and J. Heikkilä, "Blur insensitive texture classification using local phase quantization," in *International conference on image and signal processing*. Springer, 2008, pp. 236–243.

[216] R. M. Haralick, K. Shanmugam, and I. H. Dinstein, "Textural features for image classification," *IEEE Transactions on systems, man, and cybernetics*, no. 6, pp. 610–621, 1973.

[217] N. A. Hamilton, R. S. Pantelic, K. Hanson, and R. D. Teasdale, "Fast automated cell phenotype image classification," *BMC bioinformatics*, vol. 8, no. 1, p. 110, 2007.

[218] E. Rublee, V. Rabaud, K. Konolige, and G. Bradski, "Orb: An efficient alternative to sift or surf," in *2011 International conference on computer vision*. Ieee, 2011, pp. 2564–2571.

[219] M. Ringnér, "What is principal component analysis?" *Nature biotechnology*, vol. 26, no. 3, pp. 303–304, 2008.

[220] E. Bingham and H. Mannila, "Random projection in dimensionality reduction: applications to image and text data," in *Proceedings of the seventh ACM SIGKDD international conference on Knowledge discovery and data mining*, 2001, pp. 245–250.

[221] K. Michalak and H. Kwasnicka, "Correlation based feature selection method," *International Journal of Bio-Inspired Computation*, vol. 2, no. 5, pp. 319–332, 2010.

[222] S. Escalera, O. Pujol, and P. Radeva, "Separability of ternary codes for sparse designs of error-correcting output codes," *Pattern Recognition Letters*, vol. 30, no. 3, pp. 285–297, 2009.

[223] P. F. Alcantarilla, A. Bartoli, and A. J. Davison, "Kaze features," in *European Conference on Computer Vision*. Springer, 2012, pp. 214–227.

[224] R. Venkatesan, P. Chandakkar, and B. Li, "Simpler non-parametric methods provide as good or better results to multiple-instance learning," in *Proceedings of the IEEE International Conference on Computer Vision*, 2015, pp. 2605–2613.

[225] S. S. Chennamsetty, M. Safwan, and V. Alex, "Classification of breast cancer histology image using ensemble of pre-trained neural networks," in *International conference image analysis and recognition*. Springer, 2018, pp. 804–811.

[226] S. Kwok, "Multiclass classification of breast cancer in whole-slide images," in *International conference image analysis and recognition*. Springer, 2018, pp. 931–940.

[227] N. Brancati, M. Frucci, and D. Riccio, "Multi-classification of breast cancer histology images by using a fine-tuning strategy," in *International conference image analysis and recognition*. Springer, 2018, pp. 771–778.

[228] B. Marami, M. Prastawa, M. Chan, M. Donovan, G. Fernandez, and J. Zeineh, "Ensemble network for region identification in breast histopathology slides," in *International Conference Image Analysis and Recognition*. Springer, 2018, pp. 861–868.

[229] M. Kohl, C. Walz, F. Ludwig, S. Braunewell, and M. Baust, "Assessment of breast cancer histology using densely connected convolutional networks," in *International Conference Image Analysis and Recognition*. Springer, 2018, pp. 903–913.

[230] Y. Wang, L. Sun, K. Ma, and J. Fang, "Breast cancer microscope image classification based on cnn with image deformation," in *International Conference Image Analysis and Recognition*. Springer, 2018, pp. 845–852.

[231] I. Koné and L. Boulmane, "Hierarchical resnext models for breast cancer histology image classification," in *International Conference Image Analysis and Recognition*. Springer, 2018, pp. 796–803.

[232] World-Health-Organization, "Cancer," https://www.who.int/news-room/fact-sheets/detail/cancer, visited on April 16,2020.

[233] cancer.org, "Key statistics about liver cancer," https://www.cancer.org/cancer/liver-cancer/about/what-is-key-statistics.html, visited on April 16,2020.

[234] cancer.net, "Liver cancer: Statistics," https://www.cancer.net/cancer-types/liver-cancer/statistics, visited on April 16,2020.

[235] radlex.org, "radlex," http://radlex.org/, visited on April 16,2020.

[236] L.-K. Soh and C. Tsatsoulis, "Texture analysis of sar sea ice imagery using gray level co-occurrence matrices," *IEEE Transactions on geoscience and remote sensing*, vol. 37, no. 2, pp. 780–795, 1999.

[237] C. Liu and H. Wechsler, "Gabor feature based classification using the enhanced fisher linear discriminant model for face recognition," *IEEE Transactions on Image processing*, vol. 11, no. 4, pp. 467–476, 2002.

[238] G. Zhang, Z. Ma, and L. Deng, "Texture feature extraction and description using fuzzy set of main dominant directions of variable scales in content-based medical image retrieval," in *Proceedings of the 2008 ACM symposium on Applied computing*, 2008, pp. 1760–1761.

[239] A. Vadivel and B. Surendiran, "A fuzzy rule-based approach for characterization of mammogram masses into bi-rads shape categories," *Computers in biology and medicine*, vol. 43, no. 4, pp. 259–267, 2013.

[240] L. Breiman, "Random forests machine learning, vol. 45," 2001.

[241] J. Daugman, "How iris recognition works," in *The essential guide to image processing*. Elsevier, 2009, pp. 715–739.

[242] N. E. Huang, Z. Shen, S. R. Long, M. C. Wu, H. H. Shih, Q. Zheng, N.-C. Yen, C. C. Tung, and H. H. Liu, "The empirical mode decomposition and the hilbert spectrum for nonlinear and non-stationary time series analysis," *Proceedings of the Royal Society of London. Series A: mathematical, physical and engineering sciences*, vol. 454, no. 1971, pp. 903–995, 1998.

[243] J. C. Nunes, Y. Bouaoune, E. Delechelle, O. Niang, and P. Bunel, "Image analysis by bidimensional empirical mode decomposition," *Image and vision computing*, vol. 21, no. 12, pp. 1019–1026, 2003.

[244] N. B. Marvasti, N. Kökciyan, R. Türkay, A. Yazıcı, P. Yolum, S. Uskudarli, and B. Acar, "Overview of the imageclef 2015 liver ct annotation task." in *CLEF (Working Notes)-http://ceur-ws.org/Vol-1180/*, 2014.

[245] WomensHealthMatters, "Breast cancer," https://www.womenshealthmatters.ca/health-centres/breast-cancer-info-reviewed-by-doctors-research-treatment-symptoms-and-amp-diagnosis/, visited on May 06,2020.

[246] N. V. Chawla, K. W. Bowyer, L. O. Hall, and W. P. Kegelmeyer, "Smote: synthetic minority over-sampling technique," *Journal of artificial intelligence research*, vol. 16, pp. 321–357, 2002.

[247] A. J. Viera, J. M. Garrett *et al.*, "Understanding interobserver agreement: the kappa statistic," *Fam med*, vol. 37, no. 5, pp. 360–363, 2005.

[248] UCI-Repository, "Uci-machine-learning-repository," http://archive.ics.uci.edu/ml/index.php, visited on May 06,2020.

[249] F. Rosenblatt, "Principles of neurodynamics. perceptrons and the theory of brain mechanisms," Cornell Aeronautical Lab Inc Buffalo NY, Tech. Rep., 1961.

[250] G. John and P. Langley, "Estimating continuous distributions in bayesian classifiers. in proceedings of the eleventh conference on uncertainty in artificial intelligence," pp. 338–345, 1995.

[251] M. Heath, K. Bowyer, D. Kopans, R. Moore, and P. Kegelmeyer, "The digital database for screening mammography. in m. yaffe, editor, fifth international workshop on digital mammography," pp. 457–460, 2000.

[252] P. SUCKLING J, "The mammographic image analysis society digital mammogram database," *Digital Mammo*, pp. 375–386, 1994.

[253] Z. Chen, E. Denton, and R. Zwiggelaar, "Local feature based mammographic tissue pattern modelling and breast density classification," in *2011 4th International Conference on Biomedical Engineering and Informatics (BMEI)*, vol. 1. IEEE, 2011, pp. 351–355.

[254] K. J. Wang and A. M. Adrian, "Breast cancer classification using hybrid synthetic minority over-sampling technique and artificial immune recognition system algorithm," *Int J Comput Sci Electron Eng (IJCSEE)*, vol. 1, no. 3, pp. 408–412, 2013.

[255] A. J. Tallón-Ballesteros, C. Hervás-Martínez, J. C. Riquelme, and R. Ruiz, "Feature selection to enhance a two-stage evolutionary algorithm in product unit neural networks for complex classification problems," *Neurocomputing*, vol. 114, pp. 107–117, 2013.

[256] R. G. Mantovani, A. L. Rossi, J. Vanschoren, B. Bischl, and A. C. De Carvalho, "Effectiveness of random search in svm hyper-parameter tuning," in *2015 International Joint Conference on Neural Networks (IJCNN)*. Ieee, 2015, pp. 1–8.

[257] S. Belarouci, S. Bouchikhi, and M. A. Chikh, "Comparative study of balancing methods: case of imbalanced medical data," *International Journal of Biomedical Engineering and Technology*, vol. 21, no. 3, pp. 247–263, 2016.

[258] I. Nedjar, S. Mahmoudi, and M. A. Chikh, "A topological approach for mammographic density classification using a modified synthetic minority over-sampling technique algorithm," *International Journal of Biomedical Engineering and Technology*, Forthcoming article.

[259] J. N. Wolfe, "Breast patterns as an index of risk for developing breast cancer," *American Journal of Roentgenology*, vol. 126, no. 6, pp. 1130–1137, 1976.

[260] N. F. Boyd, G. A. Lockwood, J. W. Byng, D. L. Tritchler, and M. J. Yaffe, "Mammographic densities and breast cancer risk." *Cancer Epidemiology and Prevention Biomarkers*, vol. 7, no. 12, pp. 1133–1144, 1998.

[261] I. Nedjar, S. Mahmoudi, and M. A. Chikh, "Topological methods for mammographic images classification: The digital mammography dream challenge 2017," in *11th annual RECOMB/ISCB Conference on Regulatory & Systems Genomics, New York, USA*, 2018.

[262] F. Melo, "Receiver operating characteristic (roc) curve," *Springer NY*, vol. 67, pp. 1818–1823, 2013.

[263] Y. Nikulin, "Digital mammography dream challenge: Participant experience 1 (conference presentation)," in *Medical Imaging 2017: Computer-Aided Diagnosis*, vol. 10134. International Society for Optics and Photonics, 2017, p. 101344J.

[264] D. Ribli, A. Horváth, Z. Unger, P. Pollner, and I. Csabai, "Detecting and classifying lesions in mammograms with deep learning," *Scientific reports*, vol. 8, no. 1, pp. 1–7, 2018.

[265] Asianscientist, "Three invaluable lessons for building healthcare ai," https://www.asianscientist.com/2018/07/features/sginnovate-mornin-feng-healthcare-ai/, visited on May 29,2020.

[266] I. B. A. TURING, "Computing machinery and intelligence-am turing," *Mind*, vol. 59, no. 236, p. 433, 1950.

[267] S. Soni, "Applications of anns in stock market prediction: a survey," *International Journal of Computer Science & Engineering Technology*, vol. 2, no. 3, pp. 71–83, 2011.

[268] W. McCulloch and W. Pitts, "A logical calculus of the ideas immanent in nervous activity," . *Bulletin of Mathematical Biophysics*, vol. 5, no. 4, pp. 115—133, 1943.

[269] J. Von Neumann, *The computer and the brain*. New Haven/London: Yale Univesity Press, 1958.

[270] J. Gasteiger and J. Zupan, "Neural networks in chemistry," *Angewandte Chemie International Edition in English*, vol. 32, no. 4, pp. 503–527, 1993.

[271] F. Rosenblatt, "The perceptron: a probabilistic model for information storage and organization in the brain." *Psychological review*, vol. 65, no. 6, p. 386, 1958.

[272] M. Minsky and S. Papert, "An introduction to computational geometry," *Cambridge tiass., HIT*, 1969.

[273] D. E. Rumelhart, G. E. Hinton, and R. J. Williams, "Learning representations by back-propagating errors," *nature*, vol. 323, no. 6088, pp. 533–536, 1986.

[274] H. J. Kelley, "Gradient theory of optimal flight paths," *Ars Journal*, vol. 30, no. 10, pp. 947–954, 1960.

[275] S. E. Dreyfus, "The numerical solution of variational problems," *Journal of Mathematical Analysis and Applications*, vol. 5, no. 1, pp. 30–45, 1962.

[276] S. Linnainmaa, "The representation of the cumulative rounding error of an algorithm as a taylor expansion of the local rounding errors," *Master's Thesis (in Finnish), Univ. Helsinki*, pp. 6–7, 1970.

[277] A. G. Ivakhnenko, "Polynomial theory of complex systems," *IEEE Transactions on Systems, Man, and Cybernetics*, vol. SMC-1, no. 4, pp. 364–378, 1971.

[278] K. Fukushima, S. Miyake, and T. Ito, "Neocognitron: A self-organizing neural network model for a mechanism of pattern recognition unaffected by shift in position," *Biological Cybernetics*, vol. 36, pp. 93–202, 1980.

[279] Y. LeCun *et al.*, "Generalization and network design strategies. connectionism in perspective," *Zurich, Switzerland, Elsiever*, 1989.

[280] S. Hochreiter, "Untersuchungen zu dynamischen neuronalen netzen," *Diploma, Technische Universität München*, vol. 91, no. 1, 1991.

[281] J. Schmidhuber, "Learning complex, extended sequences using the principle of history compression," *Neural Computation*, vol. 4, no. 2, pp. 234–242, 1992.

[282] S. Hochreiter and J. Schmidhuber, "Long short-term memory," *Neural computation*, vol. 9, no. 8, pp. 1735–1780, 1997.

[283] X. Glorot, A. Bordes, and Y. Bengio, "Deep sparse rectifier neural networks," in *Proceedings of the fourteenth international conference on artificial intelligence and statistics*, 2011, pp. 315–323.

[284] A. Krizhevsky, I. Sutskever, and G. Hinton, "Imagenet classification with deep convolutional neural networks," *Advances in neural information processing systems*, vol. 25, no. 2, 2012.

[285] Y. LeCun, L. Bottou, Y. Bengio, and P. Haffner, "Gradient-based learning applied to document recognition," *Proceedings of the IEEE*, vol. 86, no. 11, pp. 2278–2324, 1998.

[286] Y. LeCun, B. Boser, J. S. Denker, D. Henderson, R. E. Howard, W. Hubbard, and L. D. Jackel, "Backpropagation applied to handwritten zip code recognition," *Neural computation*, vol. 1, no. 4, pp. 541–551, 1989.

[287] A. Rosebrock, *Deep Learning for Computer Vision*. PyImageSearch, 2017.

[288] K. Simonyan and A. Zisserman, "Very deep convolutional networks for large-scale image recognition," *arXiv preprint arXiv:1409.1556*, 2014.

[289] C. Szegedy, W. Liu, Y. Jia, P. Sermanet, S. Reed, D. Anguelov, D. Erhan, V. Vanhoucke, and A. Rabinovich, "Going deeper with convolutions," in *Proceedings of the IEEE conference on computer vision and pattern recognition*, 2015, pp. 1–9.

[290] C. Szegedy, V. Vanhoucke, S. Ioffe, J. Shlens, and Z. Wojna, "Rethinking the inception architecture for computer vision," in *Proceedings of the IEEE conference on computer vision and pattern recognition*, 2016, pp. 2818–2826.

[291] K. He, X. Zhang, S. Ren, and J. Sun, "Deep residual learning for image recognition," in *Proceedings of the IEEE conference on computer vision and pattern recognition*, 2016, pp. 770–778.

[292] F. Chollet, "Xception: Deep learning with depthwise separable convolutions," in *Proceedings of the IEEE conference on computer vision and pattern recognition*, 2017, pp. 1251–1258.

[293] L. Sifre and S. Mallat, "Rigid-motion scattering for image classification," *Ph. D. thesis*, 2014.

[294] G. Huang, Z. Liu, L. Van Der Maaten, and K. Q. Weinberger, "Densely connected convolutional networks," in *Proceedings of the IEEE conference on computer vision and pattern recognition*, 2017, pp. 4700–4708.

[295] A. G. Howard, M. Zhu, B. Chen, D. Kalenichenko, W. Wang, T. Weyand, M. Andreetto, and H. Adam, "Mobilenets: Efficient convolutional neural networks for mobile vision applications," *arXiv preprint arXiv:1704.04861*, 2017.

[296] M. Sandler, A. Howard, M. Zhu, A. Zhmoginov, and L. Chen, "Mobilenetv2: Inverted residuals and linear bottlenecks," in *2018 IEEE/CVF Conference on Computer Vision and Pattern Recognition*, 2018, pp. 4510–4520.

[297] M. Tan and Q. V. Le, "Efficientnet: Rethinking model scaling for convolutional neural networks," *arXiv preprint arXiv:1905.11946*, 2019.

[298] Q. Xie, E. Hovy, M.-T. Luong, and Q. V. Le, "Self-training with noisy student improves imagenet classification," *arXiv preprint arXiv:1911.04252*, 2019.

[299] I. Nedjar, S. Mahmoudi, and M. Chikh, "lassification of breast cancer histology images using consensus oriented by three deep convolutional neural networks," *International Journal of Computer Assisted Radiology and Surgery*, vol. 14, no. Suppl 1, p. S1–S194, 2019.

[300] Z. Wang, N. Dong, W. Dai, S. D. Rosario, and E. P. Xing, "Classification of breast cancer histopathological images using convolutional neural networks with hierarchical loss and global pooling," in *International Conference Image Analysis and Recognition*. Springer, 2018, pp. 745–753.

[301] H. Cao, S. Bernard, L. Heutte, and R. Sabourin, "Improve the performance of transfer learning without fine-tuning using dissimilarity-based multi-view learning for breast cancer histology images," in *International conference image analysis and recognition*. Springer, 2018, pp. 779–787.

[302] Y. Guo, H. Dong, F. Song, C. Zhu, and J. Liu, "Breast cancer histology image classification based on deep neural networks," in *International Conference Image Analysis and Recognition*. Springer, 2018, pp. 827–836.

[303] A. Mahbod, I. Ellinger, R. Ecker, Ö. Smedby, and C. Wang, "Breast cancer histological image classification using fine-tuned deep network fusion," in *International Conference Image Analysis and Recognition*. Springer, 2018, pp. 754–762.

[304] C. A. Ferreira, T. Melo, P. Sousa, M. I. Meyer, E. Shakibapour, P. Costa, and A. Campilho, "Classification of breast cancer histology images through transfer learning using a pre-trained inception resnet v2," in *International Conference Image Analysis and Recognition*. Springer, 2018, pp. 763–770.

[305] A. Pimkin, G. Makarchuk, V. Kondratenko, M. Pisov, E. Krivov, and M. Belyaev, "Ensembling neural networks for digital pathology images classification and segmentation," in *International Conference Image Analysis and Recognition*. Springer, 2018, pp. 877–886.

[306] A. Rakhlin, A. Shvets, V. Iglovikov, and A. A. Kalinin, "Deep convolutional neural networks for breast cancer histology image analysis," in *International Conference Image Analysis and Recognition*. Springer, 2018, pp. 737–744.

[307] T. Iesmantas and R. Alzbutas, "Convolutional capsule network for classification of breast cancer histology images," in *International Conference Image Analysis and Recognition*. Springer, 2018, pp. 853–860.

[308] N. Weiss, H. Kost, and A. Homeyer, "Towards interactive breast tumor classification using transfer learning," in *International Conference Image Analysis and Recognition*. Springer, 2018, pp. 727–736.

[309] R. Awan, N. A. Koohbanani, M. Shaban, A. Lisowska, and N. Rajpoot, "Context-aware learning using transferable features for classification of breast cancer histology images," in *International Conference Image Analysis and Recognition*. Springer, 2018, pp. 788–795.

[310] S. Galal and V. Sanchez-Freire, "Candy cane: Breast cancer pixel-wise labeling with fully convolutional densenets," in *International Conference Image Analysis and Recognition*. Springer, 2018, pp. 820–826.

[311] Q. D. Vu, M. N. N. To, E. Kim, and J. T. Kwak, "Micro and macro breast histology image analysis by partial network re-use," in *International Conference Image Analysis and Recognition*. Springer, 2018, pp. 895–902.

Dissemination

Internationally indexed journals

1. Nedjar Imane, Dahou Mustafa El Habib, Settouti Nessma, Mahmoudi Saïd, Chikh Mohamed Amine, ”Random Forest Based Classification of Medical X-ray images using a genetic algorithm for feature selection”, In journal of Mechanics in Medicine and Biology Vol. 15, No. 02, 1540025,2015.

2. Nedjar Imane, Mahmoudi Saïd, Chikh Mohamed Amine, ”Content-based Medical Image Retrieval for Liver CT Annotation”, The Transactions on Machine Learning and Artificial Intelligence (TMLAI), Volume 5, No. 4, August 2017.

3. Lessage Xavier, Larhmam Mohamed, Mahmoudi Saïd, Nedjar Imane, ”Assessing Breast Cancer Screening using recent Deep Convolutional Neural Networks”, In International Journal of Computer Assisted Radiology and Surgery, Volume 13 (Suppl 1):S1–S273, June 2018, https://doi.org/10.1007/s11548-018-1766-y .

4. Nedjar Imane, Mahmoudi Saïd, Chikh Mohammed Amine, ”Classification of breast cancer histology images using consensus oriented by three Deep Convolutional Neural Networks”, In International Journal of Computer Assisted Radiology and Surgery, 14, 1, 81-82, 2019. DOI:10.1007/s11548-019-01969-3

5. Thomas Schaffter, Diana S. M. Buist, Christoph I. Lee, et al, ”Evaluation of Combined Artificial Intelligence and Radiologist Assessment to Interpret Screening Mammograms”, JAMA Netw Open. 3(3):e200265,2020 doi:10.1001/jamanetworkopen.2020.0265.

6. Nedjar Imane, Mahmoudi Saïd, Chikh Mohammed Amine, ”A topological approach for mammographic density classification using a modified synthetic minority over-sampling technique algorithm”, in International Journal of Biomedical Engineering and Technology (Forthcoming article, https://www.inderscience.com/info/ingeneral/forthcoming.php?jcode=ijbet)

Conferences

1. Nedjar Imane, Mahmoudi Saïd, Chikh Mohamed Amine, ”Content-based medical images classification”, International Conference on Signal, Image, Vision and their Applications, Guelma, Algeria, 2013.

2. Nedjar Imane, Mahmoudi Saïd, Chikh Mohamed Amine, ”Content-based medical images retrieval”, International Conference on Mechanics in Medicine and Biology, Bologna , Italy, 2014.

3. Nedjar Imane, Mahmoudi Saïd, Chikh Mohamed Amine, ”Annotation and retrieval approaches for medical images ”, La 4ème journée Doctorale de Génie Biologique et Médical, Tlemcen, 2014.

4. Nedjar Imane, Mahmoudi Saïd, Chikh Mohamed Amine, Abi-yad Khadidja, Bouafia Zohier, ”Automatic annotation of liver CT image: Imageclefmed 2015”, In: CLEF2015 Working Notes. CEUR Workshop Proceedings, CEURWS. org, Toulouse, France, 2015.

5. Nedjar Imane, Mahmoudi Saïd, Chikh Mohamed Amine, ”Content-based Medical Image Retrieval for Liver CT Annotation”, International conference on affective computing, machine learning and intelligent systems Tétouan, Maroc, 2017.

6. Nedjar Imane, Mahmoudi Saïd, Chikh Mohammed Amine, ”Topological methods for mammographic images classification: The Digital Mammography DREAM Challenge 2017”, In 11th annual RECOMB/ISCB Conference on Regulatory & Systems Genomics, NYU Langone Health, in New York City, New York, USA, 2018.

7. Nedjar Imane, Mahmoudi Saïd, Chikh Mohammed Amine, ”A comparative study of different deep learning architectures for breast cancer histology images classification”, In ”Mardi des Chercheurs”, Mons, Belgique, 2019.

Abstract

Computer aided detection and diagnosis CADe/CADx systems, are an essential tools used by physicians to assist them in their daily clinical diagnosis. In cancers diseases, these systems have an important role to perform the early detection and diagnosis, this allows to provide early treatment before it will be too late. In this thesis, we present several methods to be uses in a computer aided diagnosis system in order to generate structured reports of liver lesions including cancer using Computed Tomography (CT) images. In addition, we propose different methods for computer aided detection of breast cancer, by treating breast density classification using mammography and breast lesion classification using histopathology images. At this context we present three distingue contributions, the first one is related to the annotation of liver CT images by using a medical ontology, in which we propose three methods. The second contribution is about breast density classification according to the standard Breast Imaging Reporting and Data System (BI-RADS). In addition to that, we propose an improved version of Synthetic Minority Over-Sampling Technique Algorithm (SMOTE) used to equilibrate the dataset. The last contribution is about breast lesions classification in the histopathology images. Precisely, we propose a method to distinct benignant and malignant lesions, as well to classify the normal cases, benign cases, in situ and invasive cancer cases.

Keywords

Medical images; Computer-Aided Diagnosis; Image Retrieval; Liver annotation; BEMD; Gabor wavelet; Mammography; Breast tissue classification; SMOTE; Image classification; Histology images; Deep learning.

ملخص

تعد أنظمة الكشف والتشخيص بمساعدة الكمبيوتر CADe/CADx أدوات أساسية يستخدمها الأطباء لمساعدتهم في تشخيصهم اليومي. بحيث تلعب هذه الأنظمة دورًا مهمًا في إجراء الكشف والتشخيص المبكر لأمراض السرطان، مما يسمح بتوفير العلاج المبكر قبل فوات الأوان.

في هذه الأطروحة، نقدم العديد من الطرق للاستعمال في نظام التشخيص بمساعدة الكمبيوتر لإنشاء تقارير منظمة لآفات الكبد بما في ذلك السرطان، و هذا من خلال استخدام صور التصوير المقطعي (CT). إضافة إلى ذلك، نقترح طرقًا مختلفة للاستعمال في نظام الكشف عن سرطان الثدي بمساعدة الكمبيوتر، عن طريق معالجة تصنيف كثافة الثدي باستخدام التصوير الشعاعي للثدي و كذلك تصنيف آفات الثدي باستخدام صور الأنسجة.

في هذا السياق نقدم ثلاث مساهمات متباينة، تتعلق الأولى بتقديم تعليقات على صور الأشعة المقطعية للكبد باستخدام الأنطولوجيا الطبية، حيث نقترح هنا ثلاث طرق .

أما المساهمة الثانية فتتعلق بتصنيف كثافة الثدي وفقًا لتقرير تصوير الثدي النموذجي ونظام البيانات (BI-RADS). بالإضافة إلى ذلك، نقترح تعديلا محسنًا لخوارزمية تقنية الإفراط في أخذ العينات للأقليات الاصطناعية (SMOTE) المستخدمة لموازنة مجموعة البيانات.

المساهمة الأخيرة هي في تصنيف آفات الثدي باستخدام صور الأنسجة. على وجه التحديد، نقترح طريقة لتمييز الآفات الحميدة والخبيثة، وكذلك لتصنيف الحالات الطبيعية، الحالات الحميدة، حالات السرطان الموضعية والغزوية.

الكلمات الدالة

الصور الطبية؛ التشخيص بمساعدة الحاسوب؛ استرجاع الصورة؛ التعليق على صور الكبد؛ BEMD؛ مويجات الغابور؛ التصوير الشعاعي للثدي؛ تصنيف أنسجة الثدي؛ SMOTE؛ BI-RADS؛ صور الأنسجة؛ التعلم العميق.

Résumé

Les systèmes de détection et de diagnostic assistés par ordinateur CADe/CADx sont des outils essentiels utilisés par les médecins pour les aider dans leur diagnostic clinique quotidien. Ces systèmes ont un rôle important pour effectuer la détection et le diagnostic précoces des maladies cancéreuses, ce qui permet de fournir un traitement précoce avant qu'il ne soit trop tard.

Dans cette thèse, nous présentons plusieurs méthodes à utiliser dans le système de diagnostic assisté par ordinateur pour générer des rapport structurés sur les lésions hépatiques, y compris le cancer, en utilisant les images de tomodensitométrie. De plus, nous proposons différentes méthodes à utiliser dans la détection assistée par ordinateur pour le cancer du sein, en traitant la classification de la densité mammaire par l'utilisation des images mammographiques et aussi la classification des lésions mammaires par l'utilisation des images histopathologiques.

Dans ce contexte, nous présentons trois distinctes contributions, la première est liée à l'annotation des images CT du foie en utilisant une ontologie médicale, où nous proposons trois méthodes différentes.

La deuxième contribution concerne la classification de la densité mammaire selon le système standard de rapport et de données d'imagerie mammaire (BI-RADS). De plus, nous proposons une version améliorée de l'algorithme SMOTE (Synthetic Minority Over-Sampling Technique Algorithm) utilisé pour équilibrer l'ensemble de données.

La dernière contribution concerne la classification des lésions mammaires dans les images histopathologiques. Précisément, nous proposons une méthode pour distinguer les lésions bénignes et malignes, ainsi que pour classer les cas normaux, les cas bénins, les cas de cancer in situ et invasif.

Mots clefs

Images médicales; Diagnostic assisté par ordinateur; Récupération des images; Les annotations hépatique; BEMD; Ondelettes de Gabor; Mammographie; Classification des tissus mammaires; SMOTE; BI-RADS; Les images histopathologiques; Apprentissage profond.